Master's Thesis

ON THE INFLUENCE OF BOTTOM TOPOGRAPHY ON THE LARGE SCALE OCEAN CIRCULATION

Masters program: Climate Physics
Mathematisch Naturwissenschafftliche Fakultät
Christian-Albrechts-Universität zu Kiel

18 April
2017

Supervisor
Prof. Dr. **Richard J. Greatbatch**

Submitted by
Ezra Eisbrenner

Second assessor
Prof. Dr. **Joke F. Lübbecke**

Abstract

The effects of variable bottom topography are investigated on the basis of idealised model simulations. The simulations feature idealised bottom topographies with increasing complexity, starting with a single hemisphere flat-bottomed basin and evolving to a full idealised Atlantic Ocean with continental margins, a mid oceanic ridge, a Drake Passage opening to create an Antarctic Circumpolar Current and two Nordic Seas openings to allow for dense overflows into the North Atlantic basin. The goal of the study is to expand the work of Holland (1973) concerning the impact of sloping bottom topography along the western boundary on the horizontal transport streamfunction in order to show the effects of other bottom topography features and the response of the transport streamfunction when multiple bottom topography features are combined. The diagnostics focus on the calculation of the horizontal streamfunction and the meridional overturning. The results highlight the role of variable bottom topography for the horizontal streamfunction and the crucial role of the meridional overturning. It is shown that the depth of the meridional overturning dictates whether the horizontal streamfunction is amplified or weakened by the underlying bottom topography. Furthermore, it is shown that for increasingly complex bottom topographies the horizontal streamfunction converges towards the classical gyre system, represented by the flat-bottomed Sverdrup transport. However, the variable bottom topography tends to amplify the gyres with respect to the afore mentioned Sverdrup transport, i.e. leading to a desirable increase of the transport of the subtropical western boundary current. This study provides new visualisations of the effects of varying bottom topography and provides an introduction to the necessary components of the bottom topography to realistically represent the Atlantic Ocean circulation.

Zusammenfassung

Die Auswirkungen von variabler Bodentopographie werden auf der Basis von idealisierten Modellsimulationen untersucht. Die Simulationen bieten idealisierte Bodentopographien mit zunehmender Komplexität, beginnend mit einer einzelnen Hemisphäre und flachem Ozeanboden und entwickeln sich zu einem idealisierten Atlantik mit kontinentalen Hängen, einem mittelozeanischen Rücken, einer Drake-Passage, welche einen antarktischen Zirkumpolarstrom ermöglicht, und zwei Öffnungen in ein Nordische Seen becken, welches Überströmen von dichtem Wasser in den Nordatlantik ermöglicht. Das Ziel der Studie ist es, auf die Erkenntnisse der Arbeit von Holland (1973) über die Auswirkungen, von schräger Bodentopographie entlang des westlichen Randes auf die horizontale Transportstromfunktion, aufzubauen, mit dem Ziel die Auswirkungen anderer Bodentopographie-Merkmale zu untersuchen und die dadurch verursachten Veränderungen der Transportstromfunktion zu zeigen, insbesondere wenn mehrere Bodentopographie-Merkmale kombiniert werden. Die Diagnose konzentriert sich auf die Berechnung der horizontalen Stromfunktion und der meridionalen Umwälzbewegung. Die Ergebnisse stellen die Rolle der variablen Bodentopographie für die horizontale Strömungsfunktion heraus und weiterhin unterstreichen sie die entscheidende Rolle der meridionalen Umwältzbewegung. Es wird gezeigt, dass die Tiefe der meridionalen Umwälzbewegung diktiert, ob die horizontale Stromfunktion durch die darunterliegende Bodentopographie verstärkt oder geschwächt wird. Weiterhin wird gezeigt, dass für zunehmend komplexe Bodentopographien die horizontale Stromfunktion zum klassischen Gyre-System konvergiert, das durch den Sverdruptransport mit flachem Boden repräsentiert wird. Insgesammt zeigt sich jedoch, dass die variable Bodenopographie, das Gyre-System in Bezug auf den zuvor genannten Sverdruptransport stärkt, d.h. es führt zu einer angestrebten Erhöhung des Transportes des subtropischen westlichen Randstroms. Diese Studie bietet neue Visualisierungen der Auswirkungen unterschiedlicher Bodentopographien und liefert eine Einführung in die notwendigen Komponenten der Bodentopographie, um die zirkulation des Atlantischen Ozeans realistisch zu repräsentieren.

Acknowledgements

I wish to thank Richard J. Greatbatch for his help and advice during the shaping and writing of the thesis and to Markus Scheinert for his help with the NEMO ocean model and the supercomputer.

Contents

1 Introduction

The role of variable bottom topography was a point of debate in the past. The debate originated in the fundamental work of Sverdrup (1947), Stommel (1948) and Munk (1950) about integral mass flux together with spin-up experiments on one side (e.g., Anderson, Bryan, Gill, & Pacanowski, 1979), and the role of bottom form drag in the Southern Ocean balance at the other (e.g., Munk & Palmén, 1951). The use of integral mass or volume flux to describe the ocean general circulation patterns in terms of a mass or volume transport streamfunction yielded convincing results purely based on wind stress and Coriolis effect, whilst featuring a flat-bottomed ocean (e.g. Munk, 1950). Therefore it was assumed that the effects of variable bottom topography must play only a minor role. This view was supported by spin-up experiments, which showed that after an initial rapid adjustment associated with barotropic Rossby waves to the topographic Sverdrup balance, the slower baroclinic Rossby waves would confine the flow field to the upper layer and isolate the flow field from the bottom topography (e.g., Anderson & Killworth, 1977; Anderson et al., 1979).

In contradiction to the assumed unimportance of variable bottom topography stood the Southern Ocean Circumpolar Current balance, where bottom form drag is essential to provide enough counter-momentum to balance the strong zonal wind stress at the surface (e.g., Munk & Palmén, 1951), implying an interaction of the flow field and variable bottom topography. The Munk and Palmén (1951) paper was, nevertheless, largely ignored until eddying models were applied to the Southern Ocean and this balance could be verified numerically (Rintoul, Hughes, & Olbers, 2001).

Furthermore, observation based estimates of the transport of western boundary currents in the North Atlantic (e.g., Knauss, 1969; Gill, 1971) showed that the predictions, based on the flat-bottomed Sverdrup transport, highly underestimated the actual western boundary current transport. This discrepancy between observations and calculations of the flat-bottomed Sverdrup transport was first addressed by Sarkisyan (1969) and Sarkisyan and Ivanov (1971), who incorporated baroclinicity and variable bottom topography into their calculations. They showed that including variable bottom topography as well as baroclinicity would change the transport streamfunction to great extend compared to the solution obtained from the flat-bottomed and homogeneous case (Sarkisyan & Ivanov, 1971), e.g. the Sverdrup transport.

Soon after, the work of Holland (1973) demonstrated the impact of simple variable bottom topography on the transport streamfunction using a general ocean circulation model, as it was shown that the simulation with variable bottom topography exhibited major differences in the corresponding transport streamfunctions compared to the flat-bottomed control simulation, in particular a strong increase of the western boundary current transport.

The incorporation of variable bottom topography and baroclinicity into the calculation of the transport streamfunction (Sarkisyan & Ivanov, 1971; Holland, 1973) challenged an additional assumption concluded from earlier ocean gyre models, which was the need for strong friction within the boundary layer as a closure (e.g. Stommel, 1948; Munk, 1950). That variable bottom topography at the western boundary reduced the need of friction within the western

boundary region was noted by Mellor, Mechoso, and Keto (1982), who showed that for the Atlantic Ocean the interaction with variable bottom topography can produce closed streamlines, replacing friction as the western boundary closure method. This was further underlined by the work of Hughes (2000) and Hughes and de Cuevas (2001), which theoretically underpinned the importance of variable bottom topography over viscosity within western boundary currents and the gyre circulation in general. Therefore, although the calculation of flat-bottomed transport streamfunctions had been proven to be a powerful tool to reproduce major patterns of the large scale oceanic circulation (e.g. Stommel, 1948; Munk, 1950), it became apparent that the assumption of the flat bottom had to be revised due to discrepancies with western boundary current observations, which then led to the incorporation of variable bottom topography and baroclinicity for the consideration of the processes that contribute to the horizontal transport streamfunction.

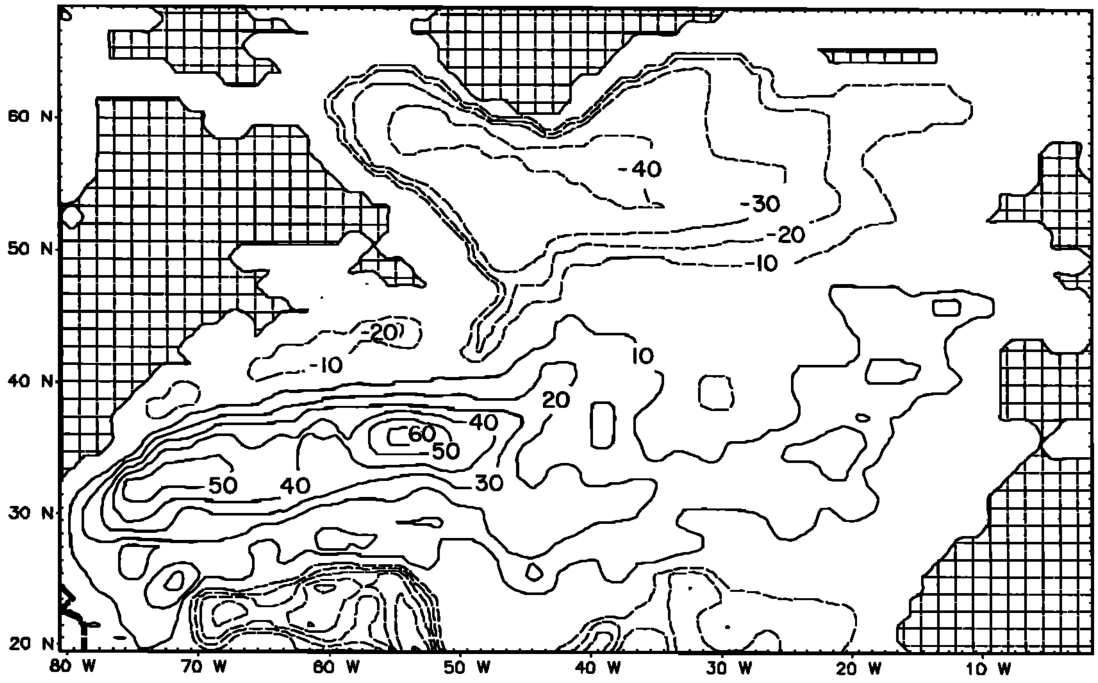

Figure 1: The North Atlantic Ocean from 20°N to 70°N and 80°W to 0°W. Seen is the transport streamfunction (annual mean field) calculated using climatological mean winds and density data. The contour interval is 10 Sv. Dashed contours indicate negative values; solid contours, positive values. The zero contour is not drawn. The figure is taken from Greatbatch et al. (1991, Fig. 1).

In Greatbatch et al. (1991), the transport streamfunction with variable bottom topography and baroclinicity was calculated for the North Atlantic (Figure 1), following Mellor et al. (1982). This demonstrated successfully that the general ocean circulation is well approximated by the transport streamfunction under the assumption of negligible viscosity but variable bottom topography and baroclinicity, as it showed many realistic looking features (Greatbatch et al., 1991). Greatbatch et al. (1991) also suggested a decomposition of the transport streamfunction into parts associated with an uniform density ocean, density compensation and bottom pressure torque; a very useful approach to separate the effects of variable bottom topography.

While the prior discussion concentrated on topics that were mostly investigated in times of very limited computational capabilities, other studies of the recent past were able to look at processes that were impractical to investigate previously. This includes the influence of resolution, i.e. partly resolving the eddy field, and the impact of different viscosities on the deep ocean currents and their imprint on the integral mass and volume flux (e.g., Hughes & de Cuevas, 2001; Spence, Saenko, Sijp, & England, 2012) as well as temporal variability and the link of the former to the Atlantic Meridional Overturning Circulation (AMOC), which is an important measure used to investigate the state of our climate system (e.g., Yeager, 2015).

1.1 Goal of the Study

The influence of variable bottom topography on the large scale ocean circulation will be investigated systematically in this thesis using an ocean general circulation model. The original model set-up used in Holland (1973) will be expanded gradually with the goal to clarify the influence of basic bottom topography features on the large scale oceanic circulation, by comparing the corresponding transport streamfunctions. Bottom topography features will be added using a modular approach, and will include continental margins, a mid oceanic ridge and a land mass protruding into the ocean basin creating a Labrador basin, as well as an Antarctic Circumpolar Current and the Nordic Seas. The result is a series of experiments, evolving in complexity from the classical flat-bottomed ocean basin to an idealized Atlantic Ocean.

The thesis is organised as follows, in Chapter 2 the theoretical background is provided, especially the streamfunction equations under the effect of variable bottom topography are derived in detail. Then in Chapter 3 the ocean general circulation model used to carry out the simulations is presented. In Chapter 4 the numerical notation for the transport streamfunctions is provided and the available options to decompose the former (Greatbatch et al., 1991) are presented. In Chapter 5 the experiments and their implementation into the model are presented, including the creation of the surface forcing and restoring fields as well as the design of the bottom topographies. Then in Chapter 6 the findings of this thesis are presented in detail, followed by Chapter 7 where the results are summarised and possible improvements and ideas for future experiments are discussed. Finally, the Appendix includes the model validation and technical material concerning the ocean general circulation model.

2 Theory

This section introduces the central theoretical concepts used for this thesis. First, some important definitions are introduced, then the basic set of equations are presented together with their boundary conditions. Next, the method of integral mass flux is derived, which allows the description of the large scale ocean circulation using the horizontal mass or volume transport streamfunction.

The derivation of the method of integral mass flux, is done stepwise. First, the previously introduced equations are vertically integrated, i.e. the continuity equation, the hydrostatic equation and the horizontal momentum equations. Secondly, the integrated horizontal momentum equations are combined, analogous to the way vorticity is derived, building the equations that, on the one hand, led to the early examples in this field (Sverdrup, 1947; Stommel, 1948; Munk, 1950) and, on the other, leads to the equations involving the "Bottom Pressure Torque" term (BPT, Sarkisyan, 1969; Holland, 1973) and the "Joint Effect of Baroclinicity And Relief" term (JEBAR, Sarkisyan & Ivanov, 1971). The latter two are the equations of interest as they incorporate variable bottom topography into the method of integral mass flux.

The section is concluded with a note about the vertical integration, since an in depth description of the vertical integral and surrounding assumptions is often missing.

2.1 Mathematical Definitions

Some of the mathematical definitions have to be introduced. Therefore in this section the mathematical expressions used for the thesis are quickly introduced and also short forms of mathematical expressions are defined.

Unit vectors are given by $\hat{\mathbf{e}}_i$, with $i \in 1, 2, 3$.

General coordinates are given by x_i, with $i \in 1, 2, 3$.

Definition of the Coordinate System: The coordinate system is for the purpose of simplicity chosen as the local Cartesian coordinates, unless otherwise stated, i.e. the horizontal coordinates at a given location are in longitudinal direction x, in latitudinal direction y and the local vertical will be denoted z, labeled $1, 2, 3$ respectively. Note that the model (see Section 3) uses spherical coordinates.

The summation convention states that over reoccurring indices a summation will be performed, e.g. $a_i b_i \equiv \sum_i a_i b_i$. The summation convention is implied for the remainder of the thesis.

An arbitrary vector denoted $\mathbf{a}$ is defined as

$$\mathbf{a} = \mathbf{a}_h + a_3\hat{\mathbf{e}}_3 = a_1\hat{\mathbf{e}}_1 + a_2\hat{\mathbf{e}}_2 + a_3\hat{\mathbf{e}}_3 \tag{1}$$

where the subscript h denotes the horizontal components of a vector. This definition will be applied predominantly on the velocity vector $\mathbf{v}$ and the Del operator $\boldsymbol{\nabla}$ to denote the horizontal

components, i.e. $\mathbf{v}_h$ and $\boldsymbol{\nabla}_h$.

The del operator is denoted by the nabla symbol

$$\boldsymbol{\nabla} \equiv \boldsymbol{\nabla}_h + \hat{\mathbf{e}}_3 \tfrac{\partial}{\partial x_3} = \hat{\mathbf{e}}_1 \tfrac{\partial}{\partial x_1} + \hat{\mathbf{e}}_2 \tfrac{\partial}{\partial x_2} + \hat{\mathbf{e}}_3 \tfrac{\partial}{\partial x_3} \tag{2}$$

where x_i, $i \in 1, 2, 3$ are coordinates corresponding to the unit vectors $\hat{\mathbf{e}}_i$, $i \in 1, 2, 3$.

The inner product also known as dot product is defined as $\mathbf{a} \cdot \mathbf{b} \equiv a_i b_i$, $i \in 1, 2, 3$. The dot-symbol used here will be exclusively used to represent the inner product. Note that the inner product can also be performed on higher order tensors, e.g. $\mathbf{a} \cdot \mathbf{B}^{(2)} \equiv a_j b_{ji}$, where $\mathbf{B}^{(2)}$ is a second order tensor with elements b_{ji}.

The outer product also known as dyadic product is defined as $\mathbf{ab} \equiv a_i b_j$, $i, j \in 1, 2, 3$. The absence of any symbol between two vectors exclusively refers to an outer product. Note that outer products also can be performed on higher order tensors, e.g. $\mathbf{a}\mathbf{B}^{(2)} \equiv \mathbf{C}^{(3)}$ where $\mathbf{B}^{(2)}$ is a second order tensor with components b_{jk}, $k \in 1, 2, 3$ and $\mathbf{C}^{(3)}$ a third order tensor with components $c_{ijk} = a_i b_{jk}$.

The vector product also known as cross product is defined as $(\mathbf{a} \times \mathbf{b})_i \equiv \varepsilon_{ijk} a_i b_j$ where ε_{ijk} is the Levi-Civita-Symbol in $\mathbb{R}^3$, i.e. $i, j, k \in 1, 2, 3$. The cross-symbol used here will be exclusively used to represent the vector product.

The vertical component of the curl. In the following an operator will be defined following the notation of Hasselmann (1982). The operator is defines as

$$\underset{\neg}{\boldsymbol{\nabla}} \equiv \hat{\mathbf{e}}_3 \times \boldsymbol{\nabla} = -\hat{\mathbf{e}}_1 \tfrac{\partial}{\partial x_2} + \hat{\mathbf{e}}_2 \tfrac{\partial}{\partial x_1} + 0\hat{\mathbf{e}}_3 \tag{3}$$

which corresponds to a 90° left (counter clockwise) rotation in the x-y-plane of the horizontal del operator $\boldsymbol{\nabla}_h$ (2). Furthermore, this operator can be multiplied, using the inner product, by an arbitrary vector to obtain the vertical component of the curl of that vector, e.g. the vertical component of the curl of the momentum $\mathbf{p}$ can be written as $\hat{\mathbf{e}}_3 \cdot (\boldsymbol{\nabla} \times \mathbf{p})$ which is equal to $(\hat{\mathbf{e}}_3 \times \boldsymbol{\nabla}) \cdot \mathbf{p} \equiv \underset{\neg}{\boldsymbol{\nabla}} \cdot \mathbf{p}$. This follows from the interchangeability of inner and vector product in this kind of product, known as scalar triple product.

Proof: assuming a pair of vectors $\mathbf{a}$ and $\mathbf{b}$ with components a_1, a_2, a_3 and b_1, b_2, b_3, and using the abbreviation $\frac{\partial}{\partial x_i} \equiv \partial_i$, then the scalar triple product as seen above is

$$\begin{aligned}
\mathbf{a} \cdot (\boldsymbol{\nabla} \times \mathbf{b}) &= \begin{pmatrix} a_1 \\ a_2 \\ a_3 \end{pmatrix} \cdot \begin{pmatrix} \partial_2 b_3 - \partial_3 b_2 \\ -\partial_1 b_3 + \partial_3 b_1 \\ \partial_1 b_2 - \partial_2 b_1 \end{pmatrix} \\
&= a_1 \partial_2 b_3 - a_1 \partial_3 b_2 - a_2 \partial_1 b_3 + a_2 \partial_3 b_1 + a_3 \partial_1 b_2 - a_3 \partial_2 b_1 \\
&= \begin{pmatrix} a_2 \partial_3 - a_3 \partial_2 \\ -a_1 \partial_3 + a_3 \partial_1 \\ a_1 \partial_2 - a_2 \partial_1 \end{pmatrix} \cdot \begin{pmatrix} b_1 \\ b_2 \\ b_3 \end{pmatrix} = (\mathbf{a} \times \boldsymbol{\nabla}) \cdot \mathbf{b}
\end{aligned}$$

The Jacobian determinant is another mathematical definition used later, the Jacobian determinant will, for practical reasons, be presented here for the example of two variables A and B and the two general coordinates x and y. Under those restrictions the Jacobian determinant is defined as

$$J(A,B) = \det\mathbf{J}(A,B) = \det\begin{pmatrix} \frac{\partial A}{\partial x} & \frac{\partial B}{\partial x} \\ \frac{\partial A}{\partial y} & \frac{\partial B}{\partial y} \end{pmatrix} = \frac{\partial A}{\partial x}\frac{\partial B}{\partial y} - \frac{\partial A}{\partial y}\frac{\partial B}{\partial x}, \tag{4}$$

i.e. the determinant (det) of the Jacobian matrix ($\mathbf{J}$) of the variables A and B.

A definite integral with boundaries a and b has the form

$$\int_a^b f(\chi)\, d\chi = F(b) - F(a) \equiv F|_a^b \tag{5}$$

where F is an indefinite integral of f, with $\frac{\partial F}{\partial \chi} = f$.

Leibniz integral rule is defined as

$$\frac{d}{d\omega}\int_{\chi_1(\omega)}^{\chi_2(\omega)} f\big(\chi,\omega\big)\, d\chi = \int_{\chi_1(\omega)}^{\chi_2(\omega)} \frac{\partial f\big(\chi,\omega\big)}{\partial\omega}\, d\chi + f\big(\chi_2(\omega),\omega\big)\frac{d\chi_2(\omega)}{d\omega} - f\big(\chi_1(\omega),\omega\big)\frac{d\chi_1(\omega)}{d\omega} \tag{6}$$

and is the derivative of an integral with bounds which themselves depend on the derivatives variable, therefore the chain rule has to be applied.

2.2 The Governing Equations

As the starting point the linearised hydrostatic and Boussinesq approximated momentum equations for an ocean in steady state are chosen, where molecular viscosity is neglected but part of the Reynolds stress term is kept via a downgradient eddy closure (see below), which together with the continuity equation leads to the following system of equations

$$f\hat{\mathbf{e}}_3 \times \mathbf{v}_h = -\frac{1}{\rho_0}\boldsymbol{\nabla}_h\, p + \frac{1}{\rho_0}\frac{\partial\boldsymbol{\tau}}{\partial z} \tag{7a}$$

$$0 = -\frac{\partial p}{\partial z} - \rho g \tag{7b}$$

$$\boldsymbol{\nabla}\cdot\mathbf{v} = 0 \tag{7c}$$

where f is the Coriolis parameter $f = 2\Omega\sin(\phi)$, i.e. twice the Earth's angular velocity Ω about the local vertical $\hat{\mathbf{e}}_3$ at the latitude ϕ. $\mathbf{v}_h$ is the horizontal velocity vector, following equation (1). ρ_0 is the mean density. $\boldsymbol{\nabla}_h$ are the horizontal components of the Del operator, see equation (1) and (2). p is the pressure. z is the local vertical coordinate, and $\boldsymbol{\tau}$ is the

horizontally acting stress vector, defined, using a kinematic eddy viscosity ν, by

$$\frac{\partial \boldsymbol{\tau}}{\partial z} \equiv \frac{\partial}{\partial z}\left(\nu \frac{\partial \mathbf{v}_h}{\partial z}\right) \tag{8}$$

which is the downgradient eddy closure approximation to the vertical Reynolds stress term, a remnant of the time averaged non-linear term[1]. For a discussion of the downgradient eddy closure, see for example Roberts and Marshall (2000).

2.2.1 Boundary Conditions

For solving the system of partial differential equations (7) it is necessary to specify boundary conditions. These are for the turbulent stresses

$$\boldsymbol{\tau} = \boldsymbol{\tau}|^s \qquad \text{at } z = \eta \tag{9a}$$

$$\boldsymbol{\tau} = \boldsymbol{\tau}|_b \qquad \text{at } z = -H \tag{9b}$$

where $\boldsymbol{\tau}|^s$ is the surface wind stress vector, $\boldsymbol{\tau}|_b$ the bottom stress vector, $z = \eta$ the sea surface elevation and $z = -H$ the ocean bottom.

For the velocities, the kinematic boundary conditions in steady state are

$$\tfrac{D}{Dt}\Big(z - \eta\Big) = w^s - \mathbf{v}_h^s \cdot \boldsymbol{\nabla}_h \eta = 0 \qquad \text{at } z = \eta \tag{10a}$$

$$\tfrac{D}{Dt}\Big(z + H\Big) = w^b + \mathbf{v}_h^b \cdot \boldsymbol{\nabla}_h H = 0 \qquad \text{at } z = -H. \tag{10b}$$

Furthermore, for reasons of simplicity the atmospheric pressure p_a is assumed to be constant in time and spatially uniform

$$\frac{\partial p_a}{\partial x} \approx \frac{\partial p_a}{\partial y} \approx 0. \tag{11}$$

The atmospheric pressure variations are usually considered small, however for the later model calculations the atmospheric pressure is assumed zero everywhere, fulfilling the condition above.

2.2.2 Pressure and Bottom Pressure

The equation describing the pressure can be derived by integrating the hydrostatic equation (7b) from the bottom at $z = -H$ to a variable depth z, i.e.

$$p = p_b - \int_{-H}^{z} g\rho \, dz \tag{12}$$

[1] Reynolds averaging assumes a constant density (Reynolds, 1895), therefore other averaging methods are often used. See for example Favre (1992).

where p_b is bottom pressure which satisfies

$$p_a - p_b = -\int_{-H}^{\eta} g\rho \, dz \tag{13}$$

where p_a is the surface (atmospheric) pressure.

2.3 The Integral Equations

To derive the equation containing the "Joint Effect of Baroclinicity And Relief" term (JEBAR, Sarkisyan & Ivanov, 1971) as well as the equation containing the "Bottom Pressure Torque" term (BPT, Sarkisyan, 1969; Holland, 1973) it is necessary to integrate the horizontal momentum equation vertically. Since the result of the vertical integration can be used later for both derivations this integration is done separately in the following section, starting with the definition of the integral, followed by the integrated continuity equation and hydrostatic equation. Finally, the obtained results are used during the derivation of the vertically-integrated horizontal momentum equations.

2.3.1 The Vertical Integral

The vertical integral applied in the following subsections for an arbitrary variable a is defined as follows

$$\int_{-H}^{\eta} a \; dz = A \tag{14}$$

where $H = H(x, y)$ is the modulus of the water depth measured relative to the level $z = 0$ and $\eta = \eta(x, y)$ is the free surface in steady state.

2.3.2 Integrated Continuity Equation

Vertical integration (14) of the continuity equation (7c)

$$\int_{-H}^{\eta} \boldsymbol{\nabla} \cdot \mathbf{v} \; dz = 0 \tag{15}$$

gives

$$\boldsymbol{\nabla}_h \cdot \int_{-H}^{\eta} \mathbf{v}_h \; dz - \mathbf{v}_h^s \cdot \boldsymbol{\nabla}\eta - \mathbf{v}_h^b \cdot \boldsymbol{\nabla} H + \int_{-H}^{\eta} \frac{\partial w}{\partial z} \; dz = 0 \tag{16}$$

where the Leibniz integral rule (6) was applied. Integration of the vertical velocity term

$$\int_{-H}^{\eta} \frac{\partial w}{\partial z} \; dz \equiv w^s - w^b \tag{17}$$

together with the definition (14), e.g. $\int_{-H}^{\eta} \mathbf{v}_h \, dz = \mathbf{V}_h$, leads to

$$\boldsymbol{\nabla}_h \cdot \mathbf{V}_h - \mathbf{v}_h^s \cdot \boldsymbol{\nabla}_h \, \eta - \mathbf{v}_h^b \cdot \boldsymbol{\nabla}_h \, H + w^s - w^b = 0 \tag{18}$$

for which substitution of w^s and w^b from the the kinematic boundary conditions (10) leads to

$$\boldsymbol{\nabla}_h \cdot \mathbf{V}_h = 0. \tag{19}$$

This result allows for the introduction of a streamfunction Ψ, since the integral volume transport divergence is zero. Ψ is defined by

$$\underset{\neg}{\boldsymbol{\nabla}} \Psi = \mathbf{V}_h. \tag{20}$$

Note that the operator $\underset{\neg}{\boldsymbol{\nabla}}$ represents a left rotation of the horizontal del operator $\boldsymbol{\nabla}_h$ in the x-y-plane as defined in (3).

2.3.3 Integrated Hydrostatic Equation

Here the integrated pressure P will be derived. Following the integral definition (14), the hydrostatic equation (7b) is integrated, using the pressure (12) and bottom pressure (13).

$$\begin{aligned} P = \int_{-H}^{\eta} p \, dz &= \int_{-H}^{\eta} \left(p_b - \int_{-H}^{z} g\rho \, dz' \right) dz \\ &= p_b(\eta + H) - \left[z \int_{-H}^{z} g\rho \, dz' \right]_{-H}^{\eta} + \int_{-H}^{\eta} z g\rho \, dz \end{aligned} \tag{21}$$

which with

$$\left[\chi \int_{\chi_0}^{\chi} f(\chi) \, d\chi \right]_{\chi_0}^{\chi_1} = \chi_1 \int_{\chi_0}^{\chi_1} f(\chi) \, d\chi \tag{22}$$

and (13) results in the vertically-integrated pressure

$$P = p_a \eta + p_b H + \Phi \tag{23}$$

where Φ is defined as

$$\Phi \equiv \int_{-H}^{\eta} z g\rho \, dz \tag{24}$$

with Φ being the potential energy per unit area, referenced to the surface.

2.3.4 Integrated Horizontal Momentum Equation

For the derivation of the JEBAR term and the BPT term the vertically-integrated horizontal momentum equations are required. The integration, following (14), of the horizontal momen-

tum (7a) uses the results of the two previous subsections 2.3.2 and 2.3.3 and is presented in the following.

Integration (14) of the term on the left hand side of (7a), the Coriolis term, gives

$$\int_{-H}^{\eta} f\hat{\mathbf{e}}_3 \times \mathbf{v}_h \; dz = f\hat{\mathbf{e}}_3 \times \mathbf{V}_h \tag{25}$$

the first term on the right of (7a). The pressure gradient term, requires the application of the Leibniz integral rule (6), with which then follows

$$\int_{-H}^{\eta} -\frac{1}{\rho_0}\boldsymbol{\nabla}_h p \; dz = -\frac{1}{\rho_0}\Big(\boldsymbol{\nabla}_h P - p_a \boldsymbol{\nabla}_h \eta - p_b \boldsymbol{\nabla}_h H\Big) \tag{26a}$$

and using (23)

$$= -\frac{1}{\rho_0}\Big(\boldsymbol{\nabla}_h \left(p_a \eta + p_b H + \Phi\right) - p_a \boldsymbol{\nabla}_h \eta - p_b \boldsymbol{\nabla}_h H\Big) \tag{26b}$$

which with (11) yields

$$= -\frac{1}{\rho_0}\Big(\boldsymbol{\nabla}_h \Phi + H \boldsymbol{\nabla}_h p_b\Big). \tag{26c}$$

The second term on the right of (7a), the eddy viscosity term, becomes

$$\int_{-H}^{\eta} \frac{1}{\rho_0}\frac{\partial \boldsymbol{\tau}}{\partial z} \; dz = \frac{1}{\rho_0}\Big(\boldsymbol{\tau}|_{z=\eta} - \boldsymbol{\tau}|_{z=-H} \Big) \equiv \frac{1}{\rho_0}\boldsymbol{\tau}|_b^s. \tag{27}$$

Combining the results (25), (26) and (27) to the full vertically-integrated horizontal momentum equations yields

$$f\hat{\mathbf{e}}_3 \times \mathbf{V}_h = -\frac{1}{\rho_0}\Big(\boldsymbol{\nabla}_h \Phi + H \boldsymbol{\nabla}_h p_b\Big) + \frac{1}{\rho_0}\boldsymbol{\tau}|_b^s \tag{28a}$$

which is the basis for the derivation of the BPT term and JEBAR term. Note, for the JEBAR term, equation (28a) has to be divided by the total water column $H^* = H + \eta$, i.e. the modulus of the water depth H, measured downwards from the level $z = 0$, plus the free surface elevation η, to account for the vertical averaging rather than vertical integration. The vertically averaged horizontal momentum equations are

$$\frac{f}{H^*}\hat{\mathbf{e}}_3 \times \mathbf{V}_h = -\frac{1}{\rho_0 H^*}\Big(\boldsymbol{\nabla}_h \Phi + H \boldsymbol{\nabla}_h p_b \Big) + \frac{1}{\rho_0 H^*}\boldsymbol{\tau}|_b^s. \tag{28b}$$

Section 2.4.2 introduces a simplification of the above equation, ensuring recognisability during further steps of the derivation.

2.4 The Vorticity Analogue

The vertically-integrated horizontal momentum equations (28a), as well as the vertically averaged horizontal momentum equations (28b), can be further simplified if an approach analogous to the vorticity analysis is applied.

A vorticity analysis, where the vorticity ω is defined as the vertical component of the curl of the velocity vector $\mathbf{v}$, can reduce the horizontal momentum equations to a single equation, if the velocity $\mathbf{v}$ is purely horizontal. Note that the vorticity approach is identical to forming the inner product of the operator (3) with the corresponding momentum equations. Since for equation (28a) and (28b) the volume transport vector $\mathbf{V}_h$ is purely horizontal, the vorticity analysis will be carried out analogously.

There are two approaches, the first is to apply the operator (3) direct onto the vertically-integrated horizontal momentum equation (28a), which is done historically for simplified conditions (e.g., Sverdrup, 1947), see Section 2.4.1 or with more complexity (e.g., Holland, 1973) see Section 2.4.3. The second approach is to apply the operator onto the vertically averaged horizontal momentum equations (28b) (e.g., Sarkisyan & Ivanov, 1971), see Section 2.4.4.

2.4.1 Historical Solutions: The Homogeneous Ocean

The three most widely known solutions to the wind driven circulation are the Sverdrup relation (Sverdrup, 1947) and the extended versions from Stommel (1948) and Munk (1950), which are summarised in the following.

Sverdrup

To derive the Sverdrup relation (Sverdrup, 1947) one assumes an integral from a lower boundary with no vertical flow $w_b = 0$, for example a flat bottomed ocean or a level of no motion, to a rigid surface $w_s = 0$ and sets the stresses at the lower boundary equal to zero $\boldsymbol{\tau}|_b = 0$. Then forming the inner product of the operator (3) with (28a) leads to the Sverdrup relation

$$\beta \frac{\partial \Psi}{\partial x} = \frac{1}{\rho_0} \underset{\neg}{\boldsymbol{\nabla}} \cdot \boldsymbol{\tau}|^s \tag{29}$$

where Ψ is a volume transport streamfunction, i.e. (20), $\boldsymbol{\tau}|^s$ is the surface wind stress and β is the meridional derivative of the Coriolis term f.

Stommel

In Stommel (1948), a homogeneous, one layer ocean of uniform, undisturbed depth H and with total depth $H + \eta$, was assumed. During the derivation the approximation was made that $H + \eta \approx H$. The main difference to Sverdrup (1947) and Munk (1950) is the inclusion of a bottom stress in terms of a linear friction $\boldsymbol{\tau}|_b = R\mathbf{v}_h$ which leads to the Stommel solution

$$\beta \frac{\partial \Psi}{\partial x} = \frac{1}{\rho_0} \underset{\neg}{\boldsymbol{\nabla}} \cdot \boldsymbol{\tau}|^s - \frac{R}{\rho_0 H} \boldsymbol{\nabla}^2 \Psi \tag{30}$$

again with the streamfunction Ψ defined by (20).

Munk

In Munk (1950) most assumptions done by Sverdrup (1947) were kept, only extending the ansatz of vertical eddy viscosity by a horizontal eddy viscosity term $\boldsymbol{\nabla} \cdot (A_H \boldsymbol{\nabla} \mathbf{v}_h)$. Further, he did not neglect the lower boundary stresses $\boldsymbol{\tau}|_b$ right away, allowing for the possibility of a bottom that reaches up to the integration depth H, which in his case was about 1000-2000 meters. However, in general the lower boundary stresses were assumed negligible $\boldsymbol{\tau}|_b \approx 0$. The resulting equation is

$$\beta \frac{\partial \Psi}{\partial x} = \frac{1}{\rho_0} A_H \boldsymbol{\nabla}^4 \Psi + \frac{1}{\rho_0} \underset{\neg}{\boldsymbol{\nabla}} \cdot \boldsymbol{\tau}|^s \tag{31}$$

where A_H is the horizontal eddy viscosity coefficient with the streamfunction Ψ according to (20).

2.4.2 Simplified Vertical Integration

It is common to perform the integration, previously defined by equation (14), only up to the level $z = 0$, i.e.

$$\int_{-H}^{0} a \, dz = A. \tag{32}$$

Historically this was done since the models (e.g. Bryan (1969)) used the "rigid lid" approximation, i.e. $w = 0$ at $z = 0$. Under the "rigid lid" approximation the surface boundary condition (10a) acts at $z = 0$, allowing the use of (32) instead of (14).

For the presented thesis this can also be achieved by linearising the surface boundary condition (10a). This is viewed reasonable, since the momentum equations (7a) are also linearised and also, $\eta \ll H$. Again this allows the use of (32) instead of (14).

The results presented in the next two sections will be using the simplified integration (32). This has no effect on the vertically integrated momentum equation (28a), other than that the components derived in Sections 2.3.2, 2.3.3 and 2.3.4 have to be understood in the context of (32) rather than (14).

For the vertically averaged momentum equation (28b) the total water depth H^* simplifies to the simple water depth H measured downwards from the level $z = 0$. Besides this, as before, the individual terms have to be understood following equation (32).

Over the years many papers used zero as the upper limit of the vertical integral (32), e.g. Holland (1973), Mellor et al. (1982), Greatbatch et al. (1991), Mertz and Wright (1992), Myers, Fanning, and Weaver (1996) and Eden and Olbers (2010). Recent papers do also use η as the upper limit (14), however mostly for the derivation of the vertically integrated momentum equation, e.g Hughes (2000), Hughes and de Cuevas (2001), Jackson, Hughes, and Williams (2006) and Yeager (2015). In Yeager (2015) the vertically integrated momentum equation is derived using (14), while the vertically averaged momentum equation is derived using (32). Parallel to the step from (32) to (14), an evolution of models, away from the "rigid

lid" approximation, took place. The general ocean circulation model used during this thesis (NEMO version 3.4, see Section 3) removed the possibility to use the "rigid lid" approximation in 2009 (NEMO version 3.2).

2.4.3 Bottom Pressure Torque (BPT)

The equation containing the Bottom Pressure Torque (BPT, Holland, 1973) term is obtained via the vertical component of the curl of the vertically integrated horizontal momentum equation (28a). In order to gain the vertical component of the curl, the inner product of the operator (3) with (28a) is taken, which together with the relation (19), and using the integration (32), yields

$$\beta V = \frac{1}{\rho_0} J(p_b, H) + \frac{1}{\rho_0} \nabla \cdot \boldsymbol{\tau}|_b^s \tag{33a}$$

where $J(p_b, H)$ is the BPT term and the operator J, the Jacobian determinant (4), p_b is the bottom pressure, β is the meridional derivative of the Coriolis term f.

Equation (33a) can be rewritten in terms of a transport streamfunction (20), since $\mathbf{V}_h$ is solenoidal (19)

$$\beta \frac{\partial \Psi}{\partial x} = \tfrac{1}{\rho_0} J(p_b, H) + \tfrac{1}{\rho_0} \nabla \cdot \boldsymbol{\tau}|_b^s. \tag{33b}$$

2.4.4 Joint Effect of Baroclinicity And Relief (JEBAR)

The equation corresponding to the Joint Effect of Baroclinicity And Relief (JEBAR, Sarkisyan, 1969; Sarkisyan & Ivanov, 1971) term is gained by taking the vertical component of the curl of the vertically averaged horizontal momentum equations (28b), which corresponds to, forming the inner product of the operator (3) with (28b), where H^* is replaced by H, following (32). Together with the relation (19) then follows

$$\mathbf{V}_h \cdot \nabla_h \frac{f}{H} = \frac{1}{\rho_0} J(\Phi, \frac{1}{H}) + \frac{1}{\rho_0} \nabla \cdot \frac{\boldsymbol{\tau}|_b^s}{H} \tag{34a}$$

where $J(\Phi, \frac{1}{H})$ is the JEBAR term (Sarkisyan & Ivanov, 1971). Equation (34a) can also be rewritten in terms of a transport streamfunction (20) since $\mathbf{V}_h$ is solenoidal (19)

$$J(\Psi, \frac{f}{H}) = \frac{1}{\rho_0} J(\Phi, \frac{1}{H}) + \frac{1}{\rho_0} \nabla \cdot \frac{\boldsymbol{\tau}|_b^s}{H}. \tag{34b}$$

2.5 BPT and JEBAR under Homogeneous Density

Here the the BPT and JEBAR term are derived under the assumption of homogeneous density. The derivation is done assuming the full integration (14). By using the integral (14) this solution is also exact true for the primitive equations (44), introduced in the next chapter.

For a homogeneous density ocean ($\rho = \rho_0$) the BPT term in (33b) assuming (14) becomes,

$$\frac{1}{\rho_0} J(p_b, H)\Big|_{\rho \equiv \rho_0} = g J(\eta + H + \frac{p_a}{g\rho_0}, H) = g J(\eta, H). \tag{35}$$

The BPT term with homogeneous density is equal whether the surface boundary condition (10a) is linearised, the "rigid lid" approximation is applied, or not. As long as the vertical integration is chosen accordingly.

The JEBAR term (34b) with the integral (14) and not the simplified version (32), i.e. here $H^* = H + \eta$, becomes

$$J(\Psi, \frac{f}{H^*}) = \frac{1}{\rho_0} J(\Phi, \frac{1}{H^*}) + \frac{1}{\rho_0} J(p_b, \frac{H}{H^*}) + \frac{1}{\rho_0} \boldsymbol{\nabla} \cdot \frac{\boldsymbol{\tau}|_b^s}{H^*}. \tag{36}$$

For a homogeneous density ocean ($\rho = \rho_0$) the JEBAR term in (36), which is now defined by the left hand side of (37), becomes exact zero, i.e.

$$\begin{aligned} \frac{1}{\rho_0} J(\Phi, \frac{1}{H^*})\Big|_{\rho \equiv \rho_0} + \frac{1}{\rho_0} J(p_b, \frac{H}{H^*})\Big|_{\rho \equiv \rho_0} &= g\Big(J(\frac{\eta^2 - H^2}{2}, \frac{1}{H^*}) + J(\eta + H + \frac{p_a}{g\rho_0}, \frac{H}{H^*}) \Big) \\ &= g\Big(\eta J(\eta, \frac{1}{H^*}) + \frac{1}{H^*} J(\eta, H) + H J(\eta, \frac{1}{H^*}) \Big) \\ &= g\Big(-\frac{1}{H^*} J(\eta, H) + \frac{1}{H^*} J(\eta, H) \Big) = 0. \end{aligned} \tag{37}$$

This is also true if the surface boundary condition is linearised or the "rigid lid" approximation is applied, as long as the simplified integration (32) is applied too.

2.6 Linear Vorticity Dynamics

In Holland (1973) the vertical bottom velocity is related to the meridional velocities via the vertically integrated linear vorticity equation.

The linear vorticity equation is derived by taking the vertical component of the curl of the momentum equations (7a) and (7b), i.e.

$$\Big[\boldsymbol{\nabla} \times \Big(f \hat{\mathbf{e}}_3 \times \mathbf{v}_h \Big) \Big]_z = \Big[\boldsymbol{\nabla} \times \Big(-\frac{1}{\rho_0} \boldsymbol{\nabla} p - \frac{\rho}{\rho_0} \mathbf{g} + \frac{1}{\rho_0} \frac{\partial \boldsymbol{\tau}}{\partial z} \Big) \Big]_z, \tag{38}$$

which with the continuity equation (7c) results in

$$\beta v = f \frac{\partial w}{\partial z} + \frac{1}{\rho_0} \frac{\partial}{\partial z} \Big(\frac{\partial \tau^y}{\partial x} - \frac{\partial \tau^x}{\partial y} \Big). \tag{39}$$

Here βv is the advection of planetary vorticity term; $f w_z$ the vortex stretching term; the last term on the right is the vorticity input by the wind, where τ^x and τ^y are the zonal and meridional component of the horizontally acting stress $\boldsymbol{\tau}$.

Vertical integration[2] of (39) assuming the linearised surface boundary condition $w_s = 0$, leads to

$$\beta V = -f w_b + \frac{1}{\rho_0} \Big(\frac{\partial \tau_s^y}{\partial x} - \frac{\partial \tau_s^x}{\partial y} \Big). \tag{40}$$

Here τ_s^x and τ_s^y are the zonal and meridional component of the surface wind stress stress

[2] Integral of the form of equation (32).

$\boldsymbol{\tau}$, where the assumption is made that the bottom stresses are negligible. Now the vertical bottom velocity over sloping bottom topography can be related to the meridional velocities, i.e. northward flow is associated with downward motion and southward flow with upward motion (Holland, 1973).

Finally, assuming that the horizontal velocity at the bottom is in geostrophic balance,

$$\begin{aligned}\begin{pmatrix} u_b^g \\ v_b^g \end{pmatrix} = \begin{pmatrix} u^g \\ v^g \end{pmatrix}_{z=-H} &= \frac{1}{f\rho_0}\begin{pmatrix} -\frac{\partial p}{\partial y} \\ \frac{\partial p}{\partial x} \end{pmatrix}_{z=-H} \\ &= \frac{1}{f\rho_0}\begin{pmatrix} -\frac{\partial p_b}{\partial y} + \frac{\partial p(x,y,-H)}{\partial H}\frac{\partial H}{\partial y} \\ \frac{\partial p_b}{\partial x} - \frac{\partial p(x,y,-H)}{\partial H}\frac{\partial H}{\partial x} \end{pmatrix}\end{aligned} \tag{41}$$

here the superscript g denotes geostrophic velocities and the subscript b denotes bottom values, i.e. $p_b = p(x, y, -H)$. Then substituting the geostrophic bottom velocities (41) into the kinematic bottom boundary condition leads to

$$\begin{aligned} w_b^g &= -(u_g^b \tfrac{\partial H}{\partial x} + v_g^b \tfrac{\partial H}{\partial y}) \\ &= -\frac{1}{f\rho_0}(-\tfrac{\partial p}{\partial y}|_{z=-H}\tfrac{\partial H}{\partial x} + \tfrac{\partial p}{\partial x}|_{z=-H}\tfrac{\partial H}{\partial y}) \\ &= -\frac{1}{f\rho_0}((-\tfrac{\partial p_b}{\partial y} + \tfrac{\partial p(x,y,-H)}{\partial H}\tfrac{\partial H}{\partial y})\tfrac{\partial H}{\partial x} + (\tfrac{\partial p_b}{\partial x} - \tfrac{\partial p(x,y,-H)}{\partial H}\tfrac{\partial H}{\partial x})\tfrac{\partial H}{\partial y}) \\ &= -\frac{1}{f\rho_0}J(p_b, H) \end{aligned} \tag{42}$$

or equivalently

$$-fw_g^b = \frac{1}{\rho_0}J(p_b, H), \tag{43}$$

therefore, in the geostrophic limit, relating the vortex stretching term to the bottom pressure torque.

3 Model

In this chapter the general ocean circulation model used for this thesis is presented. The model is the Nucleus for European Modelling of the Ocean (NEMO) version 3.4 (Madec, 2008), here after referred to as NEMO.

First, the primitive equations as used in NEMO are presented followed by a short introduction to the Bryan (1969) model as used by Holland (1973). Then important coefficients of the different parameterizations are compared and partly discussed. Finally, the way the model is forced is demonstrated, with a focus on surface restoring for temperature and salinity and the associated time scales.

3.1 The Nucleus for European Modelling of the Ocean (NEMO) version 3.4

For this thesis NEMO version 3.4 (Madec, 2008) was used. This section is dedicated to introduce NEMO and give an overview of settings and parameters.

First the model equations are shown, the so called primitive equations, then the implementation of small-scale physics, bottom friction and surface forcings, is given.

The description of the implemented forcing fields follows in Section 5.

3.1.1 The Primitive Equations

The equations, the so called primitive equations, for NEMO are taken from the NEMO-manual version 3.4 (Madec, 2008). The equations are, with $\mathbf{v} = \mathbf{v}_h + w\hat{\mathbf{e}}_3 = u\hat{\mathbf{e}}_1 + v\hat{\mathbf{e}}_2 + w\hat{\mathbf{e}}_3$, given as follows

$$\frac{\partial \mathbf{v}_h}{\partial t} = -\left[(\boldsymbol{\nabla} \times \mathbf{v}) \times \mathbf{v} + \frac{1}{2}\boldsymbol{\nabla}\left(\mathbf{v} \cdot \mathbf{v}\right)\right]_h - f\hat{\mathbf{e}}_3 \times \mathbf{v}_h - \frac{1}{\rho_0}\boldsymbol{\nabla}_h p + \mathbf{D}^{\mathbf{v}} + \mathbf{F}^{\mathbf{v}} \tag{44a}$$

$$\frac{\partial p}{\partial z} = -\rho g \tag{44b}$$

$$\boldsymbol{\nabla} \cdot \mathbf{v} = 0 \tag{44c}$$

$$\frac{\partial T}{\partial t} = -\boldsymbol{\nabla} \cdot (T\mathbf{v}) + D^T + F^T \tag{44d}$$

$$\frac{\partial S}{\partial t} = -\boldsymbol{\nabla} \cdot (S\mathbf{v}) + D^S + F^S \tag{44e}$$

$$\rho = \rho(T, S, p) \tag{44f}$$

where $\boldsymbol{\nabla}$ is the generalised derivative vector operator in $(\mathbf{i}, \mathbf{j}, \mathbf{k})$ directions, t is the time, z is the vertical coordinate, ρ is the in situ density given by the equation of state (44f), ρ_0 is a reference density, p the pressure, $f = 2\boldsymbol{\Omega} \cdot \mathbf{k}$ is the Coriolis acceleration (where $\boldsymbol{\Omega}$ is the Earth's angular velocity vector), and g is the gravitational acceleration. $\mathbf{D}^{\mathbf{v}}$, D^T and D^S are the parametrisations of small-scale physics for momentum, temperature and salinity, and $\mathbf{F}^{\mathbf{v}}$, F^T and F^S surface forcing terms (Madec, 2008). Note that T is the potential temperature.

The primitive equations are for example derived in Olbers, Willebrand, and Eden (2012). A short list of the basic assumptions: spherical Earth approximation, assuming the Earth to be a sphere rather than an ellipsoid or geoid; thin-shell approximation, neglecting the water depth against the Earth's radius; turbulent closure hypothesis, expressing the small scale physics in terms of large scale features; Boussinesq hypothesis, approximation of the density as constant in the horizontal momentum equations; hydrostatic hypothesis, reducing the vertical momentum equation to the hydrostatic equation; (Madec, 2008), and finally replacing conservation of mass with conservation of volume, i.e. the continuity equation. The latter is phrased as Incompressibility hypothesis in the NEMO manual (Madec, 2008), however the primitive equations keep the aspect of compressibility due to the equation of state.

3.1.2 Parameterisations of Subgrid-Scale Physics

Most effects due to the non-linear terms fall below the model resolution and therefore have to be parameterized. For the presented thesis the down-gradient parameterization is chosen which approximates the term due to the unresolved non-linear term as

$$\frac{\partial}{\partial x}\left(A^l(\chi)\frac{\partial \chi}{\partial x}\right) + \frac{\partial}{\partial y}\left(A^l(\chi)\frac{\partial \chi}{\partial y}\right) + \frac{\partial}{\partial z}\left(A^v(\chi)\frac{\partial \chi}{\partial z}\right). \tag{45}$$

Here A^l and A^v are the lateral and vertical eddy viscosity coefficients. The coefficients applied in the momentum equations, are the lateral A^{lm} and vertical eddy viscosity A^{vm}. The coefficient applied to the tracer equations, i.e. for temperature and salinity, are the lateral A^{lT} and vertical eddy diffusivity A^{vT}, Table 1 contains the eddy coefficients used for the presented thesis. The separation of horizontal and vertical eddy coefficients originates in the difference of mixing strength along and across isopycnals.

In the equations of NEMO (Madec, 2008) the small-scale physics are summarized in the term D. An example for D from the horizontal momentum equation is

$$\mathbf{D}^{v\mathbf{v}} = \frac{\partial}{\partial z}\left(A^{vm}\frac{\partial \mathbf{v}_h}{\partial z}\right) \tag{46}$$

where the superscript $v\mathbf{v}$ of $\mathbf{D}$ denotes the vertical (v) gradient-component of the parameterization of the horizontal ($\mathbf{v}$) unresolved non-linear terms. The superscripts of A, i.e. vm denote that it is the vertical (v) eddy coefficient of the momentum (m) equation. Table 1 lists the eddy coefficients and their value as chosen for the presented thesis which are equal to the eddy coefficients in Holland (1973).

Name	Symbol	Value	Units
lateral eddy viscosity	A^{lm}	5×10^4	m^2/s
vertical eddy viscosity	A^{vm}	1×10^{-3}	m^2/s
lateral eddy diffusivity	A^{lT}	5×10^3	m^2/s
vertical eddy diffusivity	A^{vT}	1×10^{-4}	m^2/s

Table 1: Eddy coefficients as part of the down-gradient approximation of the unresolved component of the non-linear term in the momentum and tracer equations, applied in this thesis. The eddy coefficients are equal to the eddy coefficients in Holland (1973).

It should be noted that neither the Gent and McWilliams (1990) eddy parameterisation nor isopycnal mixing are implemented in the model experiments described in the thesis. The reason is historical: it was thought that these parameterisations were implemented by default in NEMO and it was only discovered too late that this is not, in fact, the case. On the other hand, the model set-up that is used has the advantage of enabling direct comparison with Holland (1973). Also, it is not expected that the results would be radically altered by including Gent and McWilliams and/or isopycnal diffusion, as could be verified in future work.

3.1.3 Lateral Boundary Condition

In NEMO, and in general for most models, the lateral boundaries need an additional parameterisation. This parameterisation defines how the flow, parallel and in direct proximity of the boundaries, is calculated. Classically, three options are available, first there is the free-slip condition, for which the flow field is continued, spatially constant, between the boundary and the first grid point; secondly, the no-slip condition, where the flow field is assumed to be at rest at the boundary; and third, the partial-slip condition, where the flow field is slowed down at the boundary, but not brought to rest. In NEMO a fourth option is available, the strong-slip condition, which is similar to the no-slip condition, however the velocity profile, between the boundary and the first velocity grid-point, is given by a sinusoidal function, where for the no-slip condition the velocity profile is linear. More details can be found in the NEMO manual (Madec, 2008, Sec. 8.1; Fig. 8.2).

The presented thesis uses the no-slip condition, following Holland (1973).

3.1.4 Bottom Friction

For the lower boundary of the water body a boundary condition in the form of bottom friction is implemented as a linear friction of the form

$$A^{vm} \frac{\partial \mathbf{v}_h}{\partial z}\bigg|_{z=k_b} = r \mathbf{v}_h^b \tag{47}$$

where A^{vm} is the vertical eddy viscosity (see Section 3.1.2), z is the vertical axis where $z = k_b$ is the model's bottom level, $\mathbf{v}_h$ the horizontal velocity vector, $\mathbf{v}_h^b$ the near bottom horizontal

velocity vector and r is the bottom drag coefficient chosen as $r = 4 \times 10^{-5}\,\mathrm{ms}^{-1}$. The bottom drag coefficient is chosen equal to the bottom drag coefficient used in Holland (1973).

3.2 Surface Forcing Fields

The following section describes the surface forcing fields. To perform a simulation with NEMO the ocean needs six fields as surface boundary condition: the two components of the surface ocean stress; the incoming solar and non solar heat fluxes; the surface freshwater budget; plus an optional field: the atmospheric pressure at the ocean surface (Madec, 2008).

For this thesis the meridional component of surface ocean stress, i.e. the wind stress, and the atmospheric pressure, are set to zero. The heat and freshwater fluxes are forced using a relaxation[3] formulation for which the surface temperature and salinity is read in from fields, that have to be provided. The use of the relaxation formulation requires the introduction of a restoring timescale parameter, i.e. an e-folding scale for the temperature and salinity surface equation. The zonal wind stress τ_u is incorporated as the surface boundary condition for the small scale physics (Section 3.1.2); a file has to be provided. Details about the fields related to heat flux, freshwater flux and zonal wind stress τ_u, used for this thesis, are described in Chapter 5: Experiments.

In the notation of NEMO, $\mathbf{F^v}$ is the momentum surface condition, i.e. wind stress, F^T and F^S are the temperature and salinity surface conditions, here defined by the flux formulation and the corresponding e-folding timescale.

The next two sections state the terms $\mathbf{F^v}$, F^T and F^S, with an emphasis of the explanation of the restoring condition and the calculation of the e-folding scale.

3.2.1 Wind Stress

The surface stress is implemented as

$$A^{vm} \frac{\partial \mathbf{v}_h}{\partial z}\bigg|_{z=k_1} = \frac{1}{\rho_0} \begin{pmatrix} \tau_u \\ \tau_v \end{pmatrix}. \tag{48}$$

Here A^{vm} is the vertical eddy viscosity coefficient (see Section 3.1.2), z is the vertical axis where $z = k_1$ is the model's surface level, $\mathbf{v}_h$ the horizontal velocity vector, ρ_0 the mean density, τ_u the zonal wind stress. The meridional wind stress τ_v is kept for generality, however τ_v is set to zero for all experiments.

3.2.2 Temperature and Salinity

The thermohaline forcing is chosen to be implemented as a restoring term in the surface equations for potential temperature (49) and salinity (50), following the original work of Holland (1973). The restoring field, to which the model surface temperature and salinity will be re-

[3] In NEMO the relaxation formalism is part of the flux formulation.

stored, will be denoted by a subscript R, i.e. T_R and S_R for temperature and salinity restoring respectively.

The formulas for surface temperature (49) and salinity (50) are roughly translated from the NEMO-FORTRAN-code (the NEMO-Handbook seems to be incomplete, at least concerning salinity) as

$$\frac{dT}{dt} = \frac{\gamma_T}{\rho_0 c_p \Delta z_1}(T - T_R) \tag{49}$$

$$\frac{dS}{dt} = \frac{\gamma_S}{\rho_0 c_s \Delta z_1}(S - S_R). \tag{50}$$

Here $\gamma_T = -80.0\,\mathrm{W/m^2/K}$ and $\gamma_S = -333.33\,\mathrm{mm/day}$ are the restoring coefficients for temperature and salinity respectively, $\Delta z_1 = 10\,\mathrm{m}$ is the surface level thickness (here the thickness of the first model level), $\rho_0 = 1035\,\mathrm{kg/m^3}$ is a reference density, $c_p = 4000\,\mathrm{J/kg/K}$ is the specific heat capacity of water as used by the NEMO 3.4, the last coefficient c_s is a conversion coefficient to transform γ_S into SI units, where $c_s = 86\,400\,\frac{\mathrm{m^2 s}}{\mathrm{kg}}\frac{\mathrm{mm}}{\mathrm{day}}$, the units of γ_S/c_s are therefore $\mathrm{kg/m^2/s}$.

3.2.3 *e*-Folding Scale: Restoring Time Scale

The restoring time scale is the e-folding scale for the surface temperature (49) and salinity (50) to approach the restoring value.

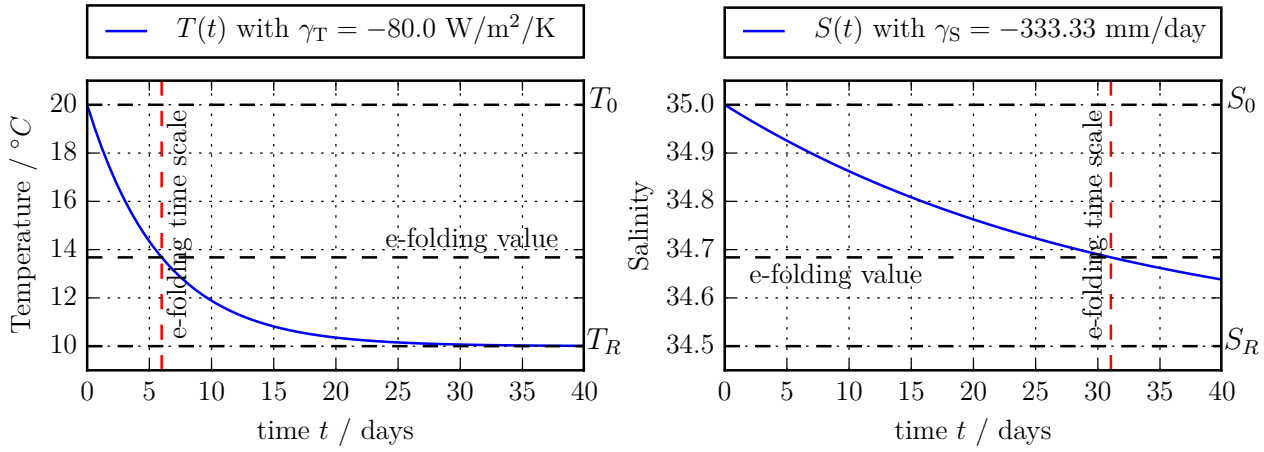

Figure 2: The e-folding time scale for temperature (left panel) and salinity (right panel). T_0, S_0 are the initial values and T_R, S_R the restoring values.

The calculation to obtain the e-folding scale can be done analytically, solving the inhomogeneous differential equation for the surface temperature (49) or salinity (50), excluding other terms.

Both equations, temperature (49) and salinity (50), can be reduced to

$$y' + ay = r \tag{51}$$

where a and r are constants. The solution to (51) is

$$y = \left[y_0 - \tfrac{r}{a}\right] e^{-at} + \tfrac{r}{a}. \tag{52}$$

The e-folding scale then is defined by

$$\frac{y - r/a}{y_0 - r/a} = \frac{1}{e} \tag{53}$$

which is achieved by the e-folding scale value t_e

$$t_e = \frac{1}{a}. \tag{54}$$

This leads to the e-folding time scale $t_{e,T}$ for temperature (55a) and $t_{e,S}$ for salinity (55b)

$$t_{e,T} = -\gamma_T^{-1} \rho_0 c_p \Delta z_1 \approxeq 6\,\text{days} \tag{55a}$$

$$t_{e,S} = -\gamma_S^{-1} \rho_0 c_s \Delta z_1 \approxeq 31\,\text{days} \tag{55b}$$

the coefficients γ_T, γ_S, ρ_0, c_p, c_s and Δz_1 are described at the end of the previous section 3.2.2. Figure 2 shows the time evolution for temperature (left) and salinity (right) evolving from an initial value T_0 and S_0 and asymptotically approaching the restoring value T_R and S_R respectively.

Name	Symbol	Value	Units
Temperature restoring coefficient	γ_T	-80	$\mathrm{W/m^2/K}$
Salinity restoring coefficient	γ_S	-333.33	mm/day
Surface temperature e-folding scale	$t_{e,T}$	6	days
Surface salinity e-folding scale	$t_{e,S}$	31	days

Table 2: Coefficients related to the e-folding scale of the surface temperature and salinity equations.

3.3 Spatial Resolution and Time Step

Initially multiple experiments where done with a horizontal resolution Δ_h of 3 degrees in both longitudinal and latitudinal direction. This was done with a small set of vertical resolutions Δz, however the default vertical resolution from the NEMO benchmark set-up was chosen to be used for all subsequent model set-ups. The default vertical resolution consists of small grid cells near the surface of about $\Delta z = 10\,\text{m}$, increasing with depth up to about $\Delta z = 300\,\text{m}$. The time step for the coarse resolution experiments were $\Delta t = 2400\,\text{s}$.

The actual experiments that are presented in detail are carried out with 1° horizontal resolution and $\Delta t = 600\,\text{s}$ time step. The vertical resolution goes as for the coarse resolution experiments from 10 m at the surface to 300 m at 4500 m depth, the maximal depth for all

experiments.

The vertical coordinate system can be chosen in NEMO. Five options are available: z-coordinates with full step or partial step, s-coordinates, s–z hybrid coordinates and s–z hybrid coordinates with partial steps. The s-coordinates are terrain following coordinates. The z-coordinates with partial steps are chosen, this is one of the few options chosen differently to Holland (1973), where full step z-coordinates are used.

3.4 Bryan and Holland

The Bryan (1969) model was used in Holland (1973) to demonstrate the effect of variable bottom topography on the oceanic gyre circulation, and the western boundary current in particular. For the presented thesis, the Holland (1973) results are used as a guideline. Therefore a description of the cornerstones of the Bryan (1969) model is carried out; for an in depth discussion see the original papers (Bryan, 1969; Holland, 1973).

The Bryan (1969) model equations are derived using the Boussinesq approximation, hydrostatic approximation and turbulent viscosity hypothesis. The latter means that the Reynolds stress term is replaced by an eddy viscosity term while molecular viscosity is neglected. Furthermore, the rigid lid approximation is applied meaning that $w = 0$ at $z = 0$.

The eddy viscosity and diffusivity coefficients as found in Holland (1973) were also used for the presented thesis. For the eddy coefficients, see Section 3.1.2 and Table 1, for the bottom drag coefficient, Section 3.1.4. The use of identical coefficients is believed to increase the comparability with the Holland (1973) study, which is used as reference. However, the grid resolution in Holland (1973), horizontal as well as vertical, is rather crude[4] and is not adopted for the presented thesis.

[4] Roughly 3° horizontal resolution with between 6 and 10 vertical levels.

4 Methods

In the following section the numerical aspect of the streamfunction integration is introduced, which is the main indicator of the influence of variable bottom topography according to the assumed balance in Section 2. Also a method to decompose the horizontal streamfunction into three parts is presented, following the work by Greatbatch et al. (1991). This streamfunction decomposition can give more insights about the effect of variable bottom topography, which is very helpful since the effect of variable bottom topography is difficult to calculate numerically. Calculation of the BPT, and especially JEBAR, leads to extremely noisy fields, while also posing other numerical challenges.

4.1 Streamfunction

The horizontal and vertical streamfunction is calculated as follows. First the horizontal streamfunction $\Psi(y, x)$ is given by

$$\Psi(y, x) = -\sum_{i=i(x)}^{I-1} \sum_{k=1}^{K} v_{k,j,I-i} |\Delta z_{k,j,I-i} \Delta x_j|. \tag{56}$$

Here i, j, k are the indices in x, y, z-direction and x, y, z being the longitudinal, latitudinal and vertical direction. $i(x)$ is the index for a given location along the x-axis, with $i(x) \in 1, 2, \ldots, I-1$. I, K are the total number of grid points in x, z-direction. Δz is the layer thickness defined by the w-grid, the grid corresponding to the vertical velocity w. The surface elevation η is added to the surface layer, i.e. $\Delta z_{k=1}$. Δx is the distance between two v-grid points in x-direction and is constant along lines of constant latitude.

The horizontal streamfunction can also be defined using the zonal velocity u, using $\frac{\partial}{\partial y}\Psi = -U$ where U is the vertically integrated zonal velocity u.

Secondly the overturning streamfunction $\Psi(z, y)$ is defined as

$$\Psi(z, y) = \sum_{k=k(z)}^{K-1} \sum_{i=1}^{I} v_{K-k,j,i} |\Delta x_j \Delta z_{K-k,j,i}|. \tag{57}$$

Here $k(z)$ is the index for a given location along the z-axis, with $k(z) \in 1, 2, \ldots, K-1$. Δz_{K-k}, omitting the j, i dependence, is defined as $\Delta z_{K-k} = z_{K-k} - z_{K+1-k}$.

The calculation of the streamfunction was done using CDFTOOLS[5].

4.1.1 The Horizontal Streamfunction in the Presence of Cyclic Boundary Conditions

For experiments with Antarctic Circumpolar Current, i.e. cyclic boundary conditions in the x-direction, the horizontal streamfunction cannot be calculated using only the meridional velocity v, i.e. equation (56).

[5] http://servforge.legi.grenoble-inp.fr/projects/CDFTOOLS

To calculate the horizontal streamfunction in the region with cyclic boundary conditions it is possible to calculate the streamfunction from the zonal velocity u at a given longitude in the channel. Or as is done in this thesis, the streamfunction is calculated from u for the entire region south of the northern channel boundary, while the northern region is still calculated using the meridional velocity v as in equation (56). Both fields are then joined together.

4.2 Streamfunction Decomposition

In Greatbatch et al. (1991), the streamfunction Ψ is split into three parts,

$$\Psi = \Psi_W + \Psi_C + \Psi_B.$$

Here Ψ_W is the streamfunction due to wind stress in the case of variable topography but homogeneous density. Ψ_C is the difference of the former and the streamfunction as predicted from the flat-bottomed Sverdrup transport Ψ_S and relates to density compensation. Ψ_B then is the difference of the total streamfunction Ψ and Ψ_S, the effect of bottom pressure torque.

This method can be used comfortably on model output if a homogeneous ocean experiment is run parallel to the ordinary run. However, it has to be noted that, within the model, the lateral eddy viscosity is chosen large, compared to values expected for the real ocean, for the purpose of model stability. This results in an additional non-negligible streamfunction component, originating in the unresolved non-linear term, that is parameterised using a lateral eddy viscosity. Unless accounted for, this additional streamfunction component would be falsely attributed to either Ψ_C or Ψ_B in unknown proportions.

Unfortunately the error of Ψ_B cannot be separated, unless the streamfunction term due to the lateral eddy diffusion is calculated directly. Therefore, when referring to the contribution of the bottom topography to the horizontal streamfunction, an unknown deviation due to the lateral eddy viscosity is contained, i.e.

$$\Psi_B + \Psi_F = \Psi - \Psi_S$$

where Ψ_B is the effect of bottom pressure torque, Ψ_F the unknown contribution due to lateral eddy viscosity, Ψ the total streamfunction and Ψ_S the Sverdrup transport. Note that although Ψ_F is assumed to play an important role in regions with high velocity shear like the western boundary currents it is also assumed that for large areas the balance $\Psi_B = \Psi - \Psi_S$ is a sufficient approximation.

5 Experiments

This section introduces the experiments conducted for the thesis, which are structured into three groups, namely E1, E2 and AC. The experiment groups E1 and E2 both consist of eight experiments, E1–1 to E1–8 and E2–1 to E2–8, while the AC group consists of two experiments, AC–1 and AC–2. For the first two experiment groups (E1 and E2), the corresponding eight experiments are designed with increasing complexity of the bottom topography. In particular, experiments E1–1 and E2–1 have the simplest bottom topography, a flat bottom.

Experiment	Bottom Topography Modules
E1–1, E2–1	Flat Bottom
E1–2, E2–2	CM–W
E1–3, E2–3	MOR
E1–4, E2–4	CM–W + MOR
E1–5, E2–5	CM–EW
E1–6, E2–6	CM–NEWS
E1–7, E2–7	CM–NEWS + MOR
E1–8, E2–8	CM–NEWS + MOR + LB
AC–1	CM–NEWS + MOR + LB + ACC
AC–2	CM–NEWS + MOR + LB + ACC + NOS

Table 3: E1, E2 and AC refer to the experiments. E1–1 to E1–8 are the single hemisphere experiment. E2–1 to E2–8 the two hemispheric experiments. AC–1 and AC–2 are experiments with Antarctic Circumpolar Current. The bathymetry modules are — Flat Bottom: basin shape is cuboid; CM: continental margin located along the North (N), East (E), West (W) or South (S) boundaries, note that only in case of the two hemispheric experiments (E2) the southern boundary has a continental margin; MOR: mid oceanic ridge; LB: idealized Labrador Basin land mass added; ACC: idealized Antarctic Circumpolar Current, i.e. cyclic boundary conditions in a channel; NOS: idealised Nordic Seas with small overflow regions. The individual modules are discussed in Section 5.1.1 and in Section 5.1.2, their combinations.

The difference between E1 and E2 is the addition of a second hemisphere. Experiments E1–1 to E1–8 consist of a single, northern, hemisphere, following the basin design of Holland (1973), while for E2–1 to E2–8 the second, southern, hemisphere is added. The two experiments AC–1 and AC–2 are extensions to the experiment E2–8, where, by means of a channel with cyclic boundary conditions, an Antarctic Circumpolar Current is added. The domain dimensions are given in Section 5.0.1.

The differences between E1–1, E2–1 to E1–8, E2–8 and AC–1 to AC–2 are discussed in Section 5.1 where the different types of bottom topography are introduced, a complete overview is given in Table 3.

Section 5.2 introduces the wind stress, temperature and salinity forcing used for the presented thesis.

5.0.1 Domain Dimensions

The horizontal domain dimensions are, for experiments E1–1 to E1–8, a width of 52° longitude and length of 70° latitude from 1.5°S to 68.5°N; for experiments E2–1 to E2–8, a width of 52° longitude and length of 139° latitude from 70.5°S to 68.5°N; experiment AC–1 and AC–2 share a width of 83° longitude, however AC–1 shares the length with the experiments of E2 while AC–2 is extended northward, resulting in a length of 149° latitude from 70.5°S to 78.5°N.

5.0.2 Duration of Integration

The experiments E1–1 to E1–8 are integrated for 520 years while the experiments E2–1 to E2–8, AC–1 and AC–2 are integrated for 1040 years. The larger model domains are given more time to reach a near steady state. The steady state in each case is approximately reached, e.g. the Antarctic Circumpolar Current transport of experiment AC–2 reduced only by 0.1 Sv for the last 100 years of integration.

5.1 Bottom Topography

In this section the different bottom topographies used in the experiments are discussed. The different aspects of the bottom topography are arranged as modules which can be added to the most simple set-up, the flat bottomed ocean. The general idea is to evolve the bottom topography from this simple case, the flat bottomed ocean, to an idealised Atlantic Ocean.

This section is split into two parts; first Section 5.1.1 in which the individual modules are presented without a discussion of their combinations. Second, Section 5.1.2 where the modules are discussed in terms of their implementation in the experiments E1, E2 and AC. Table 3 summarises the assignments of the modules introduced in Section 5.1.1 to the experiments.

5.1.1 Bottom Topography Modules

A bottom topography module, hereafter referred to as module, is defined as a bottom topography feature that can be added to the flat bottomed ocean, e.g. a continental margin. For the presented thesis there are five modules; the Continental Margin (CM), Mid Oceanic Ridge (MOR), Labrador Sea Basin (LB), Antarctic Circumpolar Current (ACC) and the Nordic Seas basin (NOS).

CM: The Continental Margin module, CM hereafter, is short for the implementation of a sloping lateral boundary. The slope is based on a typical continental margin as found in the world oceans, however highly simplified. The CM module, as implemented here, is a series of linear sections starting at the coast with a soft slope representing the shelf area, followed by a very steep slope representing the continental slope, the deepest section, the continental rise, is split into two where the upper section, following the continental slope, has intermediate sloping and the lower section, connecting the CM to the abyssal plane, has again a soft slope, however not as soft as the shelf area.

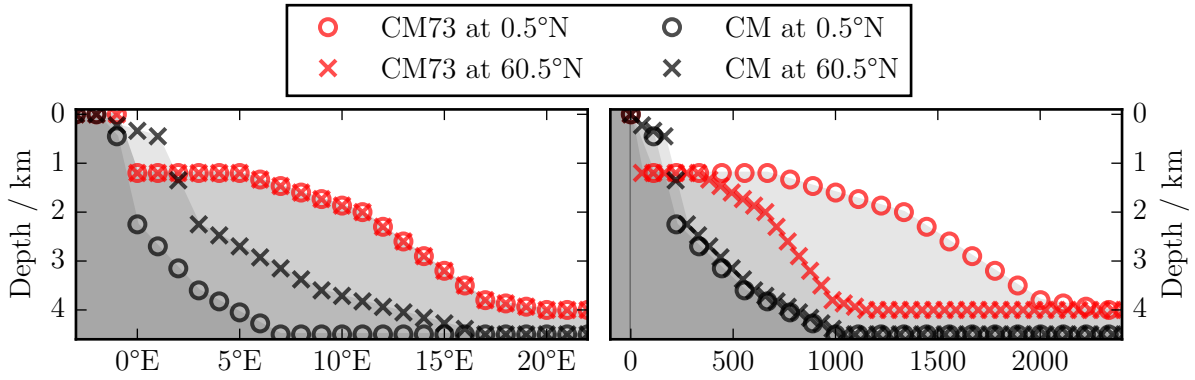

Figure 3: Continental Margin (CM) at constant latitude with depth in km on the z-axis and degrees longitude (left panel) or distance in km (right panel) on the x-axis; shown for two latitudes, 0.5°N (black circles) and 60.5°N (black crosses). For reference the bottom topography of Holland (1973) is also shown, labeled as CM73 (red circles and crosses for 0.5°N and 60.5°N respectively).

The CM is always approximately parallel to the coastline, this is particularly important for the implementation of the LB module (see below).

The width of the CM, perpendicular to the coast, is always about 1000 km, with deviations[6] of up to the grid width of 1°, and therefore approximately equidistant in contrast to the sloping bottom topography in Holland (1973) where the width of the bottom topography, along to the coast, depends on latitude, doubling in width between the equator and 60°N.

The left panel of Figure 3 shows the CM at a western boundary as a depth-longitude plot; the right panel shows the same CM as a depth-distance plot. For reference the continental margin as found in Holland (1973) is also shown, referred to as CM73.

MOR: The Mid Oceanic Ridge module, MOR hereafter, is short for the implementation of a north-south oriented ridge at the center of the basin. The MOR, like the CM, is chosen to have an equidistant slope approximately perpendicular to the north-south orientation, i.e. the MOR measures approximately equal width at any latitude. As with the CM, for the MOR the discrete nature of the grid leads to width deviations between latitudes.

The MOR measures roughly 1600 km from abyssal plane to abyssal plane (cross section), with the shallowest part, the tip, being 1800 m deep. The sloping follows a Gaussian distribution.

Note that the MOR in the single hemisphere experiments (E1–3, E1–4, E1–7 and E1–8) connects with the northern and southern boundary. For experiments with southern hemisphere (E2–3, E2–4, E2–7, E2–8, AC–1 and AC–2) the connection is present in the north, but not in the south, where the MOR ends at about 55°S featuring a slope in form of a Gaussian distribution. The termination of the MOR allows deep water formed in the southern ocean to flow in both deep ocean basins, left and right of the MOR.

[6] Deviations originate in the discrete nature of the grid and are associated to rounding during the creation of the continental margin.

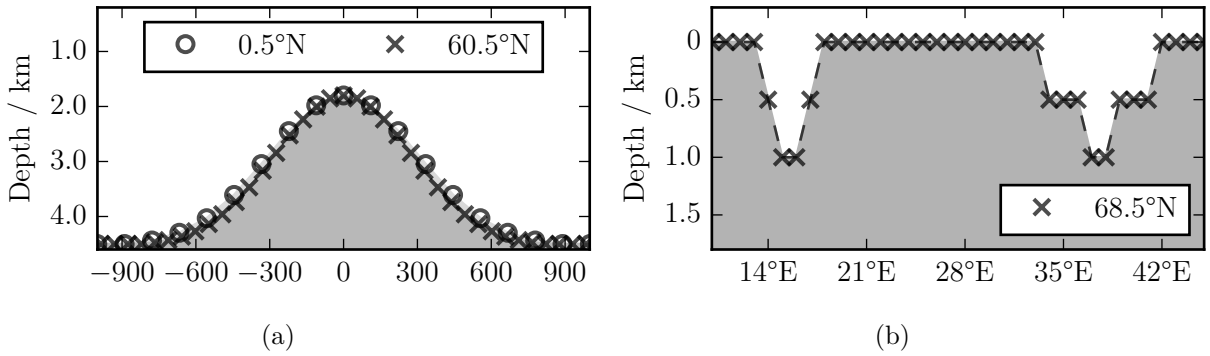

Figure 4: (a) Mid Oceanic Ridge (MOR) at constant latitude with depth in meter on the z-axis and distance from the center in km on the x-axis, shown for two latitudes, 0.5°N (circles) and 60.5°N (crosses). (b) Section of the through flow straits connecting the main ocean basin to the Nordic Seas basin (NOS) with depth in meter on the z-axis and degrees longitude on the x-axis.

LB: The Labrador Sea basin module, LB hereafter, is a land mass between 33.5°N and 57.5°N with a simple sine-wave form, and an approximately parallel and equidistant continental margin (previously introduced CM). The property of an equidistant and parallel CM was solved exactly in Cartesian coordinates and then approximated onto the spherical coordinates using nothing more than a latitude dependency of the length measured along lines of constant latitude.

The maximal width of the LB land mass, about 10° longitude is chosen far enough inwards to create a bifurcation of the f/H contours when the slope of the LB module merges with the slope of the MOR. The bifurcation point was implemented during the early stages of the thesis where it was hoped that higher horizontal resolution experiments with low eddy viscosity coefficients could be performed later on. Under lower eddy viscosity (only possible with higher horizontal resolution) bottom velocities are expected to change their pathways compared to high eddy coefficient simulations (Spence et al., 2012). Higher resolution experiments were not performed; the f/H contour bifurcation is therefore, with respect to the results in Spence et al. (2012), believed to show no prominent effect.

ACC: The Antarctic Circumpolar Current module, ACC hereafter, is a wide zonal channel with a small sill at the east entrance to the channel and cyclic boundary conditions at the domain boundaries. The channel is 28° latitude wide including a continental margin (CM module) at the southern and northern boundary. The channel adds 16° longitude in the east and 15° longitude in the west. On each side, the cyclic boundary conditions require a mirrored cell; if i is the grid-point index in x-direction, with $i = 1, 2, ..., I$ then for a model variable $\chi(i)$ the following statement is true, $\chi(1) = \chi(I-1)$ and $\chi(2) = \chi(I)$.

The sill has a height of 1200 m above the sea floor and similar to the MOR, a Gaussian shape in the zonal direction. The southern boundary of the ACC is located 5° latitude north of the southern boundary of the main basin, which leads to the northern boundary to be located at 37.5°S.

NOS: The Nordic Seas basin module, NOS hereafter, is an additional basin to the north of the main basin with two openings located in the northern boundary of the main basin, one in the east third and one in the west third of the boundary. The openings allow dense water, formed in the NOS basin, to flow into the idealised North Atlantic basin. The openings into the idealised North Atlantic basin are shown in Figure 4b. They have a maximal depth of 1000 m and a width of only a few degrees (Fig. 4b). The NOS basin beyond the openings is 3500 m deep and features a flat bottom (i.e. vertical walls). The size of the basin is about 8° latitude northward from 69.5°N to 77.5°N and has a longtidinal width of 43° longitude.

The flow through the straits from the NOS basin into the main basin turned out to be 4.3 Sv of total southward flow, and 1.6 Sv using an arbitrary[7] density criteria ($\rho > 1027.97\,\mathrm{kg/m^3}$), which captures the flow below 500—600 m in the western strait.

The dense overflow produced here, using the prior introduced arbitrary density criterion, is probably too weak to be compared to Denmark Strait overflow waters and Iceland-Scotland overflow waters (e.g. Köhl et al. (2007)). Nevertheless they might give valuable insights, and further studies can enhance the realism of any of the prior mentioned modules if necessary.

5.1.2 Combining the Bottom Topography Modules

In the introduction to this chapter (Chapter 5), the range of experiments was outlined, with single hemisphere experiments E1–1 to E1–8 and two hemisphere experiments E2–1 to E2–8, AC–1 and AC–2.

Each experiment uses a combination of the bottom topography modules, CM, MOR, LB, ACC and NOS, which are explained in the previous section (Section 5.1.1).

This section lists how the modules were combined to form each experiment, which is summarised in Table 3. Note that the bottom topography for each experiment is shown in the left plot of the figure related to the corresponding experiment; the figures are introduced and explained in Chapter 6.

The experiments E1–1 to E1–8 and E2–1 to E2–8, i.e. the single and two hemisphere experiments, exhibit a direct relation, in that each single hemisphere experiment in E1 has a two hemisphere version in E2, e.g. E1–1 and E2–1 both have a flat bottom with vertical sidewalls. The two remaining experiments, AC–1 and AC–2 are extensions of E2–8 and have no single hemisphere representation since they involve the Antarctic Circumpolar Current region, requiring the two hemisphere set-up.

The single and two hemisphere experiments, E1–1 to E1–8 and E2–1 to E2–8, use the modules CM, MOR and LB.

E1–1 and E2–1, as already mentioned are the flat bottom experiments, i.e. no module is used. This basic experiment is a classical set-up and represents the most basic understanding of the large scale oceanic circulation as described by the flat-bottomed Sverdrup relation.

[7] Using a density class criterion from Köhl, Käse, Stammer, and Serra (2007), i.e. $\rho > 1027.8\,\mathrm{kg/m^3}$ would encompass the entire transport through the straits as the density minimum in the straits is almost exactly $1027.8\,\mathrm{kg/m^3}$ (the maximum is $1028.02\,\mathrm{kg/m^3}$).

Experiments E1–2 and E2–2 use the CM module at the western boundary (CM–W). Adding the variable topography along the western boundary is the important step done in Holland (1973) leading to new understanding of the importance and impact of the former. The importance of this experiment will be discussed in more detail along with the presentation of the results in Section 6.1.2.

Experiment E1–3 and E2–3 use the MOR module.

Experiment E1–4 and E2–4 combine the CM–W and MOR modules, i.e. joining the modules of the two previous experiments together.

Experiment E1–5 and E2–5 again use only the CM module, however now along the eastern and western boundaries (CM–EW).

Experiment E1–6 and E2–6 add the northern boundary CM to the previous experiment with eastern and western CM; note that only for the two hemisphere experiment (E2–6) the southern boundary exhibits the CM, while the single hemisphere experiment (E1–6) the southern boundary coincides with the equator where the boundary is kept as a vertical wall.

Experiment E1–7 and E2–7 now unite the MOR with the CM along all model boundaries. Note again, the single hemisphere experiment (E1–7) does not exhibit a CM along the southern boundary (i.e. the equator).

Experiment E1–8 and E2–8 now implements the LB module into the previous experiments, E1–7 and E2–7 respectively.

Experiment AC–1, the first experiment only available with two hemisphere, adds the ACC module to the previous two hemisphere experiment E2–8.

Experiment AC–2 is the final experiment, adding the NOS module, which means that AC–2 incorporates all modules, i.e. continental margins all around the basin (CM–NEWS), the mid oceanic ridge (MOR), the Labrador Sea basin (LB), the Antarctic Circumpolar Current (ACC) and the prior mentioned last module, the Nordic Seas basin (NOS).

With this, we have a recognisable, but still drastically simplified, Atlantic Ocean. There obviously is much room to enhance the realism of the North Atlantic without the need to use real bottom topography. For example, adding a Mediterranean, or addressing the asymmetry of the equatorial region, where Africa reaches westwards north of the equator, and South America could be better represented by a triangular shape, with a slight south-east sloping coastline across the equator, the area where in the Atlantic Ocean the North Brazil Current Ring Shedding takes place. Also, modifying the MOR, e.g. changing the two rather simplistic characteristics it has now, one, that it is straight along the north-south axis, and two, that it has always the same height.

This general topic of improving the model set-up will be picked up in the conclusions, where the possibilities for improvements will be expanded using the new insight from the results presented in the following chapter, and more so the author's improved knowledge about models in general.

5.2 Forcing

There are three surface forcing fields that need to be specified in order to reproduce and extend the work of Holland (1973), namely the surface wind stress, surface heat flux and surface freshwater flux. All forcing fields are chosen to be zonally symmetric, i.e. a forcing field f solely depends on the meridional coordinate y, $f = f(y)$ where y is measured positive northwards. This is a common choice. First of all, it simplifies the problem while still capturing the main features that are believed to drive the gyre circulation and the Southern Ocean circulation, i.e. the mid latitude westerlies, the low latitude trade winds, the subtropical and subpolar gyre salinity contrast and the general equator-pole temperature gradient. Furthermore, it ensures comparability and consistency with Holland (1973). Note that the surface stress is given directly as wind stress ($\boldsymbol{\tau}|^s = \boldsymbol{\tau}_{\text{wind}}$), while both surface temperature and surface salinity are forced using a surface restoring method with restoring fields for temperature (T_R) and salinity (S_R), see Section 3.2 for more details.

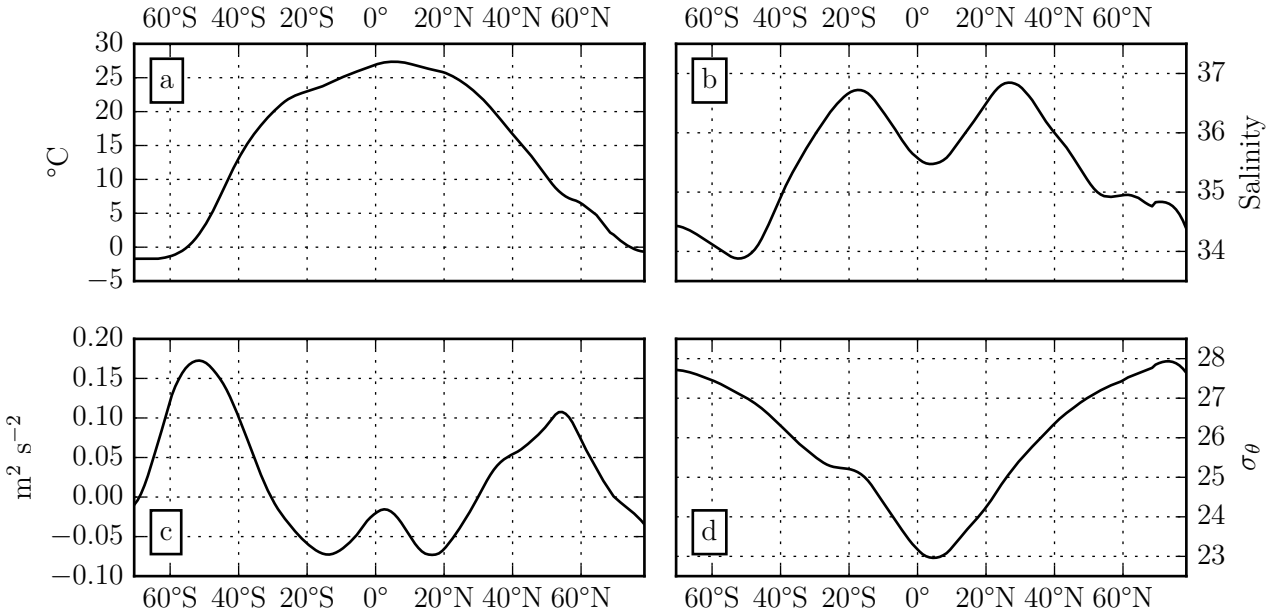

Figure 5: Surface forcing fields $f(y)$ where y is latitude and f are the (a) surface restoring temperature T_R in degrees Celsius (°C); (b) surface restoring salinity S_R; (c) surface wind stress $\boldsymbol{\tau}|^s$ in square meter per square second ($\mathrm{m^2/s^2}$); and (d) the surface density associated with T_R and S_R, i.e. $\rho = \rho(T_R, S_R, p = 0)$ in units of $\sigma_\theta \equiv \rho - 1000\,\mathrm{kg/m^3}$.

Each forcing field ($\boldsymbol{\tau}_{\text{wind}}$,$T_R$,$S_R$) was created from observational data using zonal medians and a polynomial filter, see Section 5.2.1 for details. Figure 5 shows the surface forcing fields: wind stress $\boldsymbol{\tau}_{\text{wind}}$ (Fig. 5c); temperature T_R (Fig. 5a); salinity S_R (Fig. 5b); and the surface density associated with the temperature T_R and salinity S_R, i.e. $\rho = \rho(T_R, S_R, p = 0)$ (Fig. 5d).

In the next subsection the method by which the forcing fields were created are presented.

5.2.1 Creation of the Surface Forcing Fields

Forcing field were created from observational data. The wind stress was taken from the ERA-Interim dataset (Dee et al., 2011) and for temperature and salinity, data from the World Ocean Atlas (WOA, Locarnini et al., 2013; Zweng et al., 2013) was used.

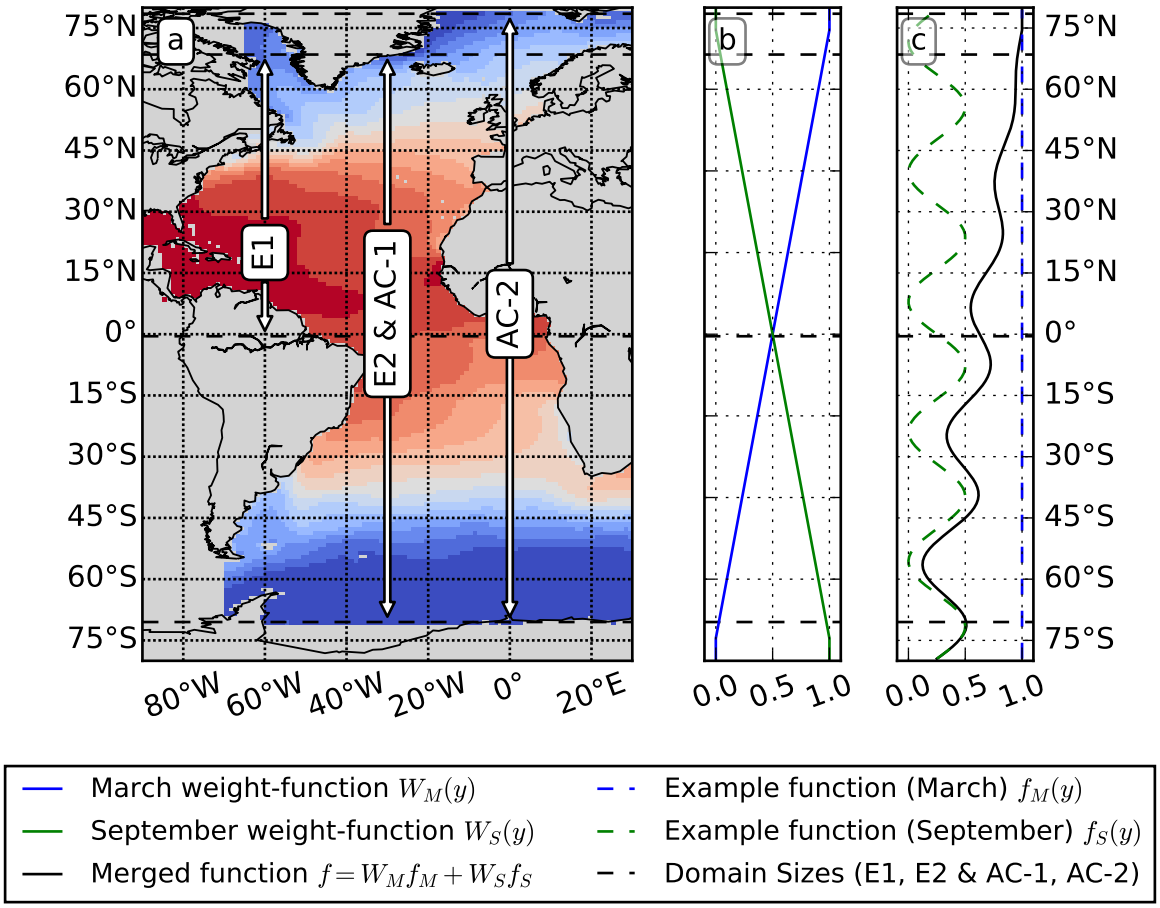

Figure 6: a) Area of input forcing data (coloured area, shown is the climatological mean of September, from the World Ocean Atlas), arrows indicate domain sizes; b) Weighting function W(y) for March and September data, applied to the zonal median for the corresponding month; c) An example of the weighting, solid black line is the weighted average of the dashed blue and green lines.

The forcing fields are time independent and only a function of the meridional axis. In each case, the winter hemispheres polar conditions were considered essential, since deep convection to drive an overturning was desired. The following steps were taken as a procedure to create each forcing field from the corresponding dataset.

1) The first step was to obtain climatological data for each hemisphere's final winter month, March for the northern hemisphere and September for the southern hemisphere. The last winter month was used since water temperatures are usually the coldest at the end of winter.

For the World Ocean Atlas (WOA, Locarnini et al., 2013; Zweng et al., 2013) climatological data is available. The climatology used in this thesis is based on the time period from 1955 to

2012 and only surface data was used. For the ERA-Interim dataset (Dee et al., 2011) monthly averaged data are available, therefore monthly data for the period from 1979 to 2015 were averaged, using an arithmetic mean, to form a climatology. The resulting climatological data will in the following be referenced as $f_{M,G}$ and $f_{S,G}$ where G denotes that the data is global, M stands for the March climatological data and S for September respectively. The differentiation between wind stress, temperature or salinity will be omitted since the following procedures are the same for all three forcing fields.

2) From the global data, $f_{M,G}$ and $f_{S,G}$, the data of the Atlantic Ocean region were used, since the basin in Holland (1973) was originally a representation of the North Atlantic and for the presented thesis the basin was developed to resemble some aspects of the Atlantic Ocean, e.g. a Labrador Sea basin, but more so the overturning driving conditions in the North Atlantic were of interest.

Thus the Atlantic was cropped out of the global data and kept within the colored area seen in Figure 6a, demonstrated for the example of temperature. At this stage, the data might be named $f_{M,A}$ and $f_{S,A}$.

3) From the Atlantic data, $f_{M,A}$ and $f_{S,A}$, the zonal median was taken. The median is a robust averaging method, and is defined as

$$\tilde{x} = \begin{cases} x_{\frac{n+1}{2}} & , n \text{ odd} \\ \frac{1}{2}\left(x_{\frac{n}{2}} + x_{\frac{x}{n}+1}\right) & , n \text{ even} \end{cases} \tag{58}$$

where $\tilde{x}$ is the median, n is the total number of data points, and x are the sorted data points, here sorted from small to large values of either temperature, salinity or wind stress. In words, the median is the middle data point of a sorted data set, and might be used as an alternative to the arithmetic mean. The median is chosen as the best option for the zonal average due to robustness against outliers, which is favourable since there are several outliers in the Atlantic zonal sea surface data, e.g. from the Mediterranean outflow or at the Newfoundland area where very cold waters are located on the shelf and in the Gulf of St. Lawrence. In the following the median of $f_{M,A}$ and $f_{S,A}$ will be denoted simply $f_M(y)$ and $f_S(y)$.

4) The final step is to merge the March and September medians, $f_M(y)$ and $f_S(y)$, since only a single time independent forcing is required for all intended purposes. To merge the two medians a simple linear weighted average is used

$$f(y) = W_M(y)f_M(y) + W_S(y)f_S(y) \qquad , \text{with } W_M(y) + W_S(y) = 1 \tag{59}$$

where $W_M(y)$ and $W_S(y)$ are the weighting values for March (M) and September (S) respectively, with values between 0 (no influence) and 1 (full influence). $W(y)$ is linear between $\pm 75°$ latitude and is chosen to favour the winter hemisphere, therefore for latitudes greater than $|75°|$ the corresponding winter (summer) hemisphere is weighted with 1 (0). Note that only for the EXP-NOS configuration does the latitude exceed 75° latitude (see Section 5.0.1 and Fig. 6a).

Figure 6b shows both $W_M(y)$ and $W_S(y)$. Furthermore in Figure 6c a minimal example is given, merging an example function for March $f_M = c_1$ and September $f_S = c_2 \sin(c_3 y) + c_4$, where $c_{1,2,3,4}$ are constants.

Some remarks about this method. Since the weighting is linear, the summer and winter hemispheres influence both hemispheres, resulting in steeper gradients at mid latitudes and a wider, less amplified tropical region. However, this is only noticeable for temperature; both salinity and wind stress show less seasonal differences and therefore show less sensitivity to the averaging (not shown).

6 Results

In this chapter the results of a subset of the performed experiments are presented. Shown are eight experiments with one hemisphere, the northern hemisphere (E1–1 to E1–8), the same number of experiments extended by a southern hemisphere, i.e. two hemispheres (E2–1 to E2–8), and two experiments with an Antarctic Circumpolar Current (AC–1, AC–2). The experiments are explained in Section 5 on page 25*ff*, and the experiment settings are summarized in Table 3 on page 25.

The validation of the model, with the goal to demonstrate that the presented results are in fact sensible follow-up experiments to the results presented in Holland (1973), is placed in the Appendix A.

6.0.1 Figures

In this chapter, the main figures are place at the end of the text and only supplementary figures are found within the main text. The main figures are explained in the following.

Figures 13 to 20 (page 52 to 55) show the experiments with one hemisphere (E1–1 to E1–8), Figures 21 to 28 (page 56 to 63) the experiments with two hemispheres (E2–1 to E2–8), and Figures 29 and 30 (page 64 and 65) experiments with Antarctic Circumpolar Current (AC–1 and AC–2). All figures share the following structure.

The left plot in each figure shows the bottom topography of the corresponding experiment as color shading, overlain by f/H contour lines in white, here f is the Coriolis parameter defined by $f = 2\Omega \sin(\phi)$, where Ω is the Earth's angular velocity and ϕ the latitude, and H is the ocean depth measured downwards from the level $z = 0$. The x-coordinate is in degrees longitude, the y-coordinate in degrees latitude. The middle plot shows the horizontal streamfunction (color shading with black contours), i.e. the streamfunction defined analytically by equation (20) and numerically by equation (56); here the bottom topography is superimposed as dashed white contour lines. As in the left figure, the x and y-coordinates are in degrees of longitude and latitude. The right plot in each figure shows the meridional overturning (color shading with black contours), numerically defined by equation (57). Here the x-coordinate is the ocean depth measured downwards from the level $z = 0$ in km, the y-coordinate is the latitude.

In each figure depicting either the horizontal streamfunction or the meridional overturning, positive (negative) values represent transport along lines of constant streamfunction in clockwise (anti-clockwise) direction. Positive (negative) values are shown as solid (dashed) contour lines.

6.1 Experiments with Single Hemisphere (E1)

In this section the experiments with a single hemisphere, i.e. experiments E1–1 to E1–8, are presented. These eight experiments are shown in Figures 13 to 20 (page 52 to 55); note that a generalised figure description is done in Section 6.0.1. For more information on the experiments see Section 5, page 25*ff* and Table 3, page 25.

6.1.1 E1–1: Flat Bottom

We start with the flat-bottom case, i.e. E1–1 (Fig. 13 on page 52). The horizontal streamfunction (middle plot in Fig. 13), represents here the reference for the following experiments. The result is close to the flat-bottomed Sverdrup transport, excluding the western boundary, where friction is required to close the streamlines.

The expected pattern is a three gyre system where the gyre separation is located close to the zeros in the wind stress curl. The used zonal wind stress results in an untypical low in the subtropical gyre, at about 40°N. Furthermore, it has to be noted that the tropical gyre, is relatively strong. Here after tropical gyres are defined as the gyre equator-wards of the subtropics. Tropical gyres are known to appear in the horizontal streamfunction. A very early example is the solution for the Pacific Ocean presented in Munk (1950, Fig. 2); two other examples, showing the global Sverdrup and Stommel solution, can be found in the text book "Ocean Dynamics" (Olbers et al., 2012, Fig. 14.6 and 14.7, Chapter 14) and a final example, the global barotropic streamfunction in Hughes and de Cuevas (2001, Fig. 4, last panel). Note however, that the tropical gyre is usually not the center of interest, as is the case here.

The meridional overturning consists of one large cell driven by downwards motion on the northern model boundary and is as expected relatively close to Holland (1973).

6.1.2 E1–2: Western Continental Margin

Introducing the western continental margin (CM–W; Fig. 14 on page 52) leads to increased strength of the subtropical gyre, together with an arm of the subtropical gyre reaching far north along the sloping bottom topography. This result is comparable to the Holland (1973) solution; however the implemented continental margin is narrower which results in a weaker subtropical gyre in comparison to Holland (1973).

The enhanced subtropical gyre, first described in Holland (1973), comes from the deep flow up the slope at the western boundary, which comes from the zonal overturning arising from the north-south density contrast. The near bottom upward motion is associated with southward flow in the form of the deep western boundary current, which follows from linear vorticity relation (39) and the integral form (40) (Holland, 1973). Maps of the near bottom zonal and vertical velocities support this (not shown). The vertical velocities near the bottom will prove to be important for the experiments that include a southern hemisphere and variable bottom topography (E2–2 to E2–8, AC–1 and AC–2).

The meridional overturning exhibits, compared to the experiment with variable bottom topography in Holland (1973), a weak response to the introduction of the western CM. An experiment where the bottom topography in Holland (1973) was reconstructed, shows (See Appendix A) the same results as can be seen in Figure 5a and b in Holland (1973), i.e. the contour lines of the meridional overturning are stretched southwards along the upper part of the respective bottom topography (for the bottom topography see Holland (1973) or red circles/crosses in Figure 3).

Here, for E1–2, the meridional overturning exhibits only a very weak southward stretching

of the contour lines along the upper parts of the bottom topography. In fact the difference is only visible in a very close comparison and furthermore is obscured by an overall weakening of the meridional overturning in E1–2 compared to E1–1.

6.1.3 E1–3: Mid Oceanic Ridge

Implementing a Mid Oceanic Ridge (MOR; Fig. 15 on page 53) to the flat bottomed ocean leads to a strong extension of the subtropical gyre both eastward across the MOR and northward along the MOR into the subpolar region, which suppresses the subpolar gyre. The extended subtropical gyre reaches farthest north along the eastern side of the MOR, comparable to what was previously seen in E1–2 along the western continental margin. The northward transport is strongest on the western side, and on top of the MOR, while east of the MOR the transport returns south. The southward transport starts off the MOR in the northeastern corner of the model and climbs the eastern side of the MOR until it reaches the top of the MOR at around 10°N; however the strength of the southward transport has already declined drastically along the way.

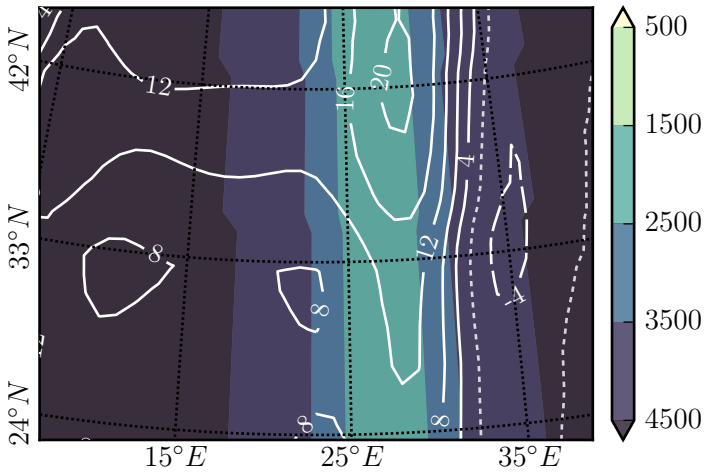

Figure 7: Streamfunction contribution from the bottom pressure torque Ψ_B (white contours), estimated as the difference between the total transport streamfunction and the flat-bottomed Sverdrup transport (see section 4.2), over bottom topography (color shading). The shown region is part of the subtropical gyre featuring the MOR; the contour interval is 4 Sv; the zero contour is omitted; solid (dashed) contours are positive (negative), i.e. clockwise (counter clockwise) rotational transport.

To the west of the MOR the streamfunction weakens again, however the subtropical gyre west of the MOR, is also stronger compared to the flat bottomed case (E1–1). Looking at the bottom pressure torque induced streamfunction, derived following the definition in Greatbatch et al. (1991), reveals that the bottom pressure torque induced streamfunction contribution Ψ_B of the MOR has a net effect on the streamfunction west of the MOR. Figure 7 shows Ψ_B for an area in the subtropical region, over the MOR. The streamfunction contribution Ψ_B is positive, i.e. strengthens the clockwise transport of the subtropical gyre, from 10°N to the northern boundary, for the region west of the MOR.

6.1.4 E1–4: Western Continental Margin and Mid Oceanic Ridge

For this experiment the bottom topography of E1–2 and E1–3 was combined, i.e. both the western continental margin and the Mid Oceanic Ridge are present (Fig. 16 on page 53).

This experiment is on the surface a simple superposition of those two previous experiments, showing both the increased transport of the western boundary current and the island of positive streamfunction above the MOR, both reaching northward into the subpolar gyre. However, the entire region of the subtropical gyre is a bit weaker compared to the experiment with MOR alone.

The meridional overturning is rather unremarkable. It exhibits the sharp corner reaching southward, as can be seen in the experiment with western continental margin alone (E1–2), but also reaches a bit deeper and also has more transport. Still, the meridional overturning of the experiment with MOR only (E1–3) is stronger.

6.1.5 E1–5: Western and Eastern Continental Margin

Adding the eastern continental margin to experiment E1–2, i.e. having a western and an eastern continental margin (Fig. 17 on page 54), first of all results in the expected pattern along the western boundary and also into the interior subtropical gyre. However, the subpolar gyre is affected noticeably. For one, along the eastern continental margin, the streamfunction exhibits a southward reaching arm, the anti-symmetric mirror to the western boundary arm reaching northward into the subpolar gyre. Also mirrored is the off coast counter extension of the subpolar gyre in the west, i.e. the subtropical gyre is dragged northward off the coast into the subpolar gyre (compare to E1–2).

6.1.6 E1–6: Western, Eastern and Northern Continental Margin

The northern continental margin, introduced here into the previous experiment E1–5, i.e. featuring the continental margin module along the northern, eastern and western boundary (CM-NEW; Fig. 18 on page 54), results in drastic changes to the subpolar gyre. The subpolar gyre is now as strong as the subtropical gyre and pushes southward along the western boundary into the subtropical gyre.

Most important here, as the source of this change, is probably the change of the meridional overturning which shows a major shallowing and weakening. The reason for the shallowing of the meridional overturning very likely is purely blocking of the deep convection. An inspection of the mixed layer depth (Figure 8 shows the mixed layer depth in the convection region for E1–5, upper panel and E1–6, lower panel) reveals that the largest mixed layer depth (deeper than 2 km) in previous experiments was located in the region now largely obscured by bottom topography, which renders convection down to the largest depth impossible. Nevertheless, deep convection can and does take place, resulting in strong deep currents along the topography. The f/H contours, which are now connected in the north by the northern continental margin, allow the flow to relatively easily follow the bottom topography at every depth from every region

where deep convection takes place.

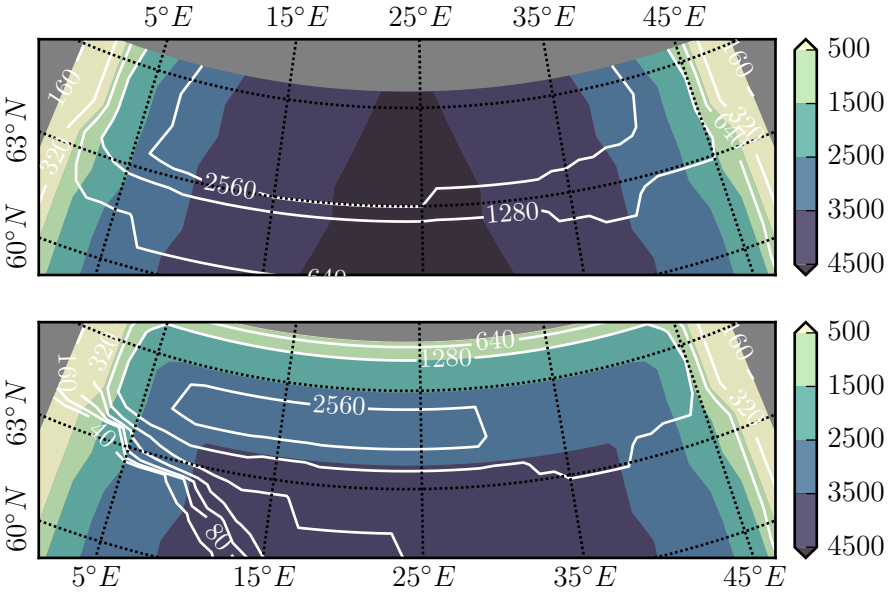

Figure 8: Mixed layer depth (white contours) over bottom topography (color shading). The mixed layer contours start at 40 m and increase by a factor of 2 for each successive contour line (40×2^n; $n \in 0, 1, \ldots$). Shown is the northern boundary of the experiments E1–5 (upper panel) and E1–6 (lower panel).

The deep western boundary current for this experiment is horizontally displaced, about 750 m higher on the continental rise (lower part of the continental margin), compared to the previous experiments, likely due to blocking of deep convection at the origin of the deep western boundary current, combined with the connection of the f/H contours in the convection regions with the western boundary.

Coming back to the horizontal streamfunction, here a comparison to the flat bottomed ocean seems fit, since the general pattern matches better compared to the previous experiments. However, the transports associated with those patterns, i.e. the transport strength of the individual gyres are much larger, with the exception of the tropical gyre which is, all in all, very inert.

6.1.7 E1–7: Western, Eastern, Northern Continental Margin and Mid Oceanic Ridge

Now incorporating the MOR, as seen in E1–3 into the basin of experiment E1–6, i.e. having a continental margin in the north, west and east (CM–NEW) together with a MOR (Fig. 19 on page 55), has a surprising small impact. Surprising, because in E1–03 and E1–4, the subtropical gyre shows a major second extremum above the MOR, which reaches into the subpolar gyre.

By contrast, the implementation of the MOR into the complexer (CM–NEW) bottom topography leads to not more than a local minimum in the subpolar gyre above the MOR. The meridional overturning is almost the same as in the previous experiment (E1–6). And the subtropical gyre only shows minor modulations of the streamlines above the MOR.

The vertical structure of the velocities above the MOR, comparing experiment E1–7 to E1–3 or E1–4, shows that the velocities above and along the MOR are greatly reduced (not shown). In the previous experiments (E1–3 and E1–4), the flow had to climb the full height of the MOR, while in this experiment (E1–7) the deep convection is shallower and the westward flow can cross the MOR further to the north. This is well visualised by the f/H contours, as a f/H contour originating from the northeastern corner in E1–3 or E1–4 crosses the MOR at about 20°N, while in E1–7, the f/H contours from the convection region already cross the MOR at around 45—50°N.

6.1.8 E1–8: Western, Eastern, Northern Continental Margin, Mid Oceanic Ridge and Labrador Sea

The last addition to the northern hemisphere is the Labrador Sea basin (LB; Fig. 20 on page 55). Adding the LB again results only in minor modulations to both the horizontal streamfunction and the meridional overturning. The meridional overturning becomes intensified from around the LB landmass's peak northward while weakened southward of that region in comparison to the prior experiment (E1–7). The horizontal streamfunction shows the obvious deflection as the water masses have to follow the land mass, however neither the transports of the major gyres, nor the patterns away from the region in direct proximity of the land mass, changes.

It was hoped that this experiment would approximate the influence of the Labrador Sea in the Atlantic Ocean, producing deep convection and maybe forcing the westward North Atlantic Current, between the subtropical and subpolar gyre, off the coast, creating for example a rudimentary north-west corner, a difficulty for modern climate and general ocean circulation models (e.g. Drews, Greatbatch, Ding, Latif, & Park, 2015).

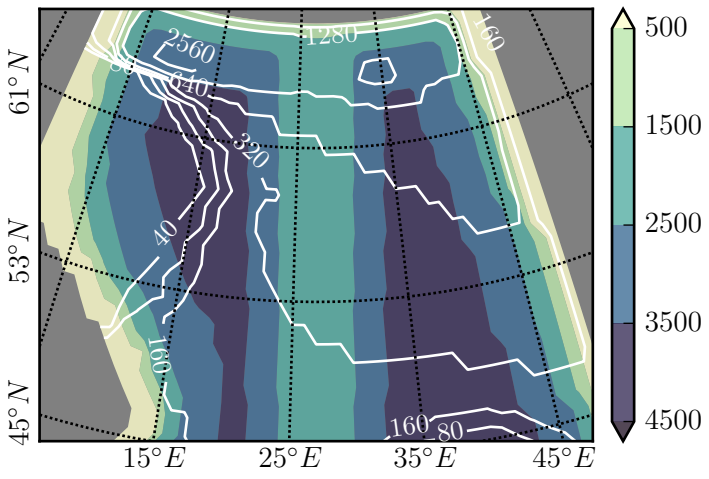

Figure 9: Mixed layer depth (white contours) over bottom topography (color shading). The mixed layer contours start at 40 m and increase by a factor of 2 for each successive contour line (40×2^n; $n \in 0, 1, \dots$). The maximum mixed layer depth is just above 3 km. Shown is the subpolar region of experiment E1–8.

However, neither of those expectations was met. Investigating the mixed layer depth (an example is shown in Figure 9) together with vertical density profiles (not shown) reveals that

immediately to the north of the LB land mass a patch with well stratified water masses is located. This patch originates in the mixture of surface warming by the surface boundary condition (remember that the e-folding scale for the surface temperature restoring is only 6 days (Section 3.2.3)), and the freshwater forcing in the central subpolar gyre. The result is a fresh and slightly warmed whirl, right where deep convection was hoped to take place. It is difficult to say whether the temperature or salinity plays the major role during the formation. However, it is clear that after the formation of the stable stratified patch, the low salinity dominates the stratification. This follows from the fact that within the patch the temperature drops below the temperature of neighboring regions (not shown), which would increase the density, however the low salinity compensates for the low temperature, resulting in stable stratification, i.e. the region of minimal mixed layer depth.

This issue in the experiment design could only be addressed by modifying the forcing fields to ensure convection takes place in the LB. In the Atlantic Ocean, the Labrador Sea is isolated by the north-east tilted mean storm track together with the continental winds lowering the temperatures in the Labrador Sea significantly compared to the other side of the Atlantic Ocean, near the European continent, supplied by the North Atlantic Current. Further, the separation of the Gulf Stream at Cape Hatteras, which allows fresh water to flow between the Gulf Stream and the western coastline, blocks the mixing of warm water into the subpolar gyre along the western coast. In fact, the saline water has to take a long way around the North Atlantic, before it mixes into the subpolar gyre. Taking this information into account, a future implementation of an idealised Labrador Sea would need to address the zonal inhomogeneity of the northern North Atlantic in both wind stress and buoyancy forcing.

6.1.9 Summary

The past sections presented the single hemisphere experiments E1–1 to E1–8 (Figs. 13 to 20 on page 52 to 55). The first experiment, E1–1, i.e. the flat-bottomed ocean foremost presents the reference for most comparisons as it is closely described by the flat-bottomed Sverdrup transport. Equally, the meridional overturning in E1–1, as it describes the overturning undisturbed by bottom topography, also provides a suitable reference.

Experiment E1–2 is the first experiment with variable bottom topography, i.e. a continental margin at the western boundary (CM–W), and the experiment best compared to the original work of Holland (1973) and therefore an important connection between Holland (1973) and the subsequent work of this thesis. This experiment shows good qualitatively resemblance to the historic work (Holland, 1973), as the subtropical gyre transport increases notably which is associated with an increase of the western boundary current transport. The importance of this experiment lies in the increased western boundary current transport as this is one of the major discrepancies between the Sverdrup transport and measurements from the North Atlantic's western boundary current, the Gulf Stream (e.g. Gill, 1971).

The following experiment, E1–3, introduced the Mid Oceanic Ridge (MOR). The MOR is often assumed to only have a small effect on the horizontal transport streamfunction (Wunsch

& Roemmich, 1985; Willebrand et al., 2001; Eden & Olbers, 2010). However, for the two experiments E1–3 and E1–4, the MOR resulted in a major transport increase of the subtropical gyre above the MOR, reaching up to the northern boundary.

Experiment E1–5, as might be expected, is quite comparable to E1–2, suggesting that the eastern continental margin might be in fact rather unimportant. However, the two hemisphere variant of E1–5, i.e. E2–5, challenges this conclusion (section 6.2.5).

Adding a continental margin to the northern boundary, as done in experiment E2–6, turned out to be the most important change for the subpolar gyre, leading to a drastic increase in transport strength as well as lateral area. Furthermore, the implementation of the northern continental margin is the first bottom topography module that changes the meridional overturning significantly, as now the regions with deep convection are partly blocked by bottom topography, the meridional overturning is shallower as well as weaker.

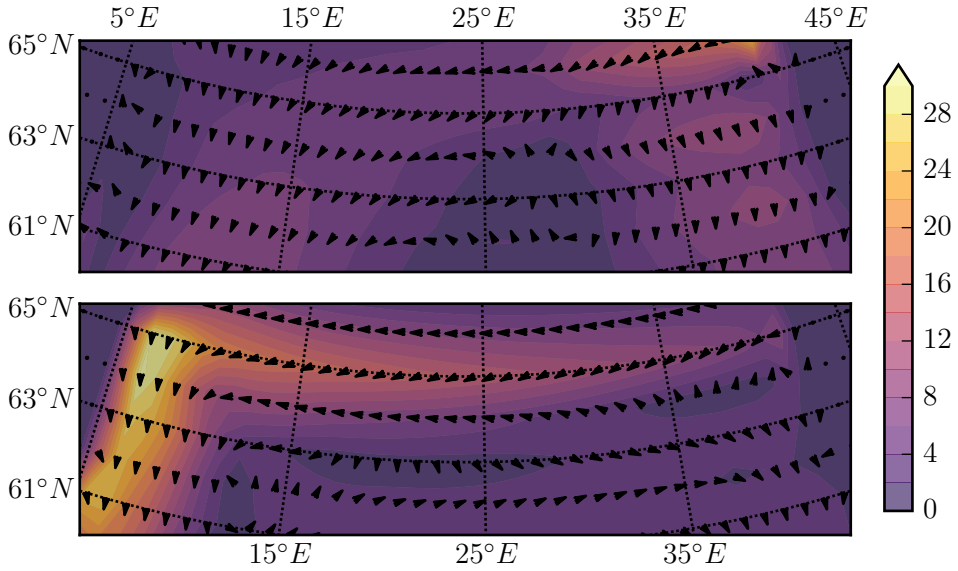

Figure 10: Horizontal velocities in about 2.6 km depth (2517—2809 m) for the northern boundary of the model domain to illustrate the change in velocities from E1–5 to E1–6, i.e. the introduction of the northern continental margin; with longitude on the x-axis and latitude on the y-axis; the magnitude of the horizontal velocities as color shading, in millimeter per second (mm/s); the direction of the horizontal velocities as black arrowheads. Upper panel: E1–5. Lower panel: E1–6.

Associated with the northern continental margin are f/H contours that connect for the first time the western boundary with the eastern boundary at mid depth. The connection of the f/H contours along the northern boundary, together with the suppression of deep convection, resulted in a drastic change of the deep currents, most notably creating a very intense deep western boundary current, which in addition to the western boundary also flows along the northern boundary. While without the northern boundary, the deep western boundary current was placed at the bottom of the western continental margin, then rising up the former while flowing south, now the deep western boundary current starts already quite high on the continental margin, exhibiting increased strength. Figure 10 shows the horizontal flow field

for the lowest layer in which the deep western boundary current connects all the way to the north-eastern corner of the model domain (i.e. in 2517—2809 m depth).

The last two single hemisphere experiments, E1–7 and E–8 are very comparable, due to the underestimated effect of the Labrador Sea basin (LB). Furthermore, the combined inclusion of the MOR into the set-up of E–6 also leads only to minor changes. The MOR in combination with the continental margins in the west, east and north, results in a weakening of the subpolar gyre above the MOR, however no other consistent changes.

6.2 Experiments with Two Hemispheres (E2)

This section presents experiments with two hemispheres, i.e. experiments E2–1 to E2–8. Those eight experiments are shown in Figures 21 to 28 (page 56 to 63); note that a generalised figure description is done in Section 6.0.1. For more information on the experiments see Section 5, page 25*ff* and Table 3, page 25.

6.2.1 E2–1: Flat Bottom

Starting with the Flat Bottom case, i.e. E2–1 (Fig. 21 on page 56).

Adding the southern hemisphere to the flat bottom experiment E1–1, creating E2–1, has practically no effect on the northern hemisphere's horizontal streamfunction. However the meridional overturning changes substantially, the southern meridional overturning cell reaches far into the northern hemisphere. The horizontal streamfunction is not affected by the changed meridional overturning, compare Fig. 13 and Fig. 21.

It has to be emphasized that the northern hemisphere's meridional overturning almost comes to a halt. The drastic reduction of the northern meridional overturning follows from the dominance of the southern meridional overturning which pushes dense waters into the northern hemisphere's deep ocean, filling the ocean with dense waters effectively blocking deep convection.

Note that there is an unexpected overturning anomaly at the deep equator, which is a persistent feature across experiments with two hemispheres (E2). This will be addressed in Section 6.4.

6.2.2 E2–2: Western Continental Margin

Adding the western continental margin (CM–W; Fig. 22 on page 57), the southern hemisphere exhibits the results expected from the single hemisphere experiment (E1–2); a strong subtropical gyre extended polewards along the western boundary displacing the subpolar gyre. The northern hemisphere displays a completely different picture. The subpolar gyre is roughly as expected, but the subtropical gyre is not. The subtropical gyre appears more like in the flat bottomed case but even weaker. The coastal extension along the western boundary is however, still visible even though it is very weak.

In the description of experiment E1–2 (Section 6.1.2) it was already hinted at the importance of the zonal velocities in the deep ocean. Effectively, the reverse of the meridional overturning in the deep ocean of the northern hemisphere, driven from the southern hemisphere, is connected to a reverse of the zonal overturning, leading to a reverse of the zonal velocities near the bottom. While in E1–2 the velocities over the sloping bottom topography was upslope, it now is downslope in the northern hemisphere. From the linear vorticity (39) and the integral form (40) follows that with the reverse of the near bottom vertical velocities in the northern hemisphere comes also a reverse of the direction of the meridional flow, now flowing northward. The southern hemisphere still behaves like E1–2, as expected since the meridional overturning in the southern hemisphere is equivalent to E1–2, in that there is deep convection near the poleward boundary with polewards surface currents and equatorwards deep currents. Again associated with the meridional overturning is a zonal overturning, which in the southern hemisphere, as in E1–2, is westwards in the deep ocean with upslope velocities.

Remarkable is also the tropical gyre, especially the northern tropical gyre which is 6 Sv stronger than the subtropical gyre. The southern tropical gyre, although with expected strength, is detached from the coast sitting just off the region with sloping topography.

6.2.3 E2–3: Mid Oceanic Ridge

The Mid Oceanic Ridge (MOR) in an otherwise flat-bottomed ocean (Fig. 23 on page 58) displays similar results as the previous experiment (E2–2), in that the southern hemisphere is comparable to the corresponding single hemisphere experiment (E1–3), while the northern hemisphere exhibits a strong tropical gyre, a subtropical gyre close to the flat bottomed solution, and a weak subpolar gyre. Here the subpolar gyre is too weak to be resolved by the contour lines, as the maximum transport is about 3 Sv.

A closer look at the region above the MOR at the zero line of the horizontal streamfunction, at the separation of subpolar and subtropical gyres, shows that for both the southern and northern hemisphere this zero line runs from a north-western to a south-eastern location. This suggests that the flow along the MOR in the north goes southwards and eastwards over the MOR. This is the opposite to what was seen in the single hemisphere experiment (E1–3).

The bottom velocities (not shown) support this claim, as for most of the southern hemisphere the bottom velocities are westward, while for the majority of the northern hemisphere the bottom velocities are eastward. The vertical profile of the zonal velocity, at a latitude of around 45°N (not shown), shows westward near surface flow (upper 500 m) followed below by eastward flow (down to 1500—2000 m), below this the zonal velocity is generally eastwards again. This is reflected by the near bottom vertical velocities, which are upwards at the western side of the MOR and downwards at the eastern side, opposite to what was the case for E1–3.

The tropical gyres, northern and southern, again exhibit an asymmetry, with a weaker southern tropical gyre.

6.2.4 E2–4: Western Continental Margin and Mid Oceanic Ridge

Combining the western continental margin and MOR (Fig. 24 on page 59) results in a horizontal streamfunction pattern that is a combination of E2–2 and E2–3. Near the western boundary the pattern of E2–2 dominates, while along the MOR and the interior around, the pattern of E2–3 dominates. The effects seem local, and combining one of the bottom topography modules with the other leads only to weak modifications of the other in its corresponding region of influence.

Summarising, the meridional overturning is mostly as before (similar to E2–3). The horizontal streamfunction is comparable to E2–2 near the western boundary and to E2–3 near the MOR.

6.2.5 E2–5: Western and Eastern Continental Margin

Continental margin at the eastern and western boundary (CM–EW; Fig. 25 on page 60); this experiment again shows that the southern hemisphere, where the meridional overturning is deep and strong, is comparable to the results previously obtained by the single hemisphere experiment with eastern and western continental margin (E1–5). However, unlike in E1–5 the strength of the southern subpolar gyre is greatly increased from the previous experiments with two hemispheres. The bottom pressure torque component of the streamfunction derived from Greatbatch et al. (1991) shows the great influence of the eastern boundary on the southern subpolar gyre. The bottom pressure torque adds to the horizontal streamfunction from the eastern boundary in the whole region from the southern boundary up to the central region of the subtropical gyre at about 30°S. Figure 11 shows this for part of the southern hemisphere, i.e. the northern part of the subpolar gyre and southern part of the subtropical gyre.

In the northern hemisphere the subtropical gyre is greatly inflated, almost completely taking over the area where the subpolar gyre would be expected. However, the transport strength of the gyre is still comparable to the flat bottomed case leading to the conclusion that the dominance of the southern meridional overturning is the reason of the weak northern subpolar gyre.

The northern meridional overturning roughly doubles in strength, however the total volume transport is at 4.9 Sv still low compared to the southern Meridional Overturning with 14.7 Sv.

6.2.6 E2–6: Western, Eastern, Northern and Southern Continental Margin

We now consider the effect of adding a continental slope along the northern and southern boundaries (Fig. 26 on page 61). Here, again the southern hemisphere is as expected from E1–6, as well as the southern meridional overturning, which becomes a bit shallower, probably related to deep convection as the region where the mixed layer depth reaches depth of more than 3500 m shrinks slightly. Note however, that for the southern hemisphere, the continental margin along the southern boundary does not block the complete area where the mixed layer depth had the largest depth; about half of the area where deep convection could be expected is not obscured by bottom topography.

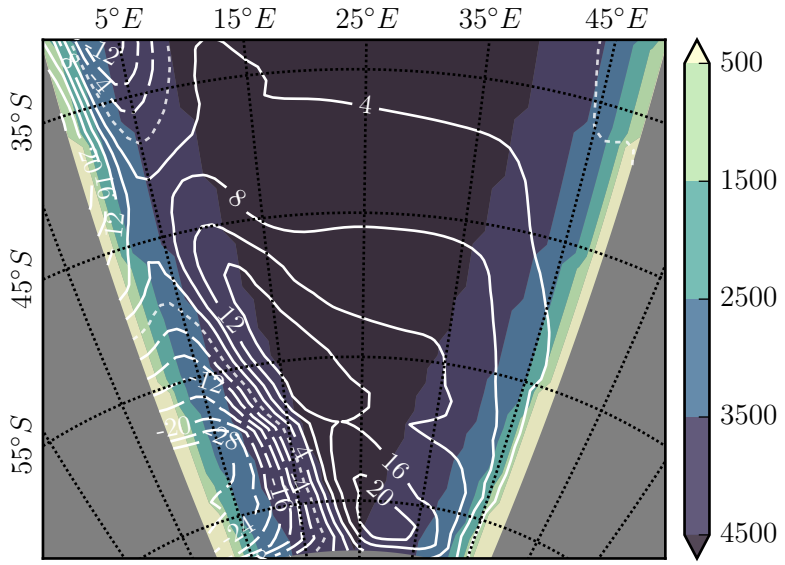

Figure 11: Streamfunction contribution of the bottom pressure torque Ψ_B (white contours), estimated as the difference between the total transport streamfunction and the flat-bottomed Sverdrup transport (see section 4.2), over bottom topography (color shading). The shown region is part of the southern subpolar and subtropical gyre of experiment E2–5; the contour interval is 4 Sv; the zero contour is omitted; solid (dashed) contours are positive (negative), i.e. clockwise (counter clockwise) rotational transport.

Moving on to the northern hemisphere, the introduction of the northern continental margin strengthens the subpolar gyre, as we saw with a single hemisphere.

6.2.7 E2–7: Western, Eastern, Northern, Southern Continental Margin and Mid Oceanic Ridge

Here, the MOR is implemented into the previous basin set-up, i.e. continental margins all around (Fig. 27 on page 62). This has little impact on the meridional overturning and leads only to modification in the horizontal streamfunction.

However, the modification to the northern subtropical gyre can be recognised. The weakening as the subtropical gyre closes in at the MOR (from the west) with a weak streamfunction maximum east of the MOR. This approximate pattern can also be found in Figure 1 of Greatbatch et al. (1991), where the horizontal transport streamfunction of the North Atlantic is shown. As the streamfunction closes in from the western side onto the Mid Atlantic Ridge the streamfunction decays, and increases again slightly onto the eastern side of the Mid Atlantic Ridge.

6.2.8 E2–8: Western, Eastern, Northern, Southern Continental Margin, Mid Oceanic Ridge and Labrador Sea

Finally, the the Labrador Sea basin (LB) is added to the set-up of E2–7, i.e. having continental margins all around, a MOR and the LB land mass at the western boundary (Fig. 28 on page 63).

Here, as was discussed for E1–8, the implementation of the LB module has unfortunately

little influence on the deep water production in the region that was thought to represent the Labrador Sea. The reason for the absence of deep water formation is found in a well stratified area exactly where the deep convection of the Labrador Sea would be expected. Possible reasons for the stable stratification were already discussed in Section 6.1.8.

6.2.9 Summary

The first experiment in E2, i.e. the flat-bottomed case E2–1, represents the flat-bottomed Sverdrup transport (excluding the western boundary region), showing the undisturbed wind driven gyre circulation. However, the meridional overturning is in a completely new state, forced by the hemispheric asymmetry of the thermohaline forcing, resulting in a dominant southern overturning cell which invades a large portion of the northern deep ocean. The northern meridional overturning reduces down to 3 Sv; for comparison the overturning of E1–1 was 14 Sv and E2–1's southern hemisphere has -20.7 Sv (the sign marks the overturning's rotational direction).

The meridional overturning does not change significantly throughout all experiments E2, while the implementation of the eastern and northern continental margin (CM–NE) increases the transport strength of the northern cell by almost a factor of 2, it is still extremely low compared to the southern cell and all single hemisphere experiments (E1).

One aspect, which is also prominent in each two hemispheric experiment (E2), is an anomaly in the meridional transport located at depth on the equator, which will be discussed in detail in section 6.4 (below).

Following the stepwise implementation of the bottom topography modules, it becomes evident that the southern hemisphere now takes the role of the single hemisphere, i.e. the southern hemispheres horizontal streamfunction patterns are comparable to the corresponding experiment in E1. In contrast the northern hemisphere of experiments E2 show only rudimentary aspects of their single hemisphere counterpart.

A striking example is the northern subtropical gyre in the experiment E2–2 (featuring CM–W), where the northward extension of the gyre along the upper part of the continental margin can still be seen; however it is very weak compared to E1–2 or the southern hemisphere of E2–2, and arguably more important is the center of the gyre, where the increase associated with the western continental margin as expected from Holland (1973) is absent, and the transport maximum of the subtropical gyre is even below the flat-bottomed Sverdrup transport.

According to Holland (1973), the meridional overturning is connected to a zonal overturning in a specific way, i.e. the dominant southern hemisphere's overturning, invading the northern hemisphere, results in an anti-clockwise zonal overturning in the deep ocean, which results in downslope velocities below the subtropical gyre, where in E1–2 and E2–2's southern hemisphere the velocities are upslope, resulting in a weakening of the subtropical gyre by the western boundary continental margin.

Similar to E2–2, the implementation of the MOR (E2–3), shows a new pattern for the northern hemisphere. This time the subpolar gyre is affected, as it is almost entirely suppressed. This is a result seen in every experiment where the bottom topography interferes with the

central or eastern part of the subpolar gyre; e.g. the implementation of the eastern continental margin in E2–5 (CM–EW).

The combination of northern CM and MOR results in recovering of the area occupied by the subpolar gyre, the transport strength however, is still very weak.

Returning to experiments E2–2 (CM–W) and E2–4 (CM–W + MOR), in comparison with experiments with eastern boundary CM (CM–E), here an interesting point shows up, as for each experiment where the western CM is included, the eastern CM however not, the subtropical gyre is below the Sverdrup transport, i.e. flat-bottomed case (E2–1). It is only when the eastern boundary is added that the northern subtropical gyre is equally strong compared to E2–1. This shows once more that the western boundary may only have a small contribution. However, in the case where the subtropical gyre is that weak it adds a non-negligible contribution of about 4 Sv.

A last, rather small change compared to E1, is the effect of the MOR on the subtropical gyre in cases with CM's on each boundary. While the southern hemisphere's subtropical gyre is more or less unaffected, as was the case for the corresponding single hemisphere experiments, the northern hemisphere's subtropical gyre exhibits a notable weakening along the MOR, which however results in no weakening of the subtropical gyre west of the MOR.

Experiments that where excluded from the thesis, featuring an alternative surface forcing, underline the role of the meridional overturning for the northern hemisphere. Those experiments exhibited a stronger northern hemisphere overturning, still weaker than in the corresponding single hemisphere experiment. The stronger northern hemisphere overturning in turn resulted in patterns of the horizontal streamfunction that were more comparable to their single hemisphere counterpart. Furthermore, the equivalent experiment to E2–5 shows an even stronger effect of the eastern CM, resulting in the strongest northern subtropical gyre for that entire set of two hemisphere experiments (no ACC experiments were performed).

6.3 Experiments with Antarctic Circumpolar Current (AC)

This section presents experiments with two hemispheres and an Antarctic Circumpolar Current, i.e. experiments AC–1 and AC–2. Those two experiments are shown in Figures 29 and 30 (page 64 and 65), note that a generalised figure description is done in Section 6.0.1. For more information on the experiments see Section 5, page 25 and Table 3, page 25.

6.3.1 AC–1: Antarctic Circumpolar Current

The addition of the Antarctic Circumpolar Current (ACC; Fig. 29 on page 64) via a channel in the southern hemisphere with cyclic boundary condition will be presented here. The ACC is implemented in the bottom topography set-up of the experiment with Mid Oceanic Ridge (MOR) and continental margins at all boundaries (CM–NEWS) including the Labrador Sea basin (LB), i.e. experiment E2–8.

We start with the meridional overturning, as this is the major change apart from the existence of the ACC. The implementation of the ACC greatly increases the strength of the

northern hemisphere's meridional overturning, although not deepening it. The northern meridional overturning reaches now further south, crossing the equator, reaching to around 15°S. The southern meridional overturning exhibits what is known as the Deacon Cell (Döös & Webb, 1994), although the Deacon Cell appearing here is rather large and deep. A density coordinate based meridional overturning was not calculated; calculating the meridional overturning in density coordinates shows the artificial nature of the Deacon cell (Döös & Webb, 1994).

The remainder of the southern meridional overturning is split by the Deacon Cell and greatly reduced in strength. However, the meridional overturning still reaches far into the northern hemisphere.

Moving on with the horizontal streamfunction, here the northern hemisphere recovers from the suppressed state in the prior experiments with a southern hemisphere added (i.e. E2–2 to E–8). With an ACC the northern subtropical gyre strengthens together with the subpolar gyre. The subpolar gyre still shows signs that the deeper part is not reached by the northern meridional overturning. This is demonstrated by the southward extension of the subpolar gyre along the eastern side of the MOR. In the single hemisphere experiment E1–8 the southward extension of the subpolar gyre takes place along the western side of the MOR.

Note, the implementation of the ACC also reduced the asymmetry of the northern and southern tropical cell. The northern tropical cell is still stronger, however the southern cell is now roughly as strong as in the flat bottomed case and furthermore, it is not off set from the coast anymore.

6.3.2 AC–2: Antarctic Circumpolar Current and Nordic Seas Basin

Finally, we come to the last modification of the basin (Fig. 30 on page 65), here a flat bottomed square basin is added to the north of the main ocean basin, with two openings. This feature is named Nordic Seas basin (NOS) as it allows very dense water masses to flow slowly into the mid-depth of the northern subpolar gyre.

The meridional overturning shows that the implementation of NOS strengthens the former even further, as now the northern meridional overturning connects with the Deacon Cell in the south. In addition, the subpolar gyre strengthens also further.

6.4 Note on Deep Equatorial Anomaly

Experiments E2–1 to E2–8 show an overturning anomaly at depth on the equator, and it is not known that NEMO has problems with the equator in general, i.e. creating an artificial overturning. Furthermore, this feature also is present in a purely density driven simulation (not shown), eliminating the zonal wind stress as potential source.

In Weaver and Sarachik (1990) the use of lateral Reynolds number $Re_l = U\Delta_l/A^{lm}$, lateral Peclet number $Pe_l = U\Delta_l/A^{lT}$, vertical Reynolds number $Re_v = W\Delta_v/A^{vm}$ and vertical Peclet number $Pe_v = W\Delta_v/A^{vT}$ are proposed to determine the stability of a model, in the context of unrealistic overturning at depth near the equator in a single hemisphere experiment. Here U is a lateral, and W a vertical representative velocity; Δ_l and Δ_v are the lateral and vertical grid

spacing, respectively; the coefficients $A^{\alpha\beta}$ are the eddy viscosity and diffusivity coefficients, see Table 1. The lateral Reynolds and Peclet numbers as well as the vertical Reynolds number, satisfy the proposed stability criterion, i.e. $Re_l, Pe_l, Re_v < 2$, although the lateral Peclet number has regions where the criterion is not fulfilled, i.e. surface flow in the tropics (first model layer) and the core region of the western boundary current. However, in Weaver and Sarachik (1990) it is argued that there is no necessity the lateral Peclet number to satisfy the criterion.

The vertical Peclet number satisfies the stability criterion ($Pe_v < 2$) for large areas of the ocean. Only in the deep ocean where the vertical resolution increases up to 300 m in combination with strong vertical velocities, is the criterion not met. This is exactly the case for the deep equatorial ocean, where north and south of the equator, vertical velocities of up to 1 m/day take place, resulting in a vertical Peclet number multiple times larger than the stability criterion boundary of 2, e.g. in Figure 12 the entire area encompassed by white contours (i.e. vertical velocity contours) does not fulfill the stability criterion.

In conclusion, the vertical stability at depth on the equator based on the stability criterion presented in Weaver and Sarachik (1990) can be questioned.

Now, assuming the deep equatorial overturning anomaly is not caused by model failure, a possible cause of the deep equatorial anomaly could be the high meridional symmetry of the bottom topography across the equator combined with the meridional antisymmetry of the Coriolis deflection. Assuming the prior premise, the deep flow patterns seem reasonable, Figure 12 shows the velocities for the deepest layer (lower panel) and a layer at about 3 km depth (upper panel) of experiment E2–5. As can be seen in Figure 12, the deep western boundary current follows the continental slope, and in contrast to the deep western boundary current in subtropical and subpolar regions (not shown), it is completely pressed against the slope with only little vertical extend. The interior horizontal flow of the bottom layer (Fig. 12, lower panel) exhibits a clockwise rotational tendency about the equatorial line, the deep western boundary current being the northward branch and eastward velocities north of the equator and westward south of the equator. In the upper layer (Fig. 12, upper panel) the interior pattern is reversed, now exhibiting a counter-clockwise rotational flow field about the equatorial line, with eastward velocities south of the equator and westward velocities north of the equator and the southward closure just off the deep western boundary current, now separated from the deep western boundary current.

At the bottom the interior flow is northward, leading to westwards deflection of the flow south of the equator and eastwards deflection north of the equator. In contrast the upper layer exhibits generally southward flow across the equator in the interior, the Coriolis deflection now induces a westward velocity component north of the equator and eastward south of the equator.

Associated with the horizontal flow is a strong vertical component, shown in Figure 12 as white contours in meters per day (m/day). The vertical velocities have the same direction in both layers, i.e. north of the equator the interior flow is upwards and the vertical flow in the western boundary current is downwards; the pattern is reversed south of the equator. The

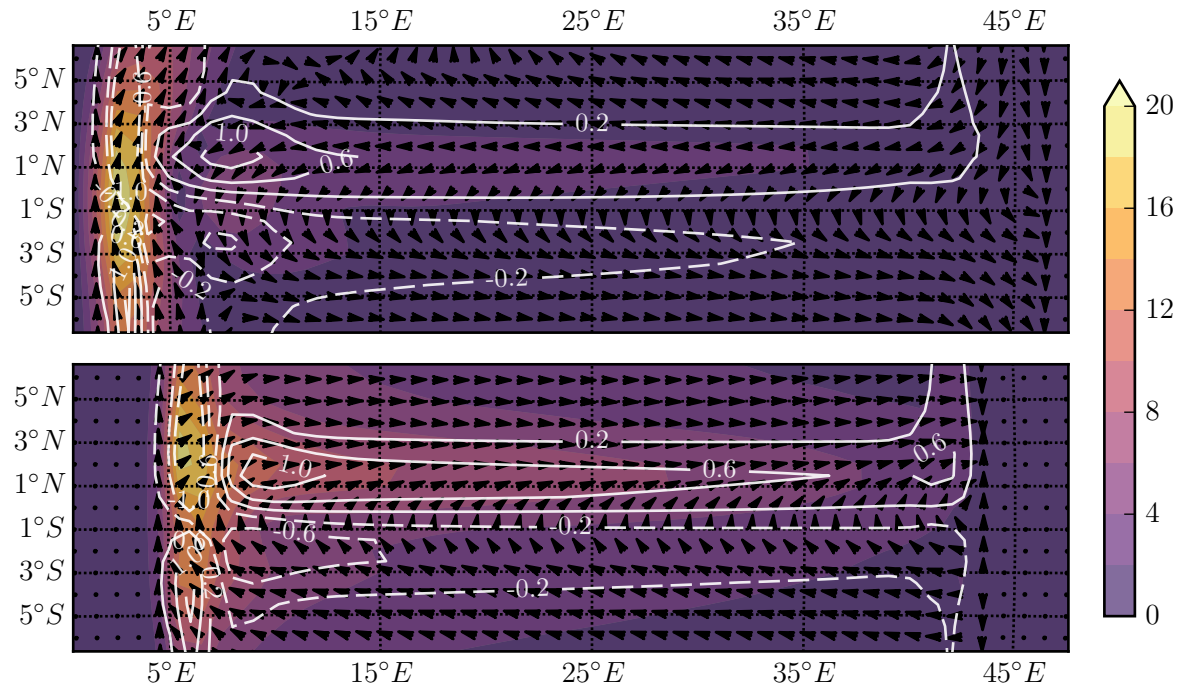

Figure 12: Equatorial velocities on the example of experiment E2–5 with longitude on the x-axis and latitude on the y-axis; the magnitude of the horizontal velocities as colored contours, in millimeter per second (mm/s); the direction of the horizontal velocities as black arrowheads; and the vertical velocities as white contours, in meters per day (m/day), solid (dashed) contours are upwards (downwards) velocities. Upper panel: interior layer (2809—3104 m depth), vertical velocities are from the layer's lower boundary. Lower panel: the bottom layer (4000—4500 m depth), vertical velocities are from the layer's upper boundary. Note, local layer thicknesses may vary due to the partial-steps bottom topography.

symmetry axis (anti-symmetry) is slightly south of the equator. The upwards velocities are likely to provide the southward flowing waters in the upper layer, as the lateral supply seems limited, the interior flow north of 3°N already turns north, and the southwards oriented eastern boundary flow is extremely weak.

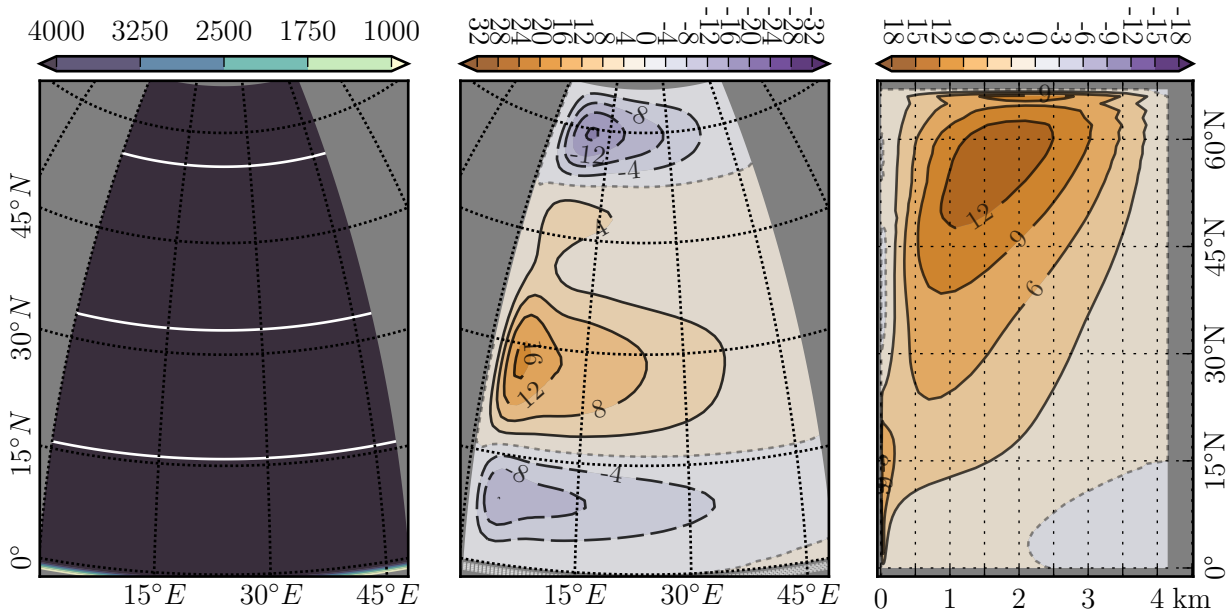

Figure 13: Experiment E1–1. Left: Bottom topography (color shading) and f/H contours (white); Middle: Horizontal streamfunction (color shading with black contours) and Bottom topography (white, dashed); Right: Meridional Overturning (color shading with black contours).

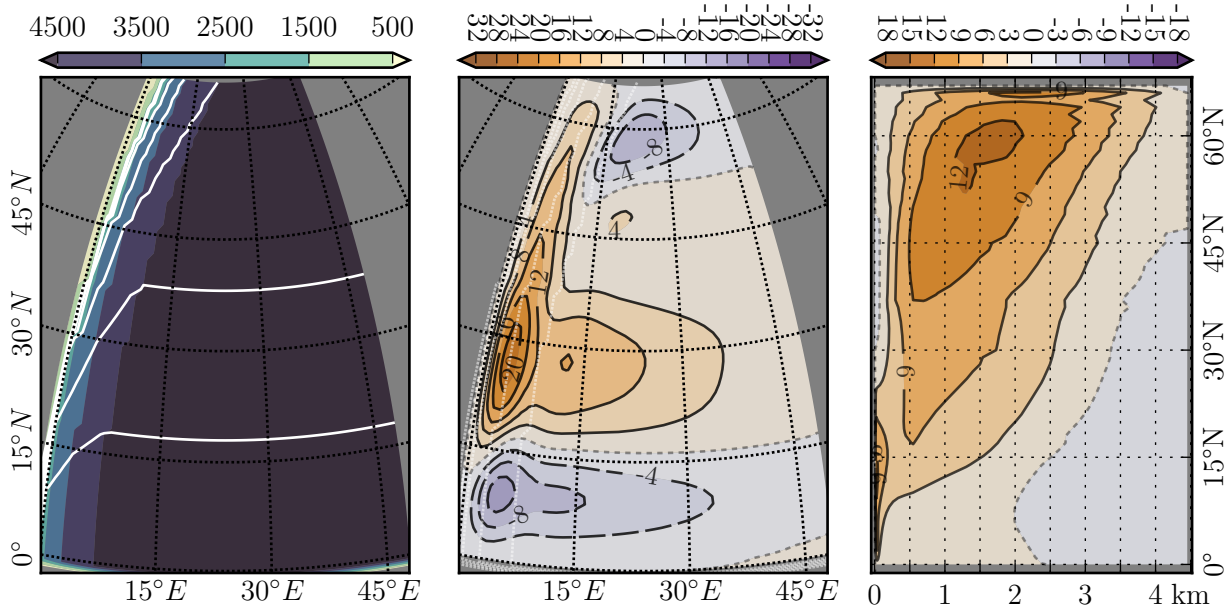

Figure 14: Experiment E1–2. Left: Bottom topography (color shading) and f/H contours (white); Middle: Horizontal streamfunction (color shading with black contours) and Bottom topography (white, dashed); Right: Meridional Overturning (color shading with black contours).

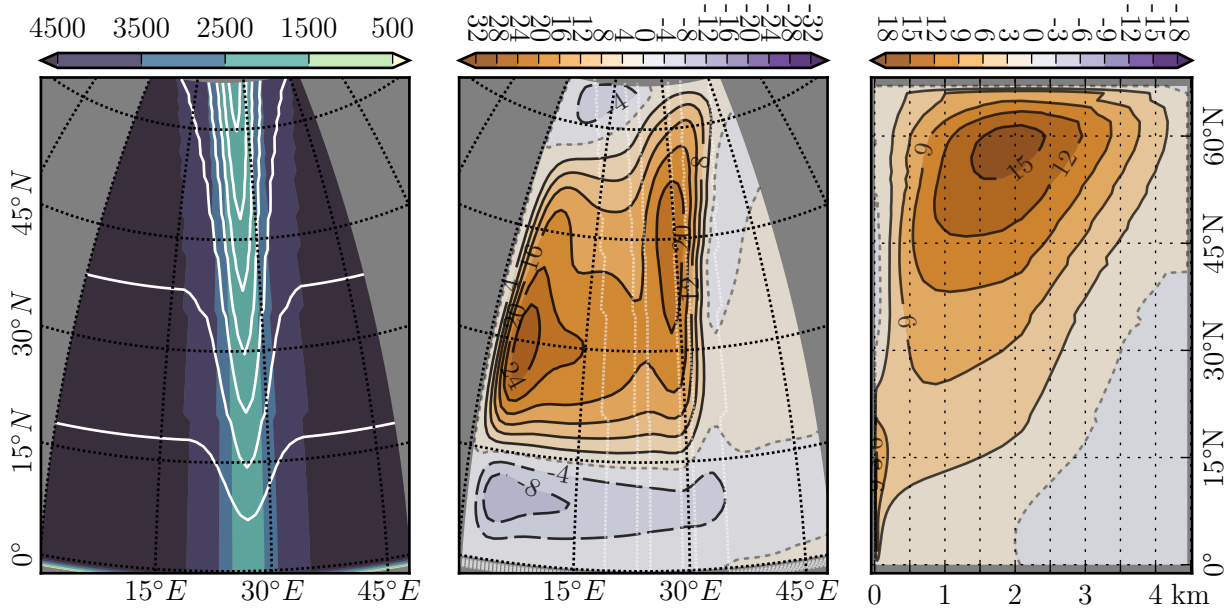

Figure 15: Experiment E1–3. Left: Bottom topography (color shading) and f/H contours (white); Middle: Horizontal streamfunction (color shading with black contours) and Bottom topography (white, dashed); Right: Meridional Overturning (color shading with black contours).

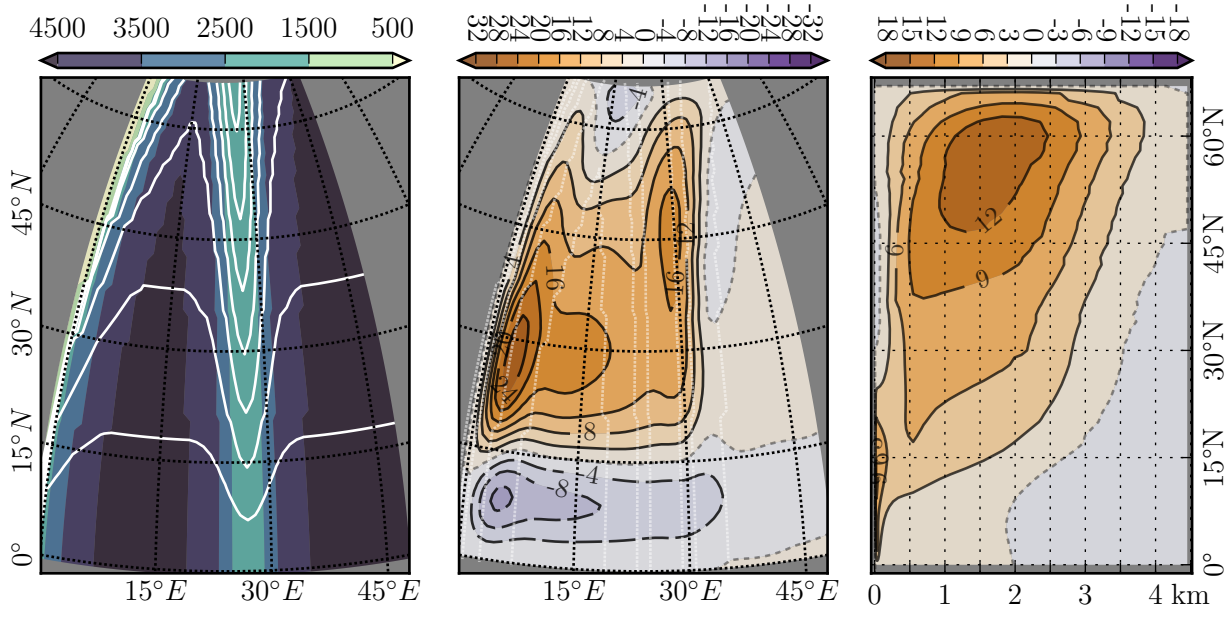

Figure 16: Experiment E1–4. Left: Bottom topography (color shading) and f/H contours (white); Middle: Horizontal streamfunction (color shading with black contours) and Bottom topography (white, dashed); Right: Meridional Overturning (color shading with black contours).

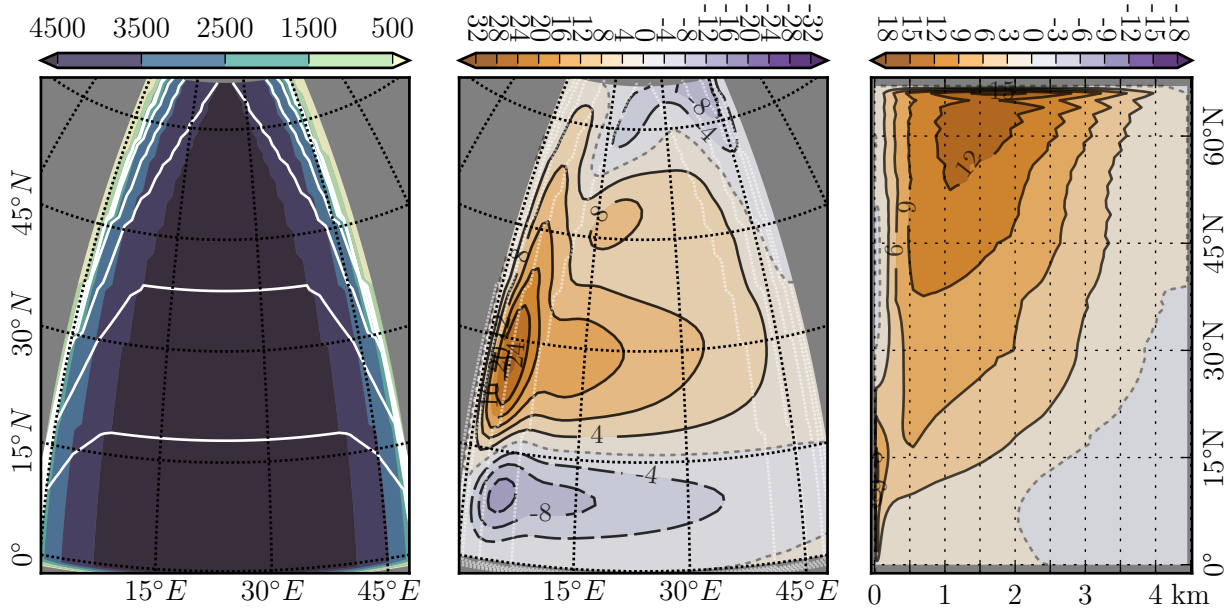

Figure 17: Experiment E1–5. Left: Bottom topography (color shading) and f/H contours (white); Middle: Horizontal streamfunction (color shading with black contours) and Bottom topography (white, dashed); Right: Meridional Overturning (color shading with black contours).

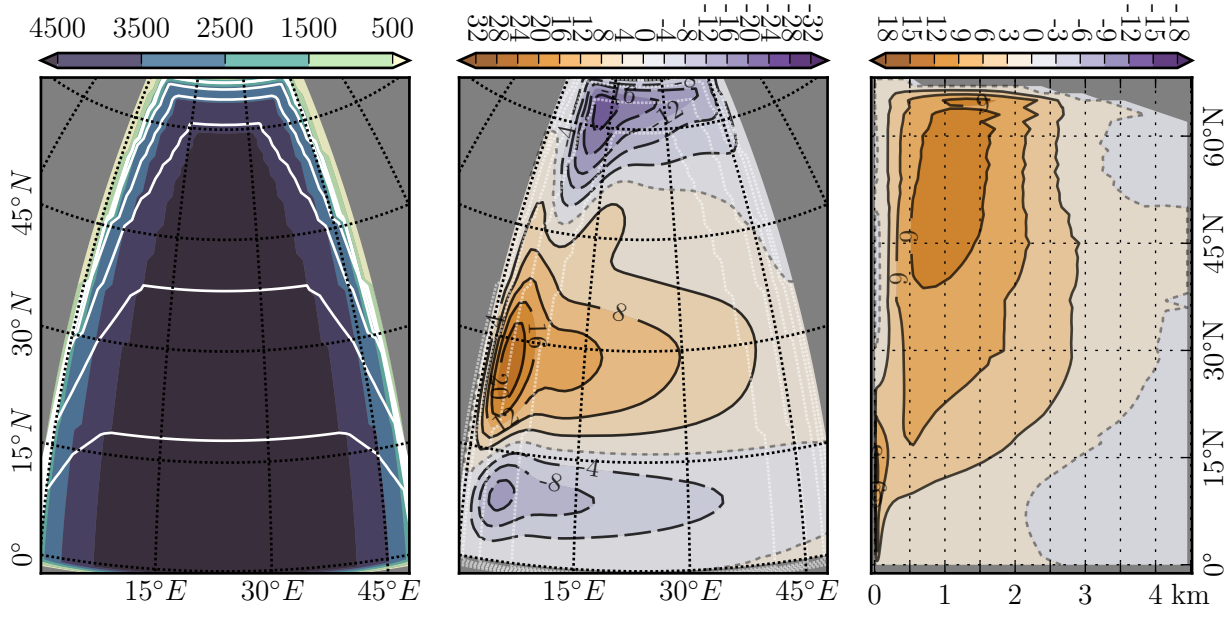

Figure 18: Experiment E1–6. Left: Bottom topography (color shading) and f/H contours (white); Middle: Horizontal streamfunction (color shading with black contours) and Bottom topography (white, dashed); Right: Meridional Overturning (color shading with black contours).

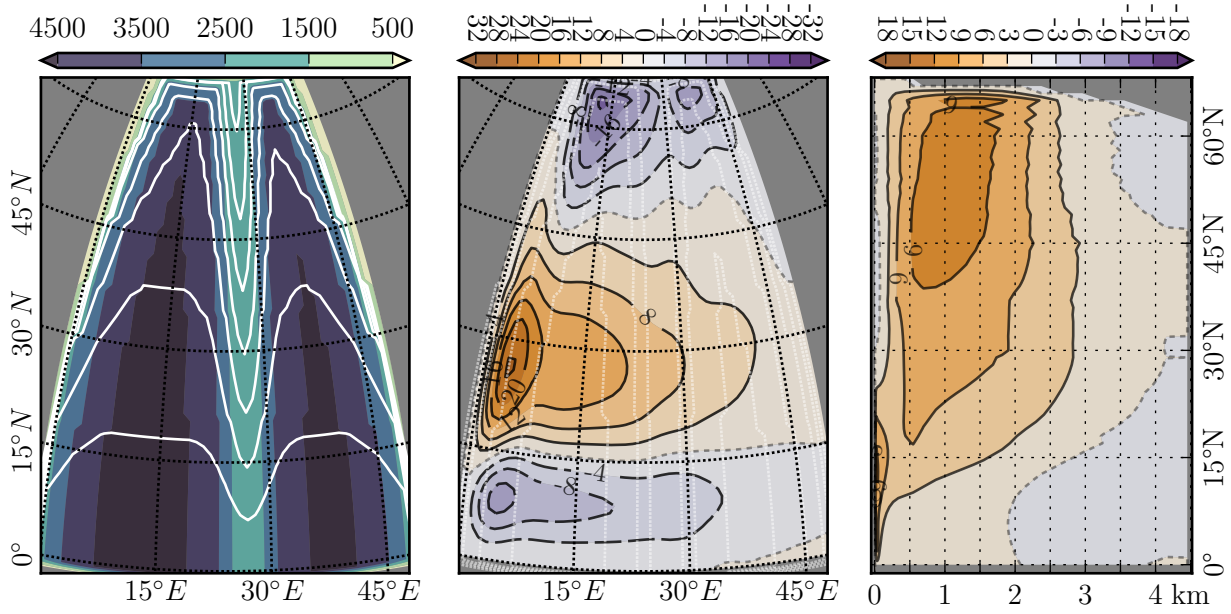

Figure 19: Experiment E1–7. Left: Bottom topography (color shading) and f/H contours (white); Middle: Horizontal streamfunction (color shading with black contours) and Bottom topography (white, dashed); Right: Meridional Overturning (color shading with black contours).

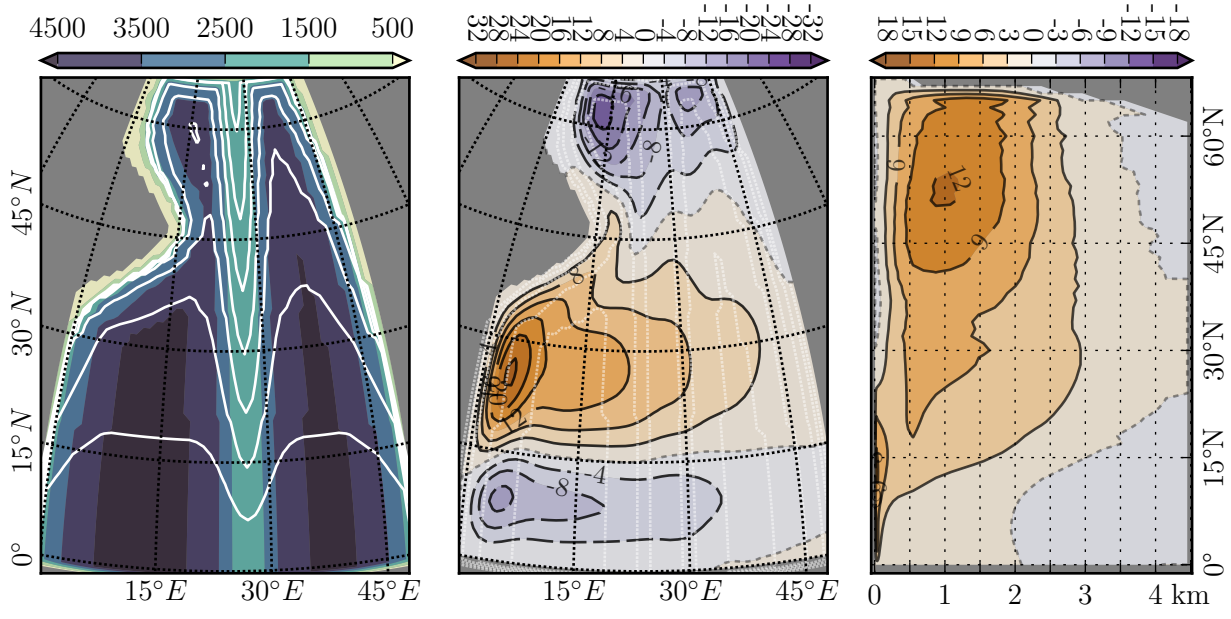

Figure 20: Experiment E1–8. Left: Bottom topography (color shading) and f/H contours (white); Middle: Horizontal streamfunction (color shading with black contours) and Bottom topography (white, dashed); Right: Meridional Overturning (color shading with black contours).

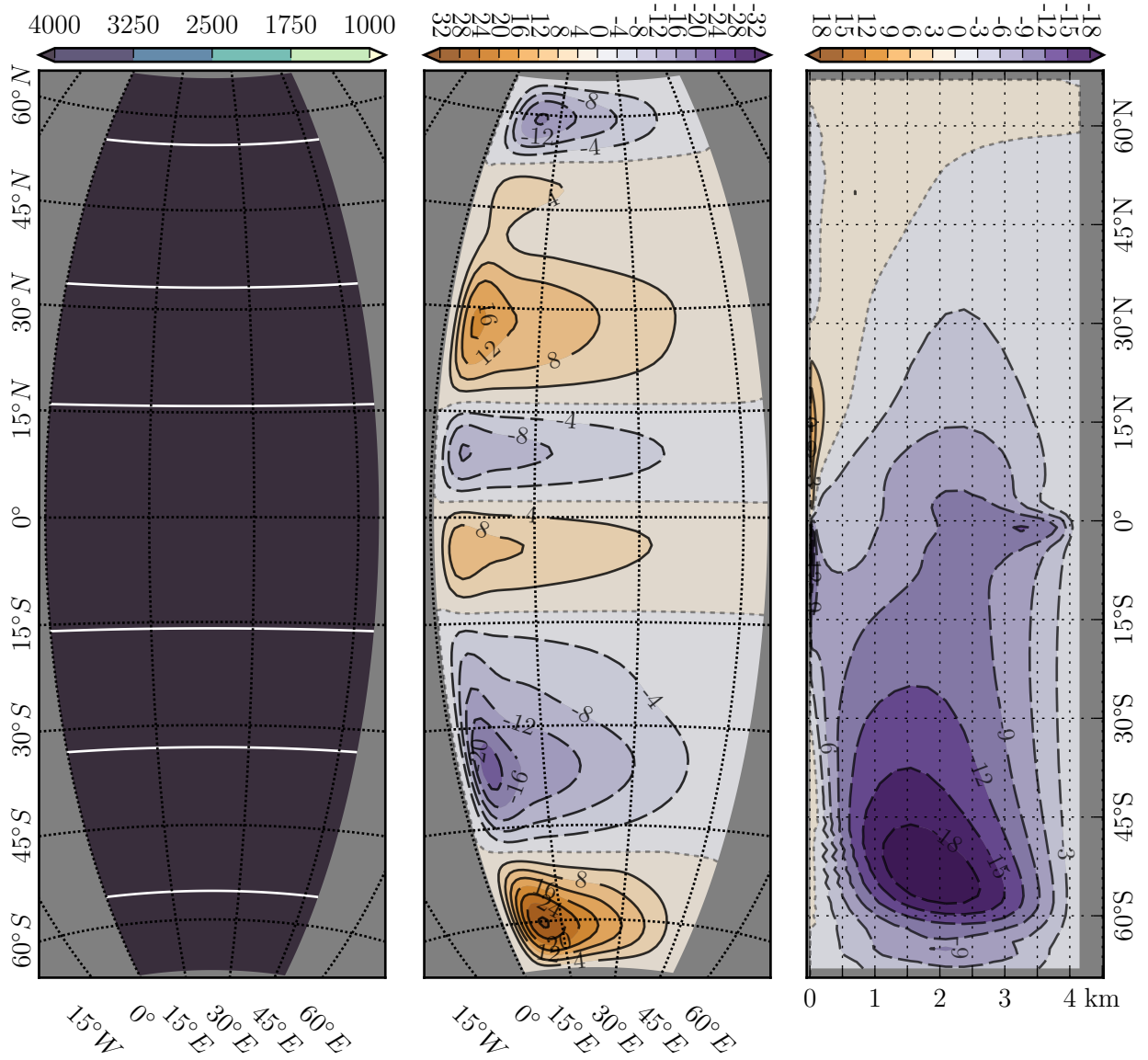

Figure 21: Experiment E2–1. Left: Bottom topography (color shading) and f/H contours (white); Middle: Horizontal streamfunction (color shading with black contours) and Bottom topography (white, dashed); Right: Meridional Overturning (color shading with black contours).

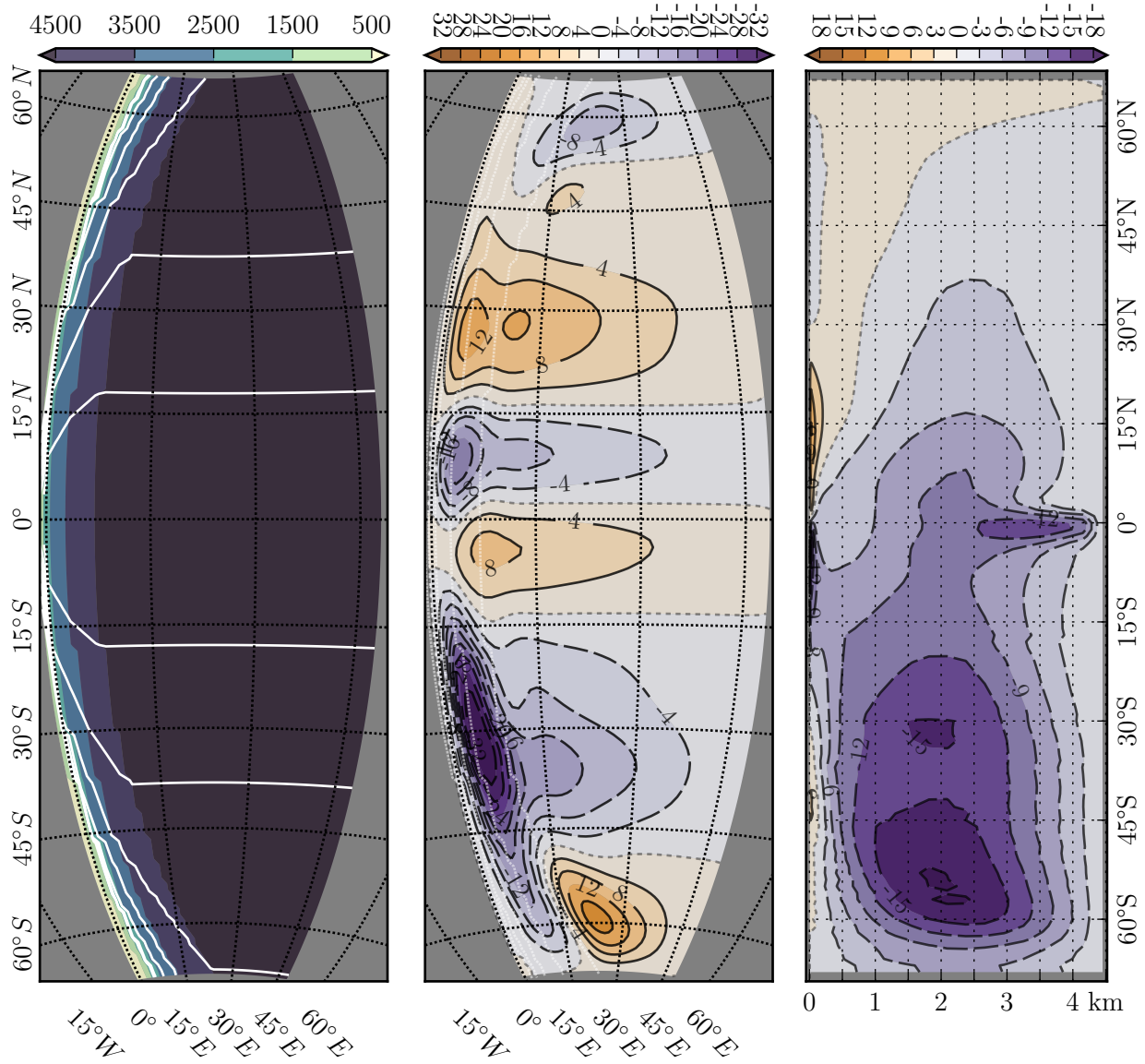

Figure 22: Experiment E2–2. Left: Bottom topography (color shading) and f/H contours (white); Middle: Horizontal streamfunction (color shading with black contours) and Bottom topography (white, dashed); Right: Meridional Overturning (color shading with black contours).

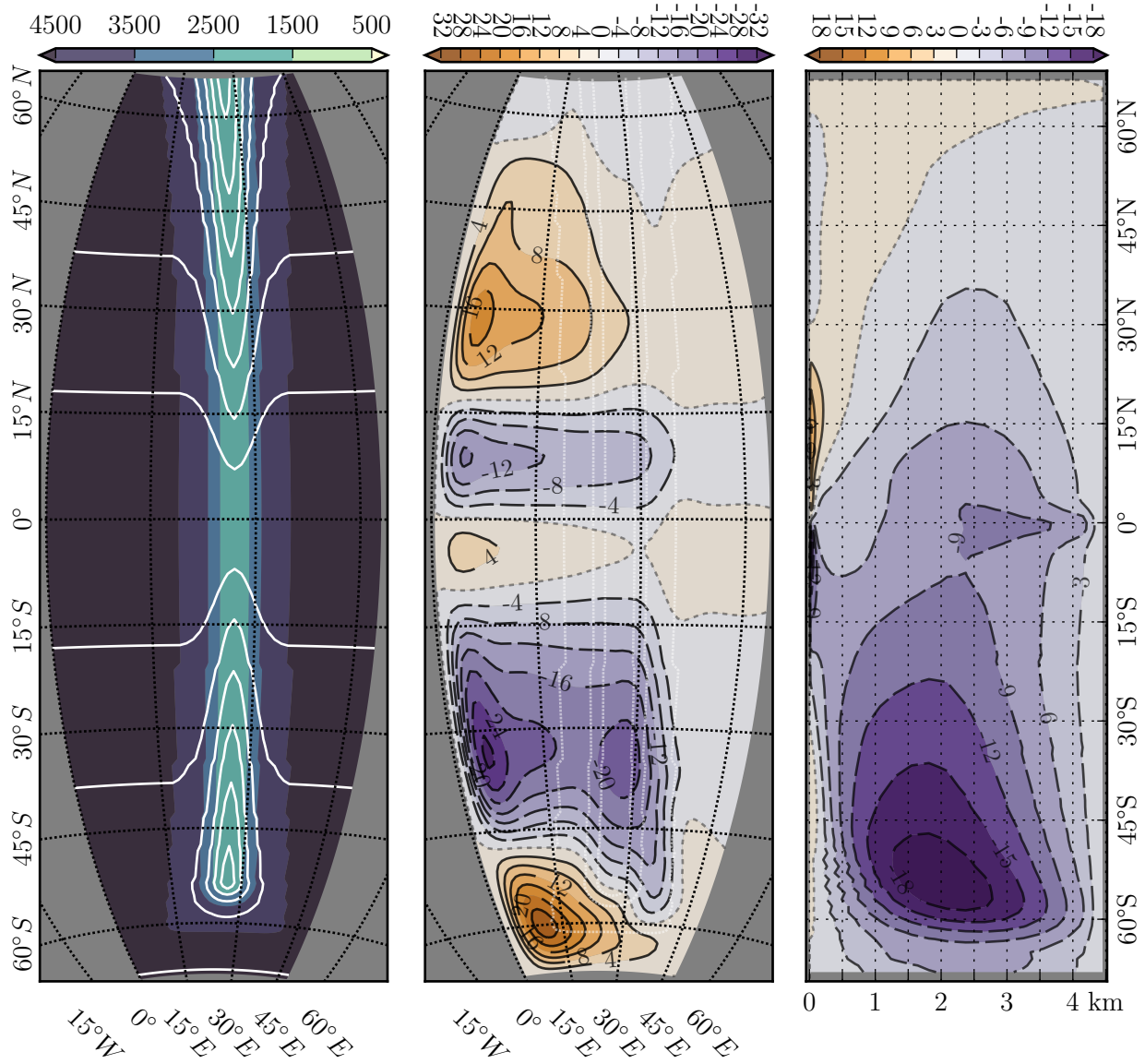

Figure 23: Experiment E2–3. Left: Bottom topography (color shading) and f/H contours (white); Middle: Horizontal streamfunction (color shading with black contours) and Bottom topography (white, dashed); Right: Meridional Overturning (color shading with black contours).

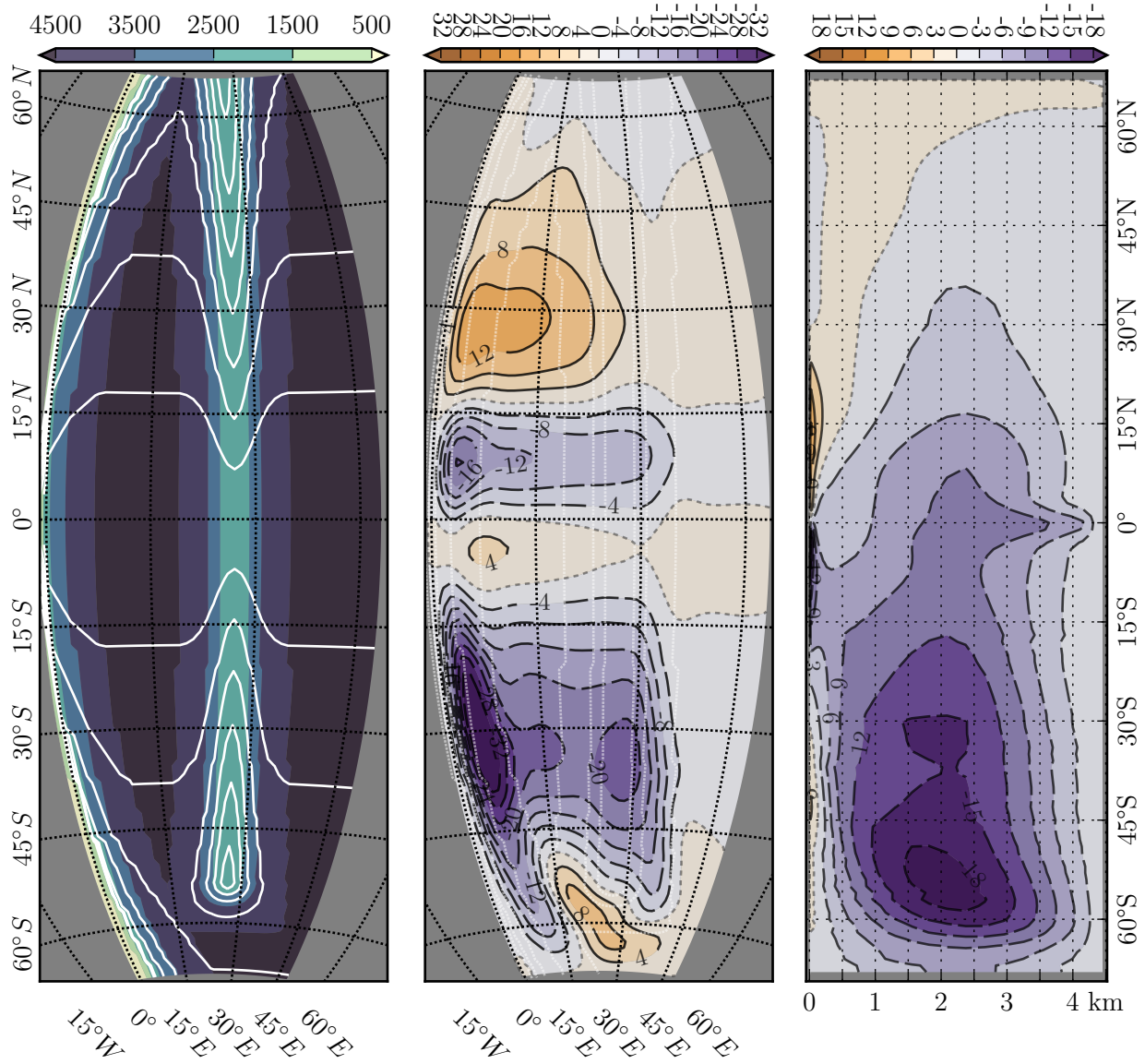

Figure 24: Experiment E2–4. Left: Bottom topography (color shading) and f/H contours (white); Middle: Horizontal streamfunction (color shading with black contours) and Bottom topography (white, dashed); Right: Meridional Overturning (color shading with black contours).

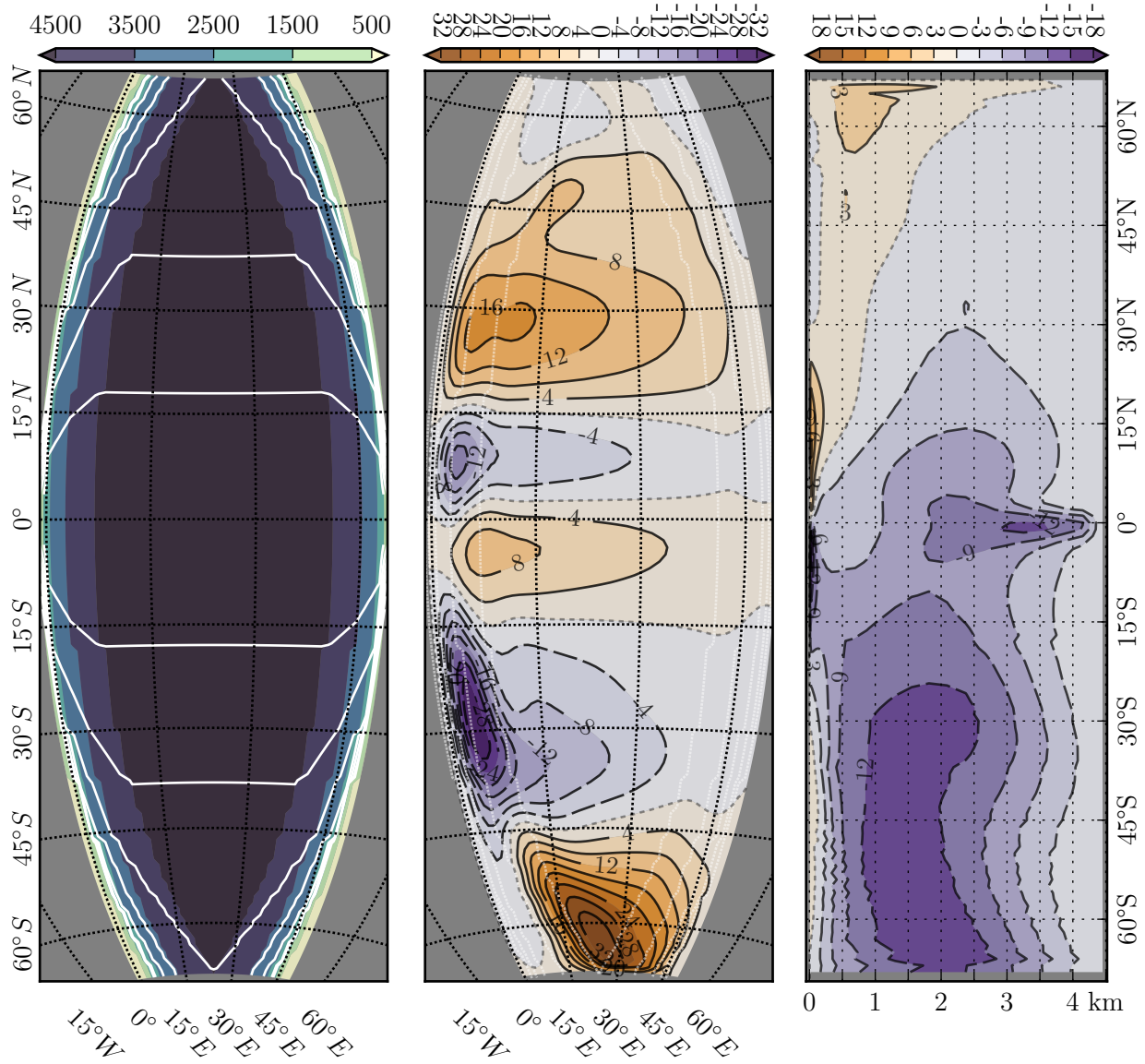

Figure 25: Experiment E2–5. Left: Bottom topography (color shading) and f/H contours (white); Middle: Horizontal streamfunction (color shading with black contours) and Bottom topography (white, dashed); Right: Meridional Overturning (color shading with black contours).

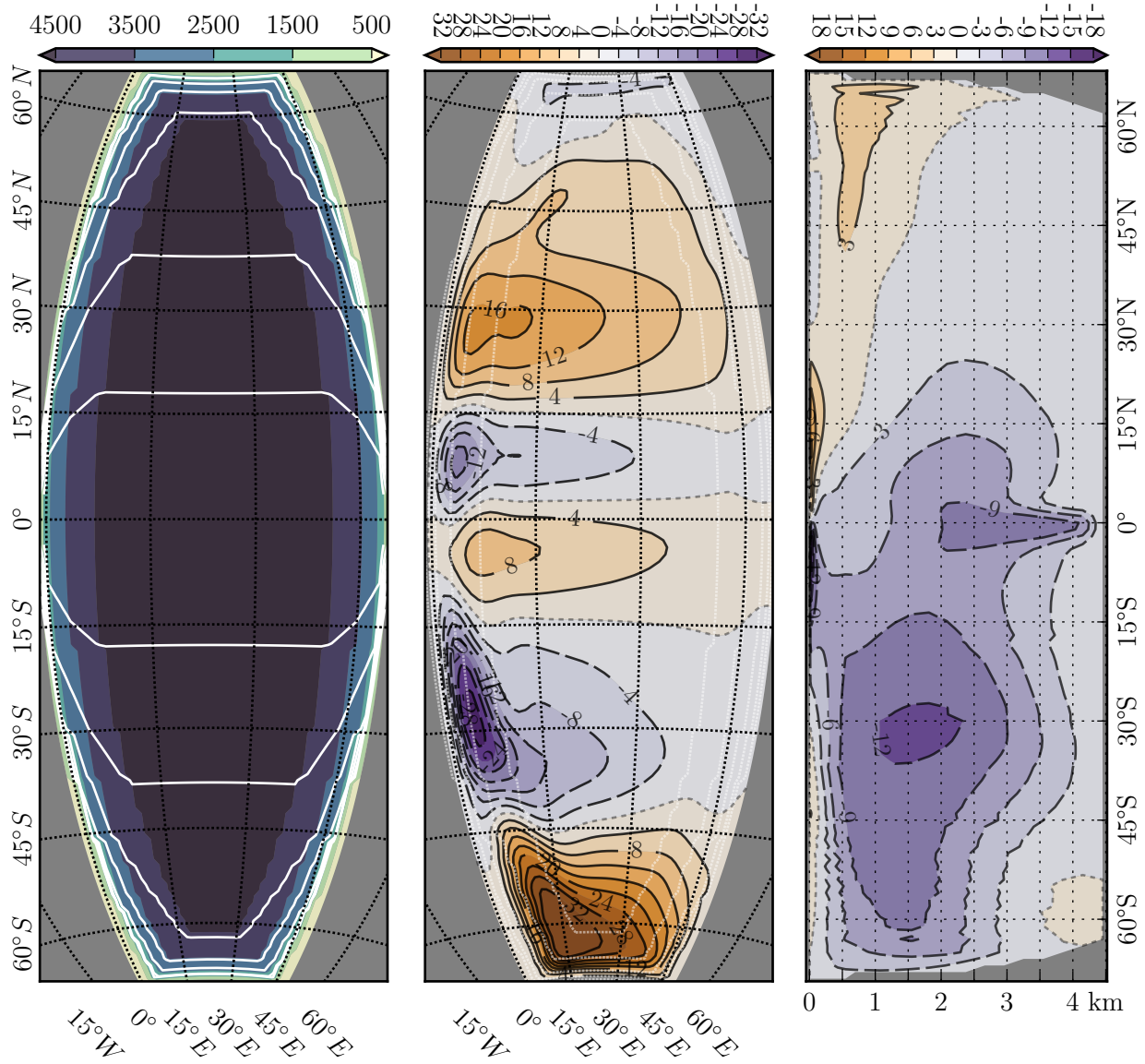

Figure 26: Experiment E2–6. Left: Bottom topography (color shading) and f/H contours (white); Middle: Horizontal streamfunction (color shading with black contours) and Bottom topography (white, dashed); Right: Meridional Overturning (color shading with black contours).

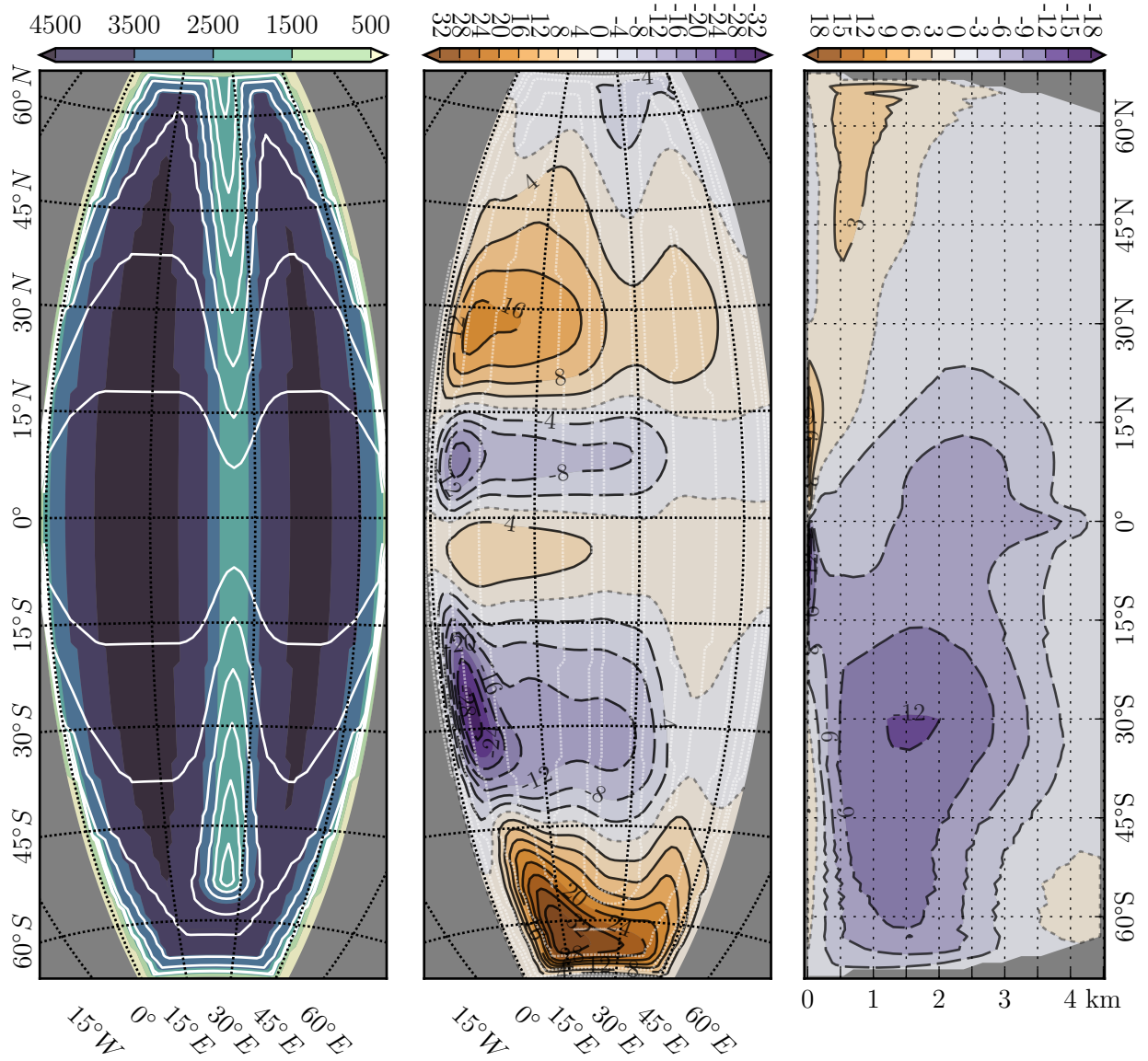

Figure 27: Experiment E2–7. Left: Bottom topography (color shading) and f/H contours (white); Middle: Horizontal streamfunction (color shading with black contours) and Bottom topography (white, dashed); Right: Meridional Overturning (color shading with black contours).

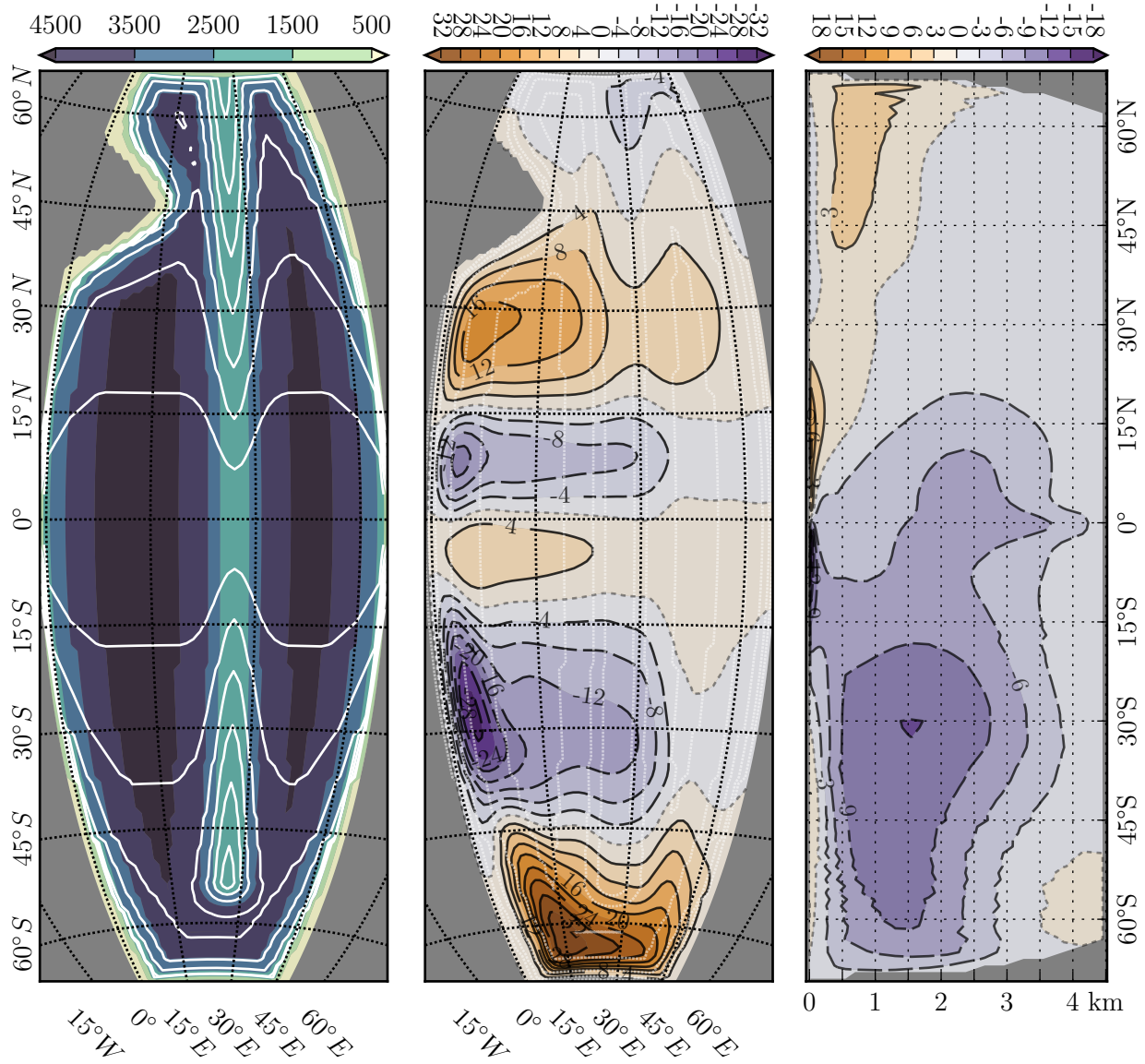

Figure 28: Experiment E2–8. Left: Bottom topography (color shading) and f/H contours (white); Middle: Horizontal streamfunction (color shading with black contours) and Bottom topography (white, dashed); Right: Meridional Overturning (color shading with black contours).

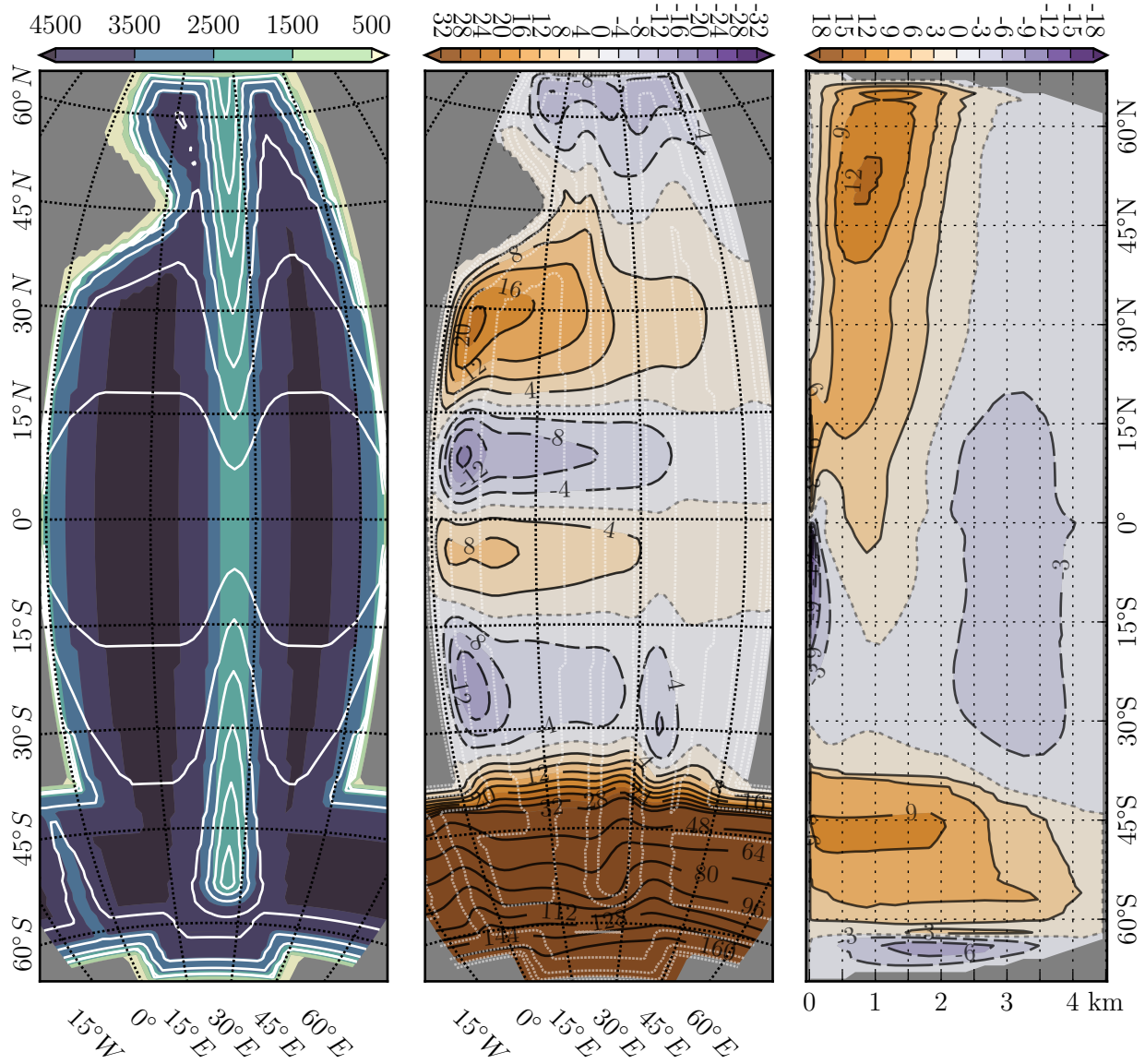

Figure 29: Experiment AC–1. Left: Bottom topography (color shading) and f/H contours (white); Middle: Horizontal streamfunction (color shading with black contours) and Bottom topography (white, dashed); Right: Meridional Overturning (color shading with black contours).

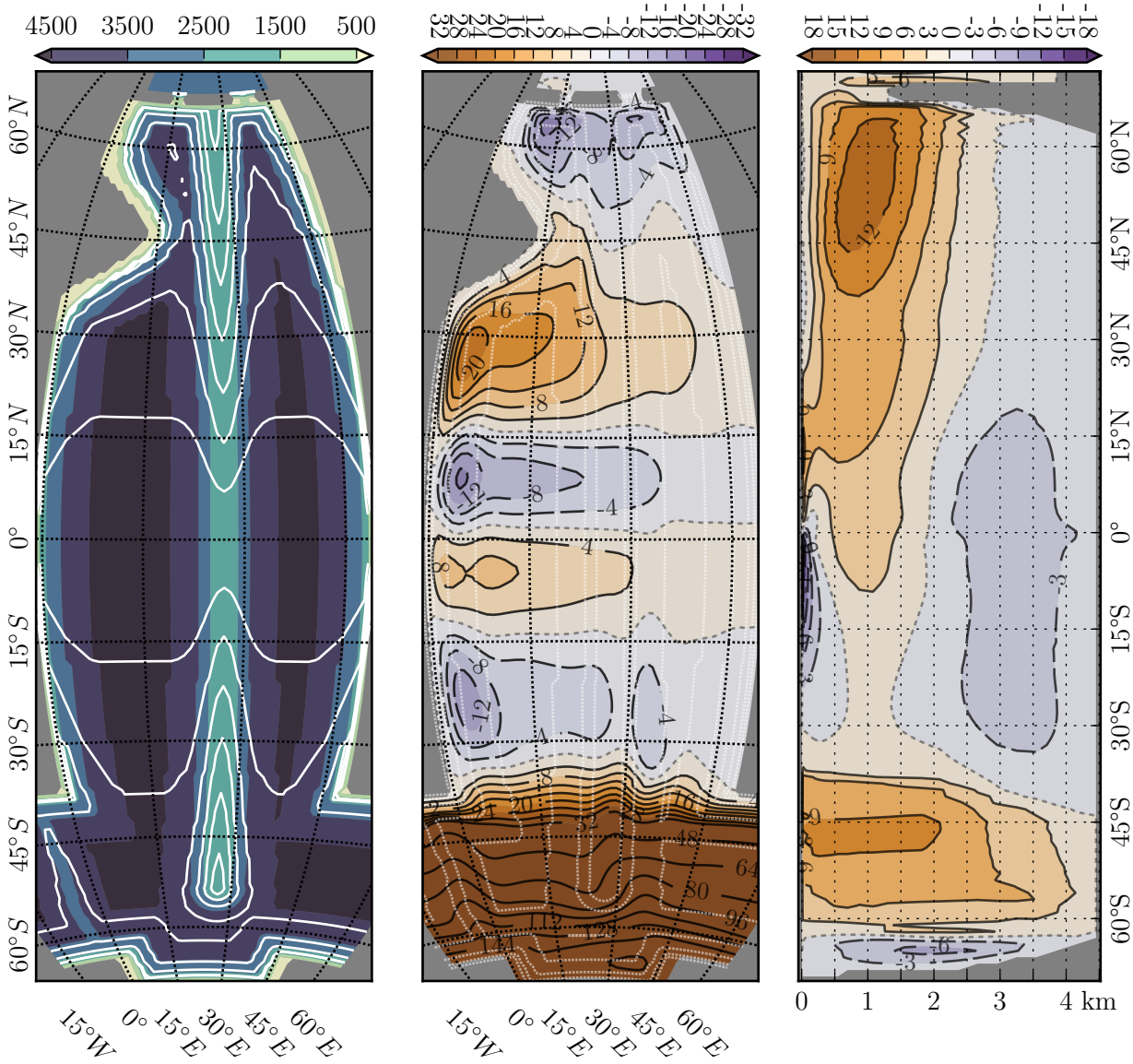

Figure 30: Experiment AC–2. Left: Bottom topography (color shading) and f/H contours (white); Middle: Horizontal streamfunction (color shading with black contours) and Bottom topography (white, dashed); Right: Meridional Overturning (color shading with black contours).

7 Summary

The influence of variable bottom topography on the large scale ocean circulation was investigated based on a series of model experiments using idealised specifications for the bottom topography. The idealised model configurations started from a single hemisphere flat-bottomed basin, evolving to a two hemisphere representation of the Atlantic Ocean with continental margins along all boundaries, a mid oceanic ridge, an Antarctic Circumpolar Current and two channels providing dense overflow waters from a Nordic Seas basin.

The investigation of the individual importance of the different bottom topography features showed that the most important bottom topography features were the western continental margin (CM-W), the northern continental margin (CM-N), the mid oceanic ridge (MOR) and the opening of an idealised Drake Passage to create an Antarctic Circumpolar Current (ACC). However, a more important finding was the way interactions between single bottom topography components lead to adjustments of the individual impact of bottom topography features. Increasing the complexity, i.e. adding multiple bottom topography features, led ultimately to a pattern not far removed from the flat-bottomed Sverdrup transport but with generally greater amplitude. The subtropical gyre transport for experiments E1–6, E1-7 and E1–8 is on average 43 % higher relative to E1–1. For the southern hemisphere of E2 the corresponding experiments show 36 % increased subtropical gyre transport. A notable exception is the northern hemisphere of E2, which is the result of a weak and shallow northern cell of the meridional overturning.

In fact, the meridional overturning proved to play a dominant role for the development of the horizontal streamfunction. A strong and deep meridional overturning would lead to very distinct patterns, e.g. the subtropical gyre of E1–2 (Fig. 14; also southern hemisphere of E2–2, Fig. 22) with greatly increased poleward western boundary transport, as known from Holland (1973); or the strong maximum over the mid oceanic ridge in E1–3 (Fig. 15; also southern hemisphere of E2–3, Fig. 23). In contrast, a weak and shallow meridional overturning which changes sign with depth, i.e. the southern hemisphere's meridional overturning extending, at depth, far into the northern hemisphere, can result in a subtropical gyre of similar strength to the flat-bottomed Sverdrup transport. In many cases, the deep meridional overturning, invading from the southern hemisphere, leads to dampening and partial shutdown of the northern subpolar gyre. The importance of the meridional overturning for the horizontal streamfunction inevitably means that the Antarctic Circumpolar Current's impact will also be noticeable, not only in its immediate proximity but also in the northern hemisphere. In fact, the incorporation of the Antarctic Circumpolar Current leads to a normalisation of the northern hemisphere, driven by the strengthening of the northern hemisphere's meridional overturning. The final change to the model domain underlines an aspect seen already in the single hemisphere experiments, i.e. increasing the complexity of the whole model domain leads to a horizontal streamfunction more and more resembling the known pattern of the real Atlantic Ocean, although each bottom topography module is highly idealised.

Overall, the presented experiments showed that the presence of variable bottom topography

will intensify the horizontal circulation, given that the meridional overturning has sufficient strength and depth. With this, we think that the the presented work clearly showed that variable bottom topography impacts the large scale ocean circulation and that the results contribute to a broadening of the understanding of the impact and interaction of different bottom topography features.

7.1 Suggestions and Outlook

In the experiments conducted in this study, some processes could not be represented or were for other reasons excluded, leading to possible improvements for future simulations. Some improvements are of a technical nature, for example better numerical representations of physical processes, e.g. the Gent and McWilliams (1990) eddy parameterisation; other changes could be done regarding the input forcing fields, e.g. addressing the failed implementation of the Labrador Sea basin and the associated deep convection, discussed in section 6.1.8 and 6.1.9. The following text is dedicated to those improvements; however we shall then go further and discuss possible steps that would lead to more realism or alternatives to isolate particular aspects of the effects of variable bottom topography.

The implementation of the Gent and McWilliams (1990) eddy parameterisation is the first aspect of model improvement that could be done, improving the representation of subgrid scale physics. Especially in high latitudes where isopycnals cross the vertical coordinates, e.g. the Antarctic Circumpolar Current region. This additional numerical improvement could be an very interesting asset to the idealised set-up presented in this thesis.

Following with another numerical aspect, as it was discussed in section 6.4, it is likely that the model exhibits grid waves in regions where the vertical velocities are high, possibly causing a spurious overturning at depth on the equator. This might be addressed by an higher vertical eddy diffusivity coefficient, or higher vertical resolution, both being easy to implement.

Moving on from numerical challenges to an unexpected drawback of the zonally uniform forcing fields. In experiment E1–8, the Labrador Sea basin module was first introduced, where it was hoped that deep convection in the Labrador Sea would increase and contribute to the meridional overturning of the northern hemisphere. However, southward surface flow combined with the zonally uniform surface restoring resulted in stable stratification in the Labrador Sea. This could be solved by either abandoning the concept of zonally uniform forcing field as a whole, or alternatively adjusting the forcing fields in selected regions to represent the conditions typical for that region, e.g. the Labrador Sea where cold dry air typically flows from the continent over the open ocean, leading to surface buoyancy loss and convection.

Before moving on to general ideas to improve the experiments, the aspect of increased horizontal resolution and the possibility to change the eddy viscosity coefficients accordingly might be explored. In Spence et al. (2012) exactly those aspects are investigated with a special interest in the North Atlantic's deep current system. It is shown that low eddy viscosities play a significant role for the near bottom currents (Spence et al., 2012); this therefore could also be important in an idealised experiment as conducted in this thesis.

While the prior changes would mostly address technical aspects of the presented thesis, there are many ways to improve or change the general setting. A possibility is the step towards time dependent forcing fields, these could be any type of dependency, some possibilities are for example using white noise in special regions to see whether those may influence the meridional overturning, other possibilities may include bi-annual, annual, inter-annual or decadal variability. All this could be accompanied by a change from restoring as the thermohaline forcing to explicit forcing, e.g. using fields of solar radiation and rainfall.

The last group of changes discussed here, are improvements of the general appearance of the lateral boundaries, i.e. the continents, adding the approximate shapes of Africa, South America, Europe and North America would interfere with the meridional symmetry common to the presented experiments. In combination with changes to the continents, could come changes to the mid oceanic ridge, also breaking with the meridional symmetry, including zonal oriented sills, as known from the southern and equatorial Atlantic, blocking the spreading of Antarctic Bottom waters towards the North Atlantic. Such changes include varying the height of the mid oceanic ridge, and including idealized fracture zones. All these features could be designed to fit into an idealised setting such as presented in this thesis.

An alternative approach, away from the idealised setting, however still with the goal to investigate the effects of variable bottom topography, could be a series of experiments where measurement based ocean bottom topography is used. Features such as for example the Mid Atlantic Ridge could be smoothed out or the continental margin along one coast could be replaced by a vertical wall. There are several papers where the flow or transports from a flat-bottomed North Atlantic Ocean model simulation were compared with simulations where the complete bottom topography is present (e.g. Greatbatch et al., 1991; Spence et al., 2012). The stepwise implementation of the measurement based bottom topography would be very interesting and a feasible project.

A Model Validation

The model validation comprises of two steps: First, coarse horizontal resolution simulations with the goal to test the model (NEMO, see Chapter 3), the prime incentive being the fast integration time. Second, simulations equivalent to those discussed in Chapter 5, i.e. with the model settings as presented in Chapter 3 but with the forcing fields reconstructed from Holland (1973, Fig. 2), with the goal to demonstrate that the solutions from Holland (1973) can be reproduced. Furthermore, the bottom topography from the second and third experiment in Holland (1973, Fig. 3; here left panel of Fig. 32) was also reconstructed.

A.1 The Coarse Horizontal Resolution Simulations

A series of coarse horizontal resolution simulations were performed Two reasons may be given: first, the horizontal resolution of these simulations is comparable to the horizontal resolution used in Holland (1973); second, the coarse horizontal resolution allows a larger timestep, drastically reducing the time needed for a model integration. Being able to perform simulations fast gives the opportunity to test model settings. In the following one option that showed anomalous results will be discussed.

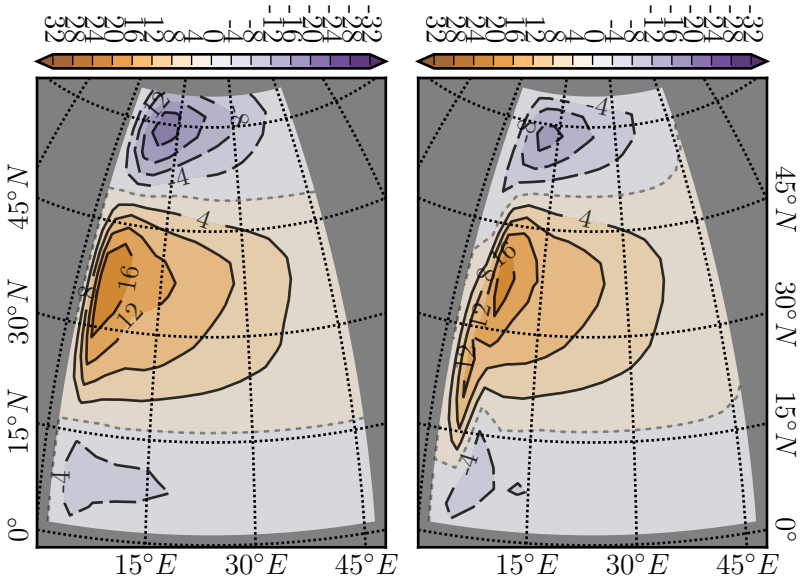

Figure 31: Reconstruction of E1 in Holland (1973), with 3 degrees horizontal resolution; shown is the horizontal streamfunction with two different advection schemes. Left: the ENE advection scheme; Right: the EEN advection scheme.

The initial simulation used the setting provided by the NEMO benchmark. The use of these settings with the coarse horizontal resolution led to artificial boundary effects on the horizontal streamfunction. The artificial boundary effects can be seen in Figure 31. The figure shows the horizontal streamfunction for a flat-bottomed ocean simulation with coarse horizontal resolution and two different advection schemes (introduced below). The left panel shows the desired pattern of the horizontal streamfunction, while the horizontal streamfunction

shown in the right panel exhibits a counter-clockwise stretch of the streamlines of the horizontal streamfunction along the boundary, most prominently seen in the south-western corner of the subtropical gyre.

The artificial boundary effect originated in the applied advection scheme; the default scheme is the energy and enstrophy conserving scheme (EEN; right panel in Figure 31). Other advection schemes, e.g. the energy conserving scheme (ENE; left panel in Figure 31) and the enstrophy conserving scheme (ENS; not shown) did not show the artificial boundary effect.

Note that this effect was found to be smaller as the horizontal resolution was increased to 1 degree (e.g. E1–1, Fig. 13), the final grid resolution. Furthermore, the EEN scheme is shown to decrease grid-scale noise close to the bottom topography and is recommended for use in NEMO (Le Sommer, Penduff, Theetten, Madec, & Barnier, 2009), and therefore the EEN advection scheme was chosen for subsequent experiments regardless of the discrepancies in the coarse resolution cases. However, the horizontal resolution in the presented experiments is still far coarser than in the studies that focus on the advection schemes (see, Penduff et al., 2007; Le Sommer et al., 2009). Note further that it was shown that the no-slip condition, which is applied in the presented experiments[8], negates the effect of the EEN scheme, at least in part (Penduff et al., 2007).

A.2 The Classical Forced Model Simulation

To demonstrate that the classical solutions presented in Holland (1973, Fig. 4) can be reproduced with the NEMO model, first the forcing fields (Holland, 1973, Fig. 2) and the bottom topography (Holland, 1973, Fig. 3) provided by Holland (1973) were reconstructed (bottom topography shown in the left panel of Figure 32). The experiments with a flat bottom closely resembled the solutions from Holland (1973) (not shown since E1–1 already is a good comparison for the flat-bottomed ocean, and despite the different forcing, the results are comparable). However, since E1–2 is considerably different to the third experiment in Holland (1973), although still qualitatively comparable, the reconstructed bottom topography (left panel of Figure 32) was used with the measurements based forcing[9] discussed in Chapter 5 to provide a better comparison. Figure 32 presents the resulting horizontal streamfunction (middle panel, Fig. 32) and in addition the homogeneous ocean response is also presented (right panel, Fig. 32), corresponding to the second experiment in Holland (1973). Again, both the the stratified and the homogeneous case are in good agreement with the classical results (Holland, 1973). This general agreement extends to the meridional overturning, for which however figures are omitted here.

Therefore, based on a series of experiments that attempted to reproduce the results of Holland (1973) as closely as possible, the conclusion is drawn that the NEMO ocean general

[8] Including the simulations associated with the model validation.

[9] The difference between the horizontal streamfunction with historic forcing (Holland, 1973, Fig. 2) and the measurement based forcing (Fig. 32) is in fact small. However noticeable when the tropical gyre transport strength is compared, which exhibits about 10 Sv for the measurement based forcing, i.e. roughly double the strength of the classical solution (Holland, 1973, Fig. 4).

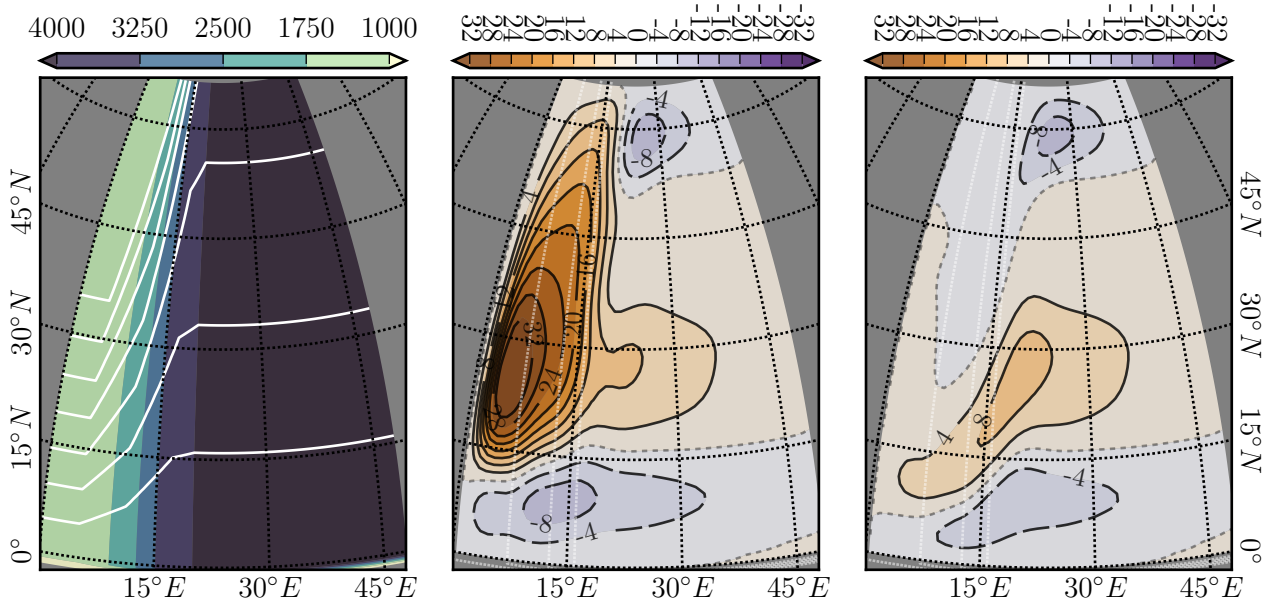

Figure 32: Reconstruction of the third experiment in Holland (1973, E3). Left: Bathymetry (colored) and f/H contours (white); Middle: Horizontal streamfunction (colored with black contours) and bathymetry (white, dashed); Right: Homogeneous ocean horizontal streamfunction (colored with black contours) and bathymetry (white, dashed).

circulation model is well suited to be used for an extended study of the effects of variable bottom topography, as presented in this thesis.

B NEMO: Settings and Namelist

In the following the FORTRAN module which contains the domain settings for NEMO (par_GYRE.h90) as well as the namelist, containing most of the options are provided. In addition the CPP keywords are listed (cpp.fcm). These technical information is provided as it stands and without further explanation. It is provided to enable the repetition of the experiments or for verification of claims about the model settings. The filed are provided for experiment AC–2, since the files are nearly identical between experiments, horizontal and meridional index and processor numbers may vary.

B.1 cpp.fcm

```
bld::tool::fppkeys key_gyre key_dynspg_flt key_zdfcst key_iom_put key_mpp_mpi key_vectopt_loop key_nosignedzero
```

B.2 par_GYRE.h90

```
   !!----------------------------------------------------------------------
    !!                  ***  par_GYRE.h90  ***
    !!    Ocean Domain : GYRE configuration at 1/jp_cfg degree resolution
    !!----------------------------------------------------------------------
    !!----------------------------------------------------------------------
    !! NEMO/OPA 3.3 , NEMO Consortium (2010)
    !! $Id: par_GYRE.h90 2715 2011-03-30 15:58:35Z rblod $
    !! Software governed by the CeCILL licence (NEMOGCM/NEMO_CeCILL.txt)
    !!----------------------------------------------------------------------
    CHARACTER (len=16)       &
#if !defined key_agrif
       , PARAMETER  &
#endif
       ::     &
```

```
      cp_cfg = "bathy_gyre"           !: name of the configuration
   INTEGER     &
#if !defined key_agrif
      , PARAMETER  &
#endif
      :: &
      jp_cfg =  1    ,         &  !: !NOT USED

      ! data size                 !!! * size of all the input files *
      jpidta  = 84,              &  !: 1st horizontal dimension ( >= jpi )
      jpjdta  = 150,             &  !: 2nd     "            "    ( >= jpj )
      jpkdta  = 31,              &  !: number of levels          ( >= jpk )

      ! global domain size        !!! * full domain *
      jpiglo  = jpidta,          &  !: 1st dimension of global domain --> i
      jpjglo  = jpjdta,          &  !: 2nd     "                  "    --> j
      ! zoom starting position
      jpizoom =   1    ,         &  !: left bottom (i,j) indices of the zoom
      jpjzoom =   1    ,         &  !: in data indices

      ! Domain characteristics
      jperio  =     1             !: lateral cond. type (between 0 and 6)

   !!  Values set to pp_not_used indicates that this parameter is not used in THIS config.
   !!  Values set to pp_to_be_computed  indicates that variables will be computed in domzgr
   REAL(wp), PARAMETER ::    &  !:
      pp_not_used       = 999999._wp  , & !: ???
      pp_to_be_computed =      0._wp      !: ???
   !!
   !! Coefficients associated with the horizontal coordinate system (jphgr_msh /= 0 )
   !!
   INTEGER,PARAMETER    ::     & !:
      jphgr_msh = 1              !: type of horizontal mesh
      !                          ! = 0 curvilinear coordinate on the sphere
      !                          !     read in coordinate.nc file
      !                          ! = 1 geographical mesh on the sphere
      !                          !     with regular grid-spacing
      !                          ! = 2 f-plane with regular grid-spacing
      !                          ! = 3 beta-plane with regular grid-spacing
      !                          ! = 4 Mercator grid with T/U point at the equator  with
      !                          !     isotropic resolution (e1_deg)
      !                          ! =5  beta-plane with regular grid-spacing and rotated domain (GYRE configuration)

      !   ppglam0 , ppgphi0: coordinates of the lower leftmost T point of the grid.
      !   The mercator grid starts only approximately at gphi0 because
      !   of the constraint that the equator be a T point.
   REAL(wp) &
#if !defined key_agrif
      , PARAMETER  &
#endif
      ::      &  !:
      ppglam0  =    -18.00_wp ,   &  !: longitude of first raw and column T-point (jphgr_msh = 1)
      ppgphi0  =    -70.50_wp ,   &  !: latitude  of first raw and column T-point (jphgr_msh = 1)
      !                           ! latitude for the Coriolis or Beta parameter (jphgr_msh = 2 or 3)
      ppe1_deg =      1.00_wp ,   &  !: zonal      grid-spacing (degrees)
      ppe2_deg =      1.00_wp ,   &  !: meridional grid-spacing (degrees)
      !
      ppe1_m   = pp_not_used,     &  !: zonal      grid-spacing (meters )
      ppe2_m   = pp_not_used         !: meridional grid-spacing (meters )
   !!
   !!  Coefficients associated with the vertical coordinate system
   !!

   REAL(wp), PARAMETER  ::        &  !:
      &      ppsur = -2033.194295283385_wp    , &  !:
      &      ppa0  =  155.8325369664153_wp    , &  !:
      &      ppa1  =  146.36159186018 90_wp   , &  !:
      !
      &      ppkth =  17.28520372419791_wp    , &  !: (non dimensional): gives the approximate
      !                                           !     layer number above which  stretching will
      !                                           !     be maximum. Usually of order jpk/2.
      &      ppacr =  5.000000000000000_wp       !: (non dimensional): stretching factor
      !                                           !     for the grid. The highest zacr, the smallest
      !                                           !     the stretching.

   !!
   !!  If all ppa0 ppa1 and ppsur are specified to 0, then
   !!  they are computed from ppdzmin, pphmax , ppkth, ppacr in dom_zgr
   !!
   REAL(wp), PARAMETER ::         &  !:
      &      ppdzmin = pp_not_used    , &  !: (meters): depth of the top (first) model layer
      !                                  !           depth of second "w" level
      &      pphmax  = pp_not_used       !: (meters): maximum depth of the ocean
      !                                  !           depth of the last "w" level
   LOGICAL,  PARAMETER ::         &
      &      ldbletanh = .FALSE.         !: Use/do not use double tanf function for vertical coordinates
   REAL(wp), PARAMETER ::         &
      &      ppa2     = pp_not_used     , &  !: Double tanh function parameters
      &      ppkth2   = pp_not_used     , &  !:
      &      ppacr2   = pp_not_used          !:

   !!----------------------------------------------------------------------
```

B.3 namelist

```
!!>>>>>>>>>>>>>>>>>>>>>>>>>>>>>>>>>>>>>>>>>>>>>>>>>>>>>>>>>>>>>>>>>>>>>>>>>>>
!! NEMO/OPA  :  1 - run manager       (namrun)
!! namelists    2 - Domain            (namzgr, namzgr_sco, namdom, namtsd)
!!              3 - Surface boundary (namsbc, namsbc_ana, namsbc_flx, namsbc_clio, namsbc_core
!!                                    namsbc_cpl, namtra_qsr, namsbc_rnf,
!!                                    namsbc_apr, namsbc_ssr, namsbc_alb)
!!              4 - lateral boundary (namlbc, namcla, namobc, namagrif, nambdy, nambdy_tide)
!!              5 - bottom  boundary (nambfr, nambbc, nambbl)
!!              6 - Tracer           (nameos, namtra_adv, namtra_ldf, namtra_dmp)
!!              7 - dynamics         (namdyn_adv, namdyn_vor, namdyn_hpg, namdyn_spg, namdyn_ldf)
!!              8 - Verical physics  (namzdf, namzdf_ric, namzdf_tke, namzdf_kpp, namzdf_ddm, namzdf_tmx)
!!              9 - diagnostics      (namnc4, namtrd, namspr, namflo, namptr, namhsb)
!!             10 - miscellaneous    (namsol, nammpp, nammpp_dyndist, namctl)
!!             11 - Obs & Assim      (namobs, nam_asminc)
!!>>>>>>>>>>>>>>>>>>>>>>>>>>>>>>>>>>>>>>>>>>>>>>>>>>>>>>>>>>>>>>>>>>>>>>>>>>>

!!======================================================================
!!                  ***  Run management namelists  ***
!!======================================================================
```

```
!!   namrun        parameters of the run
!!======================================================================
!
!-----------------------------------------------------------------------
&namrun         !   parameters of the run
!-----------------------------------------------------------------------
   nn_no       =        0   !  job number (no more used...)
   cn_exp      = "HOLLAND" !  experience name
   nn_it000    = 50544000   !  first time step
   nn_itend    = 53913600   !  last  time step
   nn_date0    =  010101    !  date at nit_0000 (format yyyymmdd) used if ln_rstart=F or (ln_rstart=T and nn_rstctl=0 or 1)
   nn_leapy    =       30   !  Leap year calendar (1) or not (0)
   ln_rstart   = .true.     !  start from rest (F) or from a restart file (T)
   nn_rstctl   =        0   !  restart control => activated only if ln_rstart = T
                            !    = 0 nn_date0 read in namelist ; nn_it000 : read in namelist
                            !    = 1 nn_date0 read in namelist ; nn_it000 : check consistancy between namelist and restart
                            !    = 2 nn_date0 read in restart  ; nn_it000 : check consistancy between namelist and restart
   cn_ocerst_in  = "HOLLAND_50544000_restart" !  suffix of ocean restart name (input)
   cn_ocerst_out = "restart"                  !  suffix of ocean restart name (output)
   nn_istate   =        1   !  output the initial state (1) or not (0)
   nn_stock    =  3369600   !  frequency of creation of a restart file (modulo referenced to 1)
   nn_write    =    17280   !  frequency of write in the output file   (modulo referenced to nn_it000)
   ln_dimgnnn  = .false.    !  DIMG file format: 1 file for all processors (F) or by processor (T)
   ln_mskland  = .false.    !  mask land points in NetCDF outputs (costly: + ~15%)
   ln_clobber  = .true.     !  clobber (overwrite) an existing file
   nn_chunksz  =        0   !  chunksize (bytes) for NetCDF file (works only with iom_nf90 routines)
/

!!======================================================================
!!                     ***  Domain namelists  ***
!!======================================================================
!!   namzgr        vertical coordinate
!!   namzgr_sco    s-coordinate or hybrid z-s-coordinate
!!   namdom        space and time domain (bathymetry, mesh, timestep)
!!   namtsd        data: temperature & salinity
!!======================================================================
!
!-----------------------------------------------------------------------
&namzgr         !   vertical coordinate
!-----------------------------------------------------------------------
   ln_zco      = .false.    !  z-coordinate - full    steps   (T/F)      ("key_zco" may also be defined)
   ln_zps      = .true.     !  z-coordinate - partial steps   (T/F)
   ln_sco      = .false.    !  s- or hybrid z-s-coordinate    (T/F)
/
!-----------------------------------------------------------------------
&namzgr_sco     !   s-coordinate or hybrid z-s-coordinate
!-----------------------------------------------------------------------
   rn_sbot_min =  300.      !  minimum depth of s-bottom surface (>0) (m)
   rn_sbot_max = 5250.      !  maximum depth of s-bottom surface (= ocean depth) (>0) (m)
   rn_theta    =    6.0     !  surface control parameter (0<=rn_theta<=20)
   rn_thetb    =    0.75    !  bottom control parameter  (0<=rn_thetb<= 1)
   rn_rmax     =    0.15    !  maximum cut-off r-value allowed (0<rn_max<1)
   ln_s_sigma  = .false.    !  hybrid s-sigma coordinates
   rn_bb       =    0.8     !  stretching with s-sigma
   rn_hc       =  150.0     !  critical depth with s-sigma
/
!-----------------------------------------------------------------------
&namdom         !   space and time domain (bathymetry, mesh, timestep)
!-----------------------------------------------------------------------
   nn_bathy    =    1       !  compute (=0) or read (=1) the bathymetry file
   nn_closea   =    0       !  remove (=0) or keep (=1) closed seas and lakes (ORCA)
   nn_msh      =    1       !  create (=1) a mesh file or not (=0)
   rn_hmin     =   -3.      !  min depth of the ocean (>0) or min number of ocean level (<0)
   rn_e3zps_min=   20.      !  partial step thickness is set larger than the minimum of
   rn_e3zps_rat=    0.1     !  rn_e3zps_min and rn_e3zps_rat*e3t, with 0<rn_e3zps_rat<1
                            !
   rn_rdt      =  600.      !  time step for the dynamics (and tracer if nn_acc=0)
   nn_baro     =   60       !  number of barotropic time step            ("key_dynspg_ts")
   rn_atfp     =    0.1     !  asselin time filter parameter
   nn_acc      =    0       !  acceleration of convergence : =1      used, rdt < rdttra(k)
                            !                                =0, not used, rdt = rdttra
   rn_rdtmin   = 7200.      !  minimum time step on tracers (used if nn_acc=1)
   rn_rdtmax   = 7200.      !  maximum time step on tracers (used if nn_acc=1)
   rn_rdth     =  800.      !  depth variation of tracer time step (used if nn_acc=1)
/
!-----------------------------------------------------------------------
&namtsd     !   data : Temperature  & Salinity
!-----------------------------------------------------------------------
!          ! file name  ! frequency (hours)   ! variable ! time interp. ! clim  !'yearly' or ! weights  ! rotation !
!          !            !  (if <0  months)   !   name   !  (logical)   ! (T/F) ! 'monthly'  ! filename ! pairing  !
   sn_tem = 'initial_ts',       -1             ,'votemper',  .false.     , .true., 'yearly'   , ' '     , ' '
   sn_sal = 'initial_ts',       -1             ,'vosaline',  .false.     , .true., 'yearly'   , ' '     , ' '
   !
   cn_dir        = './input/'  !  root directory for the location of the runoff files
   ln_tsd_init   = .true.      !  Initialisation of ocean T & S with T &S input data (T) or not (F)
   ln_tsd_tradmp = .false.     !  damping of ocean T & S toward T &S input data (T) or not (F)
/
!!======================================================================
!!            ***  Surface Boundary Condition namelists  ***
!!======================================================================
!!   namsbc          surface boundary condition
!!   namsbc_ana      analytical          formulation
!!   namsbc_flx      flux                formulation
!!   namsbc_clio     CLIO bulk formulae  formulation
!!   namsbc_core     CORE bulk formulae  formulation
!!   namsbc_mfs      MFS  bulk formulae  formulation
!!   namsbc_cpl      CouPLed             formulation                 ("key_coupled")
!!   namtra_qsr      penetrative solar radiation
!!   namsbc_rnf      river runoffs
!!   namsbc_apr      Atmospheric Pressure
!!   namsbc_ssr      sea surface restoring term (for T and/or S)
!!   namsbc_alb      albedo parameters
!!======================================================================
!
!-----------------------------------------------------------------------
&namsbc         !   Surface Boundary Condition (surface module)
!-----------------------------------------------------------------------
   nn_fsbc     = 1          !  frequency of surface boundary condition computation
                            !     (also = the frequency of sea-ice model call)
   ln_ana      = .false.    !  analytical formulation                  (T => fill namsbc_ana )
   ln_flx      = .true.     !  flux formulation                        (T => fill namsbc_flx )
   ln_blk_clio = .false.    !  CLIO bulk formulation                   (T => fill namsbc_clio)
   ln_blk_core = .false.    !  CORE bulk formulation                   (T => fill namsbc_core)
   ln_blk_mfs  = .false.    !  MFS bulk formulation                    (T => fill namsbc_mfs )
   ln_cpl      = .false.    !  Coupled formulation                     (T => fill namsbc_cpl )
   ln_apr_dyn  = .false.    !  Patm gradient added in ocean & ice Eqs. (T => fill namsbc_apr )
```

```
   nn_ice      = 0         !  =0 no ice boundary condition   ,
                           !  =1 use observed ice-cover      ,
                           !  =2 ice-model used                                  ("key_lim3" or "key_lim2")
   ln_dm2dc    = .false.   !  daily mean to diurnal cycle on short wave
   ln_rnf      = .false.   !  runoffs                                            (T => fill namsbc_rnf)
   ln_ssr      = .true.    !  Sea Surface Restoring on T and/or S                (T => fill namsbc_ssr)
   nn_fwb      = 0         !  FreshWater Budget: =0 unchecked
                           !      =1 global mean of e-p-r set to zero at each time step
                           !      =2 annual global mean of e-p-r set to zero
                           !      =3 global emp set to zero and spread out over erp area
   ln_cdgw = .false.       !  Neutral drag coefficient read from wave model (T => fill namsbc_wave)
/
!-----------------------------------------------------------------------
&namsbc_ana    !   analytical surface boundary condition
!-----------------------------------------------------------------------
   nn_tau000   =   100     !  gently increase the stress over the first ntau_rst time-steps
   rn_utau0    =   0.1e0   !  uniform value for the i-stress
   rn_vtau0    =   0.e0    !  uniform value for the j-stress
   rn_qns0     =   0.e0    !  uniform value for the total heat flux
   rn_qsr0     =   0.e0    !  uniform value for the solar radiation
   rn_emp0     =   0.e0    !  uniform value for the freswater budget (E-P)
/
!-----------------------------------------------------------------------
&namsbc_flx    !   surface boundary condition : flux formulation
!-----------------------------------------------------------------------
!              !  file name  ! frequency (hours) ! variable  ! time interp. !  clim  ! 'yearly'/ ! weights  ! rotation !
!              !             !  (if <0  months)  !   name    !   (logical)  !  (T/F) ! 'monthly' ! filename ! pairing
!
   sn_utau     = 'utau'      ,        -12         , 'utau'    , .false.      , .true. , 'yearly'  , ''       , ''
   sn_vtau     = 'zero'      ,        -12         , 'zero'    , .false.      , .true. , 'yearly'  , ''       , ''
   sn_qtot     = 'zero'      ,        -12         , 'zero'    , .false.      , .true. , 'yearly'  , ''       , ''
   sn_qsr      = 'zero'      ,        -12         , 'zero'    , .false.      , .true. , 'yearly'  , ''       , ''
   sn_emp      = 'zero'      ,        -12         , 'zero'    , .false.      , .true. , 'yearly'  , ''       , ''

   cn_dir      = './input/'      !  root directory for the location of the flux files
/
!-----------------------------------------------------------------------
&namsbc_clio   !   namsbc_clio  CLIO bulk formulae
!-----------------------------------------------------------------------
!              !  file name  ! frequency (hours) ! variable  ! time interp. !  clim  ! 'yearly'/ ! weights  ! rotation !
!              !             !  (if <0  months)  !   name    !   (logical)  !  (T/F) ! 'monthly' ! filename ! pairing
!
   sn_utau     = 'taux_1m'   ,        -1          , 'sozotaux', .true.       , .true. , 'yearly'  , ''       , ''
   sn_vtau     = 'tauy_1m'   ,        -1          , 'sometauy', .true.       , .true. , 'yearly'  , ''       , ''
   sn_wndm     = 'flx'       ,        -1          , 'socliowi', .true.       , .true. , 'yearly'  , ''       , ''
   sn_tair     = 'flx'       ,        -1          , 'socliot2', .true.       , .true. , 'yearly'  , ''       , ''
   sn_humi     = 'flx'       ,        -1          , 'socliohu', .true.       , .true. , 'yearly'  , ''       , ''
   sn_ccov     = 'flx'       ,        -1          , 'socliocl', .false.      , .true. , 'yearly'  , ''       , ''
   sn_prec     = 'flx'       ,        -1          , 'socliopl', .false.      , .true. , 'yearly'  , ''       , ''

   cn_dir      = './'      !  root directory for the location of the bulk files are
/
!-----------------------------------------------------------------------
&namsbc_core   !   namsbc_core  CORE bulk formulae
!-----------------------------------------------------------------------
!              !  file name  ! frequency (hours) ! variable  ! time interp. !  clim  ! 'yearly'/ ! weights  ! rotation !
!              !             !  (if <0  months)  !   name    !   (logical)  !  (T/F) ! 'monthly' ! filename ! pairing
!
   sn_wndi = 'u_10.15JUNE2009_orca2'       ,  6  , 'U_10_MOD',  .false.     , .true. , 'yearly'  , ''       , 'Uwnd'
   sn_wndj = 'v_10.15JUNE2009_orca2'       ,  6  , 'V_10_MOD',  .false.     , .true. , 'yearly'  , ''       , 'Vwnd'
   sn_qsr  = 'ncar_rad.15JUNE2009_orca2'   , 24  , 'SWDN_MOD',  .false.     , .true. , 'yearly'  , ''       , ''
   sn_qlw  = 'ncar_rad.15JUNE2009_orca2'   , 24  , 'LWDN_MOD',  .false.     , .true. , 'yearly'  , ''       , ''
   sn_tair = 't_10.15JUNE2009_orca2'       ,  6  , 'T_10_MOD',  .false.     , .true. , 'yearly'  , ''       , ''
   sn_humi = 'q_10.15JUNE2009_orca2'       ,  6  , 'Q_10_MOD',  .false.     , .true. , 'yearly'  , ''       , ''
   sn_prec = 'ncar_precip.15JUNE2009_orca2', -1  , 'PRC_MOD1',  .false.     , .true. , 'yearly'  , ''       , ''
   sn_snow = 'ncar_precip.15JUNE2009_orca2', -1  , 'SNOW'    ,  .false.     , .true. , 'yearly'  , ''       , ''
   sn_tdif = 'taudif_core'                 , 24  , 'taudif'  ,  .false.     , .true. , 'yearly'  , ''       , ''

   cn_dir      = './'      !  root directory for the location of the bulk files
   ln_2m       = .false.   !  air temperature and humidity referenced at 2m (T) instead 10m (F)
   ln_taudif   = .false.   !  HF tau contribution: use "mean of stress module - module of the mean stress" data
   rn_pfac     = 1.        !  multiplicative factor for precipitation (total & snow)
/
!-----------------------------------------------------------------------
&namsbc_mfs    !   namsbc_mfs  MFS bulk formulae
!-----------------------------------------------------------------------
!              !  file name  ! frequency (hours) ! variable  ! time interp. !  clim  ! 'yearly'/ ! weights  ! rotation !
!              !             !  (if <0  months)  !   name    !   (logical)  !  (T/F) ! 'monthly' ! filename ! pairing
!
   sn_wndi     =   'ecmwf'   ,         6          , 'u10'     ,    .true.     , .false. , 'daily'  ,'bicubic.nc' , ''
   sn_wndj     =   'ecmwf'   ,         6          , 'v10'     ,    .true.     , .false. , 'daily'  ,'bicubic.nc' , ''
   sn_clc      =   'ecmwf'   ,         6          , 'clc'     ,    .true.     , .false. , 'daily'  ,'bilinear.nc', ''
   sn_msl      =   'ecmwf'   ,         6          , 'msl'     ,    .true.     , .false. , 'daily'  ,'bicubic.nc' , ''
   sn_tair     =   'ecmwf'   ,         6          , 't2'      ,    .true.     , .false. , 'daily'  ,'bicubic.nc' , ''
   sn_rhm      =   'ecmwf'   ,         6          , 'rh'      ,    .true.     , .false. , 'daily'  ,'bilinear.nc', ''
   sn_prec     =   'ecmwf'   ,         6          , 'precip'  ,    .true.     , .true.  , 'daily'  ,'bicubic.nc' , ''

   cn_dir      = './ECMWF/'      !  root directory for the location of the bulk files
/
!-----------------------------------------------------------------------
&namsbc_cpl    !   coupled ocean/atmosphere model                        ("key_coupled")
!-----------------------------------------------------------------------
!                    !     description        !  multiple  !    vector   !      vector          ! vector !
!                    !                        ! categories !  reference  !    orientation       ! grids  !
! send
sn_snd_temp   =       'weighted oce and ice' ,    'no'    ,     ''       ,         ''            ,   ''
sn_snd_alb    =       'weighted ice'         ,    'no'    ,     ''       ,         ''            ,   ''
sn_snd_thick  =       'none'                 ,    'no'    ,     ''       ,         ''            ,   ''
sn_snd_crt    =       'none'                 ,    'no'    , 'spherical' , 'eastward-northward' ,  'T'
sn_snd_co2    =       'coupled'              ,    'no'    ,     ''       ,         ''            ,   ''
! receive
sn_rcv_w10m   =       'none'                 ,    'no'    ,     ''       ,         ''            ,   ''
sn_rcv_taumod =       'coupled'              ,    'no'    ,     ''       ,         ''            ,   ''
sn_rcv_tau    =       'oce only'             ,    'no'    , 'cartesian' , 'eastward-northward' ,  'U,V'
sn_rcv_dqnsdt =       'coupled'              ,    'no'    ,     ''       ,         ''            ,   ''
sn_rcv_qsr    =       'oce and ice'          ,    'no'    ,     ''       ,         ''            ,   ''
sn_rcv_qns    =       'oce and ice'          ,    'no'    ,     ''       ,         ''            ,   ''
sn_rcv_emp    =       'conservative'         ,    'no'    ,     ''       ,         ''            ,   ''
sn_rcv_rnf    =       'coupled'              ,    'no'    ,     ''       ,         ''            ,   ''
sn_rcv_cal    =       'coupled'              ,    'no'    ,     ''       ,         ''            ,   ''
sn_rcv_co2    =       'coupled'              ,    'no'    ,     ''       ,         ''            ,   ''
/
!-----------------------------------------------------------------------
&namtra_qsr    !   penetrative solar radiation
!-----------------------------------------------------------------------
!              !  file name  ! frequency (hours) ! variable  ! time interp. !  clim  ! 'yearly'/ ! weights  ! rotation !
```

```
!              !             !  (if <0  months)  !   name    !   (logical)  !  (T/F) ! 'monthly' ! filename ! pairing
!
   sn_chl      ='chlorophyll',        -1         , 'CHLA'    ,   .true.     , .true. , 'yearly'  , ''       , ''

   cn_dir      = './'      !  root directory for the location of the runoff files
   ln_traqsr   = .true.    !  Light penetration (T) or not (F)
   ln_qsr_rgb  = .false.   !  RGB (Red-Green-Blue) light penetration
   ln_qsr_2bd  = .true.    !  2 bands                light penetration
   ln_qsr_bio  = .false.   !  bio-model light penetration
   nn_chldta   =      0    !  RGB : Chl data (=1) or cst value (=0)
   rn_abs      =   0.58    !  RGB & 2 bands: fraction of light (rn_si1)
   rn_si0      =   0.35    !  RGB & 2 bands: shortess depth of extinction
   rn_si1      =   23.0    !  2 bands: longest depth of extinction
/
!-----------------------------------------------------------------------
&namsbc_rnf    !   runoffs namelist surface boundary condition
!-----------------------------------------------------------------------
!              !  file name  ! frequency (hours) ! variable  ! time interp. !  clim   ! 'yearly'/ ! weights  ! rotation !
!              !             !  (if <0  months)  !   name    !   (logical)  !  (T/F) ! 'monthly' ! filename ! pairing
!
   sn_rnf      = 'runoff_core_monthly',     -1    , 'sorunoff',    .true.     , .true. , 'yearly'  , ''       , ''
   sn_cnf      = 'runoff_core_monthly',      0    , 'socoefr0',    .false.    , .true. , 'yearly'  , ''       , ''
   sn_s_rnf    = 'runoffs'            ,     24    , 'rosaline',    .true.     , .true. , 'yearly'  , ''       , ''
   sn_t_rnf    = 'runoffs'            ,     24    , 'rotemper',    .true.     , .true. , 'yearly'  , ''       , ''
   sn_dep_rnf  = 'runoffs'            ,      0    , 'rodepth' ,    .false.    , .true. , 'yearly'  , ''       , ''

   cn_dir        = './'      !  root directory for the location of the runoff files
   ln_rnf_emp    = .false.   !  runoffs included into precipitation field (T) or into a file (F)
   ln_rnf_mouth  = .false.   !  specific treatment at rivers mouths
   rn_hrnf       =  15.e0    !  depth over which enhanced vertical mixing is used
   rn_avt_rnf    =   1.e-3   !  value of the additional vertical mixing coef. [m2/s]
   rn_rfact      =   1.e0    !  multiplicative factor for runoff
   ln_rnf_depth  = .false.   !  read in depth information for runoff
   ln_rnf_tem    = .false.   !  read in temperature information for runoff
   ln_rnf_sal    = .false.   !  read in salinity information for runoff
/
!-----------------------------------------------------------------------
&namsbc_apr    !   Atmospheric pressure used as ocean forcing or in bulk
!-----------------------------------------------------------------------
!              ! file name ! frequency (hours) ! variable ! time interpol. !  clim   ! 'yearly'/ ! weights  ! rotation !
!              !           !  (if <0  months)  !   name   !    (logical)   !  (T/F)  ! 'monthly' ! filename ! pairing
!
   sn_apr      = 'patm'    ,         -1        ,'somslpre',    .true.      , .true.  , 'yearly'  ,  ''      ,    ''

   cn_dir      = './'      !  root directory for the location of the bulk files
   rn_pref     = 101000._wp !  reference atmospheric pressure   [N/m2]/
   ln_ref_apr  = .false.   !  ref. pressure: global mean Patm (T) or a constant (F)
   ln_apr_obc  = .false.   !  inverse barometer added to OBC ssh data
/
!-----------------------------------------------------------------------
&namsbc_ssr    !   surface boundary condition : sea surface restoring
!-----------------------------------------------------------------------
!              !  file name  ! frequency (hours) ! variable  ! time interp. !  clim   ! 'yearly'/ ! weights  ! rotation !
!              !             !  (if <0  months)  !   name    !   (logical)  !  (T/F)  ! 'monthly' ! filename ! pairing
!
   sn_sst      = 'ssr'       ,       -12         , 'sst'     ,    .false.    , .true. , 'yearly'  , ''       , ''
   sn_sss      = 'ssr'       ,       -12         , 'sss'     ,    .false.    , .true. , 'yearly'  , ''       , ''

   cn_dir      = './input/'  !  root directory for the location of the runoff files
   nn_sstr     =     1       !  add a retroaction term in the surface heat       flux (=1) or not (=0)
   nn_sssr     =     1       !  add a damping     term in the surface freshwater flux (=2)
                             !  or to SSS only (=1) or no damping term (=0)
   rn_dqdt     =   -80.      !  magnitude of the retroaction on temperature   [W/m2/K]
   rn_deds     =  -333.33    !  magnitude of the damping on salinity   [mm/day]
   ln_sssr_bnd =   .false.   !  flag to bound erp term (associated with nn_sssr=2)
   rn_sssr_bnd =   4.e0      !  ABS(Max/Min) value of the damping erp term [mm/day]
/
!-----------------------------------------------------------------------
&namsbc_alb    !   albedo parameters
!-----------------------------------------------------------------------
   rn_cloud    =    0.06    !  cloud correction to snow and ice albedo
   rn_albice   =    0.53    !  albedo of melting ice in the arctic and antarctic
   rn_alphd    =    0.80    !  coefficients for linear interpolation used to
   rn_alphc    =    0.65    !  compute albedo between two extremes values
   rn_alphdi   =    0.72    !  (Pyane, 1972)
/

!!======================================================================
!!               ***  Lateral boundary condition  ***
!!======================================================================
!!   namlbc        lateral momentum boundary condition
!!   namcla        cross land advection
!!   namobc        open boundaries parameters                          ("key_obc")
!!   namagrif      agrif nested grid ( read by child model only )      ("key_agrif")
!!   nambdy        Unstructured open boundaries                        ("key_bdy")
!!   namtide       Tidal forcing at open boundaries                    ("key_bdy_tides")
!!======================================================================
!
!-----------------------------------------------------------------------
&namlbc        !   lateral momentum boundary condition
!-----------------------------------------------------------------------
   rn_shlat    =    2.      !  shlat = 0  !  0 < shlat < 2  !  shlat = 2  !  2 < shlat
                            !  free slip  !   partial slip  !   no slip   ! strong slip
   ln_vorlat   = .false.    !  consistency of vorticity boundary condition with analytical eqs.
/
!-----------------------------------------------------------------------
&namcla        !   cross land advection
!-----------------------------------------------------------------------
   nn_cla      =    0       !  advection between 2 ocean pts separates by land
/
!-----------------------------------------------------------------------
&namobc        !   open boundaries parameters                          ("key_obc")
!-----------------------------------------------------------------------
   ln_obc_clim = .false.    !  climatological obc data files (T) or not (F)
   ln_vol_cst  = .true.     !  impose the total volume conservation (T) or not (F)
   ln_obc_fla  = .false.    !  Flather open boundary condition
   nn_obcdta   =    1       !  = 0 the obc data are equal to the initial state
                            !  = 1 the obc data are read in 'obc.dta' files
   cn_obcdta   = 'annual'   !  set to annual if obc datafile hold 1 year of data
                            !  set to monthly if obc datafile hold 1 month of data
   rn_dpein    =    1.      !  damping time scale for inflow at east  open boundary
   rn_dpwin    =    1.      !     -          -         -        west    -       -
   rn_dpnin    =    1.      !     -          -         -        north   -       -
   rn_dpsin    =    1.      !     -          -         -        south   -       -
   rn_dpeob    = 3000.      !  time relaxation (days) for the east  open boundary
   rn_dpwob    =   15.      !     -          -         -      west    -       -
```

```
   rn_dpnob    = 3000.     !     -           -         -     north   -      -
   rn_dpsob    =   15.     !     -           -         -     south   -      -
   rn_volemp   =    1.     !  = 0 the total volume change with the surface flux (E-P-R)
                           !  = 1 the total volume remains constant
/
!-----------------------------------------------------------------------
&namagrif      !  AGRIF zoom                                            ("key_agrif")
!-----------------------------------------------------------------------
   nn_cln_update =    3    !  baroclinic update frequency
   ln_spc_dyn    = .true.  !  use 0 as special value for dynamics
   rn_sponge_tra = 2880.   !  coefficient for tracer   sponge layer [m2/s]
   rn_sponge_dyn = 2880.   !  coefficient for dynamics sponge layer [m2/s]
/
!-----------------------------------------------------------------------
!       nam_tide        tide parameters (#ifdef key_tide)
!-----------------------------------------------------------------------
!  ln_tide_pot    = use tidal potential forcing
!  nb_harmo     = number of constituents used
!  name(1)      = 'M2', 'K1', etc name of constituent

&nam_tide
   ln_tide_pot           = .true.
   nb_harmo    = 11
   clname(1)     =   'M2'
   clname(2)     =   'S2'
   clname(3)     =   'N2'
   clname(4)     =   'K1'
   clname(5)     =   'O1'
   clname(6)     =   'Q1'
   clname(7)     =   'M4'
   clname(8)     =   'K2'
   clname(9)     =   'P1'
   clname(10)    =   'Mf'
   clname(11)    =   'Mm'
/
!-----------------------------------------------------------------------
&nambdy        !  unstructured open boundaries                          ("key_bdy")
!-----------------------------------------------------------------------
    nb_bdy = 1                          !  number of open boundary sets
    ln_coords_file = .true.             !  =T : read bdy coordinates from file
    cn_coords_file = 'coordinates.bdy.nc' !  bdy coordinates files
    ln_mask_file = .false.              !  =T : read mask from file
    cn_mask_file = ''                   !  name of mask file (if ln_mask_file=.TRUE.)
    nn_dyn2d      =  2                  !  boundary conditions for barotropic fields
    nn_dyn2d_dta  =  3                  !  = 0, bdy data are equal to the initial state
                                        !  = 1, bdy data are read in 'bdydata   .nc' files
                                        !  = 2, use tidal harmonic forcing data from files
                                        !  = 3, use external data AND tidal harmonic forcing
    nn_dyn3d      =  0                  !  boundary conditions for baroclinic velocities
    nn_dyn3d_dta  =  0                  !  = 0, bdy data are equal to the initial state
                           !  = 1, bdy data are read in 'bdydata   .nc' files
    nn_tra        =  1                  !  boundary conditions for T and S
    nn_tra_dta    =  1                  !  = 0, bdy data are equal to the initial state
                           !  = 1, bdy data are read in 'bdydata   .nc' files
    nn_rimwidth  = 10                    !  width of the relaxation zone
    ln_vol     = .false.                !  total volume correction (see nn_volctl parameter)
    nn_volctl  = 1                      !  = 0, the total water flux across open boundaries is zero
/
!-----------------------------------------------------------------------
&nambdy_dta       !  open boundaries - external data           ("key_bdy")
!-----------------------------------------------------------------------
!              !    file name    ! frequency (hours) !  variable  ! time interpol. !  clim   ! 'yearly'/ ! weights  ! rotation !
!              !                 !  (if <0  months)  !    name    !    (logical)   !  (T/F)  ! 'monthly' ! filename ! pairing
!
   bn_ssh =      'amm12_bdyT_u2d' ,          24         , 'sossheig' ,     .true.     , .false. ,  'daily'  ,     ''     ,
''
   bn_u2d =      'amm12_bdyU_u2d' ,          24         , 'vobtcrtx' ,     .true.     , .false. ,  'daily'  ,     ''     ,
''
   bn_v2d =      'amm12_bdyV_u2d' ,          24         , 'vobtcrty' ,     .true.     , .false. ,  'daily'  ,     ''     ,
''
   bn_u3d  =     'amm12_bdyU_u3d' ,          24         , 'vozocrtx' ,     .true.     , .false. ,  'daily'  ,     ''     ,
''
   bn_v3d  =     'amm12_bdyV_u3d' ,          24         , 'vomecrty' ,     .true.     , .false. ,  'daily'  ,     ''     ,
''
   bn_tem  =     'amm12_bdyT_tra' ,          24         , 'votemper' ,     .true.     , .false. ,  'daily'  ,     ''     ,
''
   bn_sal  =     'amm12_bdyT_tra' ,          24         , 'vosaline' ,     .true.     , .false. ,  'daily'  ,     ''     ,
''
   cn_dir  =     'bdydta/'
   ln_full_vel = .false.
/
!-----------------------------------------------------------------------
&nambdy_tide     ! tidal forcing at open boundaries
!-----------------------------------------------------------------------
   filtide      = 'bdydta/amm12_bdytide_'          !  file name root of tidal forcing files
    tide_cpt(1)    ='Q1'  !  names of tidal components used
    tide_cpt(2)    ='O1'  !  names of tidal components used
    tide_cpt(3)    ='P1'  !  names of tidal components used
    tide_cpt(4)    ='S1'  !  names of tidal components used
    tide_cpt(5)    ='K1'  !  names of tidal components used
    tide_cpt(6)    ='2N2' !  names of tidal components used
    tide_cpt(7)    ='MU2' !  names of tidal components used
    tide_cpt(8)    ='N2'  !  names of tidal components used
    tide_cpt(9)    ='NU2' !  names of tidal components used
    tide_cpt(10)    ='M2'  !  names of tidal components used
    tide_cpt(11)    ='L2'  !  names of tidal components used
    tide_cpt(12)    ='T2'  !  names of tidal components used
    tide_cpt(13)    ='S2'  !  names of tidal components used
    tide_cpt(14)    ='K2'  !  names of tidal components used
    tide_cpt(15)    ='M4'  !  names of tidal components used
    tide_speed(1)    = 13.398661 !  phase speeds of tidal components (deg/hour)
    tide_speed(2)    = 13.943036 !  phase speeds of tidal components (deg/hour)
    tide_speed(3)    = 14.958932 !  phase speeds of tidal components (deg/hour)
    tide_speed(4)    = 15.000001 !  phase speeds of tidal components (deg/hour)
    tide_speed(5)    = 15.041069 !  phase speeds of tidal components (deg/hour)
    tide_speed(6)    = 27.895355 !  phase speeds of tidal components (deg/hour)
    tide_speed(7)    = 27.968210 !  phase speeds of tidal components (deg/hour)
    tide_speed(8)    = 28.439730 !  phase speeds of tidal components (deg/hour)
    tide_speed(9)    = 28.512585 !  phase speeds of tidal components (deg/hour)
    tide_speed(10)    = 28.984106 !  phase speeds of tidal components (deg/hour)
    tide_speed(11)    = 29.528479 !  phase speeds of tidal components (deg/hour)
    tide_speed(12)    = 29.958935 !  phase speeds of tidal components (deg/hour)
    tide_speed(13)    = 30.000002 !  phase speeds of tidal components (deg/hour)
    tide_speed(14)    = 30.082138 !  phase speeds of tidal components (deg/hour)
    tide_speed(15)    = 57.968212 !  phase speeds of tidal components (deg/hour)
    ln_tide_date = .true.               !  adjust tidal harmonics for start date of run
```

```
/
!!======================================================================
!!                  ***  Bottom boundary condition  ***
!!======================================================================
!!   nambfr          bottom friction
!!   nambbc          bottom temperature boundary condition
!!   nambbl          bottom boundary layer scheme                      ("key_trabbl")
!!======================================================================
!
!-----------------------------------------------------------------------
&nambfr         !   bottom friction
!-----------------------------------------------------------------------
   nn_bfr      =    1       !  type of bottom friction :   = 0 : free slip,  = 1 : linear friction
                            !                              = 2 : nonlinear friction
   rn_bfri1    =    4.e-5   !  bottom drag coefficient (linear case)
   rn_bfri2    =    1.e-3   !  bottom drag coefficient (non linear case)
   rn_bfeb2    =    2.5e-3  !  bottom turbulent kinetic energy background  (m^2/s^2)
   ln_bfr2d    = .false.    !  horizontal variation of the bottom friction coef (read a 2D mask file )
   rn_bfrien   =    50.     !  local multiplying factor of bfr (ln_bfr2d = .true.)
   ln_bfrimp   = .true.     !  implicit bottom friction (requires ln_zdfexp = .false. if true)
/
!-----------------------------------------------------------------------
&nambbc         !   bottom temperature boundary condition
!-----------------------------------------------------------------------
   ln_trabbc   = .false.    !  Apply a geothermal heating at the ocean bottom
   nn_geoflx   =    0       !  geothermal heat flux: = 0 no flux
                            !      = 1 constant flux
                            !      = 2 variable flux (read in geothermal_heating.nc in mW/m2)
   rn_geoflx_cst = 86.4e-3  !  Constant value of geothermal heat flux [W/m2]
/
!-----------------------------------------------------------------------
&nambbl         !   bottom boundary layer scheme
!-----------------------------------------------------------------------
   nn_bbl_ldf  =  0      !  diffusive bbl (=1)   or not (=0)
   nn_bbl_adv  =  0      !  advective bbl (=1/2) or not (=0)
   rn_ahtbbl   =  1000.  !  lateral mixing coefficient in the bbl  [m2/s]
   rn_gambbl   =  10.    !  advective bbl coefficient                [s]
/

!!======================================================================
!!                      Tracer (T & S ) namelists
!!======================================================================
!!   nameos          equation of state
!!   namtra_adv      advection scheme
!!   namtra_ldf      lateral diffusion scheme
!!   namtra_dmp      T & S newtonian damping
!!======================================================================
!
!-----------------------------------------------------------------------
&nameos         !   ocean physical parameters
!-----------------------------------------------------------------------
   nn_eos      =    0       !  type of equation of state and Brunt-Vaisala frequency
                            !      = 0, UNESCO (formulation of Jackett and McDougall (1994) and of McDougall (1987) )
                            !      = 1, linear: rho(T)   = rau0 * ( 1.028 - ralpha * T )
                            !      = 2, linear: rho(T,S) = rau0 * ( rbeta * S - ralpha * T )
   rn_alpha    =    2.0e-4  !  thermal expension coefficient (nn_eos= 1 or 2)
   rn_beta     =    7.7e-4  !  saline  expension coefficient (nn_eos= 2)
/
!-----------------------------------------------------------------------
&namtra_adv     !   advection scheme for tracer
!-----------------------------------------------------------------------
   ln_traadv_cen2   =  .false.  !  2nd order centered scheme
   ln_traadv_tvd    =  .true.   !  TVD scheme
   ln_traadv_muscl  =  .false.  !  MUSCL scheme
   ln_traadv_muscl2 =  .false.  !  MUSCL2 scheme + cen2 at boundaries
   ln_traadv_ubs    =  .false.  !  UBS scheme
   ln_traadv_qck    =  .false.  !  QUICKEST scheme
/
!-----------------------------------------------------------------------------------
&namtra_ldf     !   lateral diffusion scheme for tracers
!-----------------------------------------------------------------------------------
   !                        !  Operator type:
   ln_traldf_lap    =  .true.   !  laplacian operator
   ln_traldf_bilap  =  .false.  !  bilaplacian operator
   !                        !  Direction of action:
   ln_traldf_level  =  .false.  !  iso-level
   ln_traldf_hor    =  .true.   !  horizontal (geopotential)   (needs "key_ldfslp" when ln_sco=T)
   ln_traldf_iso    =  .false.  !  iso-neutral                 (needs "key_ldfslp")
   !                        !  Griffies parameters         (all need "key_ldfslp")
   ln_traldf_grif   =  .false.  !  use griffies triads
   ln_traldf_gdia   =  .false.  !  output griffies eddy velocities
   ln_triad_iso     =  .false.  !  pure lateral mixing in ML
   ln_botmix_grif   =  .false.  !  lateral mixing on bottom
   !                        !  Coefficients
   ! Eddy-induced (GM) advection always used with Griffies; otherwise needs "key_traldf_eiv"
   ! Value rn_aeiv_0 is ignored unless = 0 with Held-Larichev spatially varying aeiv
   !                              (key_traldf_c2d & key_traldf_eiv & key_orca_r2, _r1 or _r05)
   rn_aeiv_0        =     0.    !  eddy induced velocity coefficient [m2/s]
   rn_aht_0         =     5.0e3 !  horizontal eddy diffusivity for tracers [m2/s]
   rn_ahtb_0        =     0.    !  background eddy diffusivity for ldf_iso [m2/s]
   !                                 (normally=0; not used with Griffies)
/
!-----------------------------------------------------------------------
&namtra_dmp     !   tracer: T & S newtonian damping
!-----------------------------------------------------------------------
   ln_tradmp   =  .false.   !  add a damping termn (T) or not (F)
   nn_hdmp     =   -1       !  horizontal shape =-1, damping in Med and Red Seas only
                            !                   =XX, damping poleward of XX degrees (XX>0)
                            !                      + F(distance-to-coast) + Red and Med Seas
   nn_zdmp     =    1       !  vertical   shape =0    damping throughout the water column
                            !                   =1 no damping in the mixing layer (kz  criteria)
                            !                   =2 no damping in the mixed  layer (rho crieria)
   rn_surf     =   50.      !  surface time scale of damping   [days]
   rn_bot      =  360.      !  bottom  time scale of damping   [days]
   rn_dep      =  800.      !  depth of transition between rn_surf and rn_bot [meters]
   nn_file     =    1       !  create a damping.coeff NetCDF file (=1) or not (=0)
/

!!======================================================================
!!                      ***  Dynamics namelists  ***
!!======================================================================
!!   namdyn_adv      formulation of the momentum advection
!!   namdyn_vor      advection scheme
!!   namdyn_hpg      hydrostatic pressure gradient
!!   namdyn_spg      surface pressure gradient                      (CPP key only)
!!   namdyn_ldf      lateral diffusion scheme
```

```
!-----------------------------------------------------------------------
!
!-----------------------------------------------------------------------
&namdyn_adv     !   formulation of the momentum advection
!-----------------------------------------------------------------------
   ln_dynadv_vec = .true.  !  vector form (T) or flux form (F)
   ln_dynadv_cen2= .false. !  flux form - 2nd order centered scheme
   ln_dynadv_ubs = .false. !  flux form - 3rd order UBS      scheme
/
!-----------------------------------------------------------------------
&namdyn_vor     !   option of physics/algorithm (not control by CPP keys)
!-----------------------------------------------------------------------
   ln_dynvor_ene = .false. !  energy    conserving scheme
   ln_dynvor_ens = .false. !  enstrophy conserving scheme
   ln_dynvor_mix = .false. !  mixed scheme
   ln_dynvor_een = .true.  !  energy & enstrophy scheme
/
!-----------------------------------------------------------------------
&namdyn_hpg     !   Hydrostatic pressure gradient option
!-----------------------------------------------------------------------
   ln_hpg_zco  = .false.   !  z-coordinate - full steps
   ln_hpg_zps  = .true.    !  z-coordinate - partial steps (interpolation)
   ln_hpg_sco  = .false.   !  s-coordinate (standard jacobian formulation)
   ln_hpg_djc  = .false.   !  s-coordinate (Density Jacobian with Cubic polynomial)
   ln_hpg_prj  = .false.   !  s-coordinate (Pressure Jacobian scheme)
   ln_dynhpg_imp = .false. !  time stepping: semi-implicit time scheme  (T)
                           !                  centered      time scheme  (F)
/
!-----------------------------------------------------------------------
!namdyn_spg     !   surface pressure gradient   (CPP key only)
!-----------------------------------------------------------------------
!                           !  explicit free surface                   ("key_dynspg_exp")
!                           !  filtered free surface                   ("key_dynspg_flt")
!                           !  split-explicit free surface             ("key_dynspg_ts")

!-----------------------------------------------------------------------
&namdyn_ldf     !   lateral diffusion on momentum
!-----------------------------------------------------------------------
   !                        !  Type of the operator :
   ln_dynldf_lap    =  .true.   !  laplacian operator
   ln_dynldf_bilap  =  .false.  !  bilaplacian operator
   !                        !  Direction of action  :
   ln_dynldf_level  =  .false.  !  iso-level
   ln_dynldf_hor    =  .true.   !  horizontal (geopotential)           (require "key_ldfslp" in s-coord.)
   ln_dynldf_iso    =  .false.  !  iso-neutral                         (require "key_ldfslp")
   !                        !  Coefficient
   rn_ahm_0_lap     =     5.0e4 !  horizontal laplacian eddy viscosity   [m2/s]
   rn_ahmb_0        =     0.    !  background eddy viscosity for ldf_iso [m2/s]
   rn_ahm_0_blp     =     0.    !  horizontal bilaplacian eddy viscosity [m4/s]
/

!=======================================================================
!!             Tracers & Dynamics vertical physics namelists
!=======================================================================
!!    namzdf         vertical physics
!!    namzdf_ric     richardson number dependent vertical mixing         ("key_zdfric")
!!    namzdf_tke     TKE dependent vertical mixing                       ("key_zdftke")
!!    namzdf_kpp     KPP dependent vertical mixing                       ("key_zdfkpp")
!!    namzdf_ddm     double diffusive mixing parameterization            ("key_zdfddm")
!!    namzdf_tmx     tidal mixing parameterization                       ("key_zdftmx")
!=======================================================================
!
!-----------------------------------------------------------------------
&namzdf         !   vertical physics
!-----------------------------------------------------------------------
   rn_avm0      =    1.0e-3 !  vertical eddy viscosity   [m2/s]          (background Kz if not "key_zdfcst")
   rn_avt0      =    1.0e-4 !  vertical eddy diffusivity [m2/s]          (background Kz if not "key_zdfcst")
   nn_avb       =    0      !  profile for background avt & avm (=1) or not (=0)
   nn_havtb     =    0      !  horizontal shape for avtb (=1) or not (=0)
   ln_zdfevd    = .true.    !  enhanced vertical diffusion (evd) (T) or not (F)
   nn_evdm      =    1          !  evd apply on tracer (=0) or on tracer and momentum (=1)
   rn_avevd     =  100.         !  evd mixing coefficient [m2/s]
   ln_zdfnpc    = .false.   !  Non-Penetrative Convective algorithm (T) or not (F)
   nn_npc       =    1          !  frequency of application of npc
   nn_npcp      =  365          !  npc control print frequency
   ln_zdfexp    = .false.   !  time-stepping: split-explicit (T) or implicit (F) time stepping
   nn_zdfexp    =    3          !  number of sub-timestep for ln_zdfexp=T
/
!-----------------------------------------------------------------------
&namzdf_ric     !   richardson number dependent vertical diffusion      ("key_zdfric" )
!-----------------------------------------------------------------------
   rn_avmri     = 100.e-4   !  maximum value of the vertical viscosity
   rn_alp       =   5.      !  coefficient of the parameterization
   nn_ric       =   2       !  coefficient of the parameterization
   rn_ekmfc     =   0.7     !  Factor in the Ekman depth Equation
   rn_mldmin    =   1.0     !  minimum allowable mixed-layer depth estimate (m)
   rn_mldmax    =1000.0     !  maximum allowable mixed-layer depth estimate (m)
   rn_wtmix     =  10.0     !  vertical eddy viscosity coeff [m2/s] in the mixed-layer
   rn_wvmix     =  10.0     !  vertical eddy diffusion coeff [m2/s] in the mixed-layer
   ln_mldw      = .true.    !  Flag to use or not the mized layer depth param.
/
!-----------------------------------------------------------------------
&namzdf_tke     !   turbulent eddy kinetic dependent vertical diffusion  ("key_zdftke")
!-----------------------------------------------------------------------
   rn_ediff     =   0.1     !  coef. for vertical eddy coef. (avt=rn_ediff*mxl*sqrt(e) )
   rn_ediss     =   0.7     !  coef. of the Kolmogoroff dissipation
   rn_ebb       =  67.83    !  coef. of the surface input of tke (=67.83 suggested when ln_mxl0=T)
   rn_emin      =   1.e-6   !  minimum value of tke [m2/s2]
   rn_emin0     =   1.e-4   !  surface minimum value of tke [m2/s2]
   nn_mxl       =   2       !  mixing length: = 0 bounded by the distance to surface and bottom
                            !                 = 1 bounded by the local vertical scale factor
                            !                 = 2 first vertical derivative of mixing length bounded by 1
                            !                 = 3 as =2 with distinct disspipative an mixing length scale
   nn_pdl       =   1       !  Prandtl number function of richarson number (=1, avt=pdl(Ri)*avm) or not (=0, avt=avm)
   ln_mxl0      = .true.    !  surface mixing length scale = F(wind stress) (T) or not (F)
   rn_mxl0      =   0.04    !  surface  buoyancy lenght scale minimum value
   ln_lc        = .true.    !  Langmuir cell parameterisation (Axell 2002)
   rn_lc        =   0.15    !  coef. associated to Langmuir cells
   nn_etau      =   0       !  penetration of tke below the mixed layer (ML) due to internal & intertial waves
                            !       = 0 no penetration
                            !       = 1 add a tke source below the ML
                            !       = 2 add a tke source just at the base of the ML
                            !       = 3 as = 1 applied on HF part of the stress    ("key_coupled")
   rn_efr       =   0.05    !  fraction of surface tke value which penetrates below the ML (nn_etau=1 or 2)
   nn_htau      =   1       !  type of exponential decrease of tke penetration below the ML
                            !       = 0  constant 10 m length scale
```

```
                              !        = 1  0.5m at the equator to 30m poleward of 40 degrees
/
!-----------------------------------------------------------------------
&namzdf_kpp     !   K-Profile Parameterization dependent vertical mixing  ("key_zdfkpp", and optionally:
!-----------------------------------------------------------------------  "key_kppcustom" or "key_kpplktb")
   ln_kpprimix = .true.     !  shear instability mixing
   rn_difmiw   =  1.0e-04   !  constant internal wave viscosity [m2/s]
   rn_difsiw   =  0.1e-04   !  constant internal wave diffusivity [m2/s]
   rn_riinfty  =  0.8       !  local Richardson Number limit for shear instability
   rn_difri    =  0.0050    !  maximum shear mixing at Rig = 0    [m2/s]
   rn_bvsqcon  = -0.01e-07  !  Brunt-Vaisala squared for maximum convection [1/s2]
   rn_difcon   =  1.        !  maximum mixing in interior convection [m2/s]
   nn_avb      =  0         !  horizontal averaged (=1) or not (=0) on avt and amv
   nn_ave      =  1         !  constant (=0) or profile (=1) background on avt
/
!-----------------------------------------------------------------------
&namzdf_gls                 !   GLS vertical diffusion                   ("key_zdfgls")
!-----------------------------------------------------------------------
   rn_emin        = 1.e-6   !  minimum value of e   [m2/s2]
   rn_epsmin      = 1.e-12  !  minimum value of eps [m2/s3]
   ln_length_lim = .true.   !  limit on the dissipation rate under stable stratification (Galperin et al., 1988)
   rn_clim_galp  = 0.53     !  galperin limit
   ln_crban      = .true.   !  Use Craig & Banner (1994) surface wave mixing parametrisation
   ln_sigpsi     = .true.   !  Activate or not Burchard 2001 mods on psi schmidt number in the wb case
   rn_crban      = 100.     !  Craig and Banner 1994 constant for wb tke flux
   rn_charn      = 70000.   !  Charnock constant for wb induced roughness length
   nn_tkebc_surf =   1      !  surface tke condition (0/1/2=Dir/Neum/Dir Mellor-Blumberg)
   nn_tkebc_bot  =   1      !  bottom tke condition (0/1=Dir/Neum)
   nn_psibc_surf =   1      !  surface psi condition (0/1/2=Dir/Neum/Dir Mellor-Blumberg)
   nn_psibc_bot  =   1      !  bottom psi condition (0/1=Dir/Neum)
   nn_stab_func  =   2      !  stability function (0=Galp, 1= KC94, 2=CanutoA, 3=CanutoB)
   nn_clos       =   1      !  predefined closure type (0=MY82, 1=k-eps, 2=k-w, 3=Gen)
/
!-----------------------------------------------------------------------
&namzdf_ddm     !   double diffusive mixing parameterization             ("key_zdfddm")
!-----------------------------------------------------------------------
   rn_avts     = 1.e-4      !  maximum avs (vertical mixing on salinity)
   rn_hsbfr    = 1.6        !  heat/salt buoyancy flux ratio
/
!-----------------------------------------------------------------------
&namzdf_tmx     !   tidal mixing parameterization                        ("key_zdftmx")
!-----------------------------------------------------------------------
   rn_htmx     = 500.       !  vertical decay scale for turbulence (meters)
   rn_n2min    = 1.e-8      !  threshold of the Brunt-Vaisala frequency (s-1)
   rn_tfe      = 0.333      !  tidal dissipation efficiency
   rn_me       = 0.2        !  mixing efficiency
   ln_tmx_itf  = .false.    !  ITF specific parameterisation
   rn_tfe_itf  = 1.         !  ITF tidal dissipation efficiency
/

!!======================================================================
!!                  ***  Miscelaneous namelists  ***
!!======================================================================
!!   nammpp            Massively Parallel Processing                    ("key_mpp_mpi)
!!   namctl            Control prints & Benchmark
!!   namsol            elliptic solver / island / free surface
!!======================================================================
!
!-----------------------------------------------------------------------
&namsol         !   elliptic solver / island / free surface
!-----------------------------------------------------------------------
   nn_solv     =       2    !  elliptic solver: =1 preconditioned conjugate gradient (pcg)
                            !                   =2 successive-over-relaxation (sor)
   nn_sol_arp  =       0    !  absolute/relative (0/1) precision convergence test
   rn_eps      =   1.e-6    !  absolute precision of the solver
   nn_nmin     =     210    !  minimum of iterations for the SOR solver
   nn_nmax     =     800    !  maximum of iterations for the SOR solver
   nn_nmod     =      10    !  frequency of test for the SOR solver
   rn_resmax   =  1.e-10    !  absolute precision for the SOR solver
   rn_sor      =  1.96      !  optimal coefficient for SOR solver (to be adjusted with the domain)
/
!-----------------------------------------------------------------------
&nammpp         !   Massively Parallel Processing                        ("key_mpp_mpi)
!-----------------------------------------------------------------------
   cn_mpi_send =  'I'       !  mpi send/recieve type   ='S', 'B', or 'I' for standard send,
                            !  buffer blocking send or immediate non-blocking sends, resp.
   nn_buffer   =    0       !  size in bytes of exported buffer ('B' case), 0 no exportation
   ln_nnogather=  .false.   !  activate code to avoid mpi_allgather use at the northfold
   jpni        =    0       !  jpni   number of processors following i (set automatically if < 1)
   jpnj        =    0       !  jpnj   number of processors following j (set automatically if < 1)
   jpnij       =   20       !  jpnij  number of local domains (set automatically if < 1)
/
!-----------------------------------------------------------------------
&namctl         !   Control prints & Benchmark
!-----------------------------------------------------------------------
   ln_ctl      = .false.    !  trends control print (expensive!)
   nn_print    =    0       !  level of print (0 no extra print)
   nn_ictls    =    0       !  start i indice of control sum (use to compare mono versus
   nn_ictle    =    0       !  end   i indice of control sum         multi processor runs
   nn_jctls    =    0       !  start j indice of control               over a subdomain)
   nn_jctle    =    0       !  end   j indice of control
   nn_isplt    =    1       !  number of processors in i-direction
   nn_jsplt    =    1       !  number of processors in j-direction
   nn_bench    =    0       !  Bench mode (1/0): CAUTION use zero except for bench
                            !     (no physical validity of the results)
   nn_timing   =    1       !  timing by routine activated (=1) creates timing.output file, or not (=0)
/

!!======================================================================
!!                  ***  Diagnostics namelists  ***
!!======================================================================
!!   namnc4          netcdf4 chunking and compression settings          ("key_netcdf4")
!!   namtrd          dynamics and/or tracer trends                      ("key_trddyn","key_trdtra","key_trdmld")
!!   namflo          float parameters                                   ("key_float")
!!   namptr          Poleward Transport Diagnostics
!!   namhsb          Heat and salt budgets
!!======================================================================
!
!-----------------------------------------------------------------------
&namnc4         !   netcdf4 chunking and compression settings          ("key_netcdf4")
!-----------------------------------------------------------------------
   nn_nchunks_i=   4        !  number of chunks in i-dimension
   nn_nchunks_j=   4        !  number of chunks in j-dimension
   nn_nchunks_k=   31       !  number of chunks in k-dimension
                            !  setting nn_nchunks_k = jpk will give a chunk size of 1 in the vertical which
                            !  is optimal for postprocessing which works exclusively with horizontal slabs
```

```
   ln_nc4zip   = .true.    !  (T) use netcdf4 chunking and compression
                           !  (F) ignore chunking information and produce netcdf3-compatible files
/
!-----------------------------------------------------------------------
&namtrd        !   diagnostics on dynamics and/or tracer trends                  ("key_trddyn" and/or "key_trdtra")
!              !       or mixed-layer trends or barotropic vorticity             ("key_trdmld" or     "key_trdvor")
!-----------------------------------------------------------------------
   nn_trd      = 365       !  time step frequency dynamics and tracers trends
   nn_ctls     =   0       !  control surface type in mixed-layer trends (0,1 or n<jpk)
   rn_ucf      =   1.      !  unit conversion factor (=1 -> /seconds ; =86400. -> /day)
   cn_trdrst_in      = "restart_mld"    ! suffix of ocean restart name (input)
   cn_trdrst_out     = "restart_mld"    ! suffix of ocean restart name (output)
   ln_trdmld_restart = .false.          !  restart for ML diagnostics
   ln_trdmld_instant = .false.          !  flag to diagnose trends of instantantaneous or mean ML T/S
/
!-----------------------------------------------------------------------
&namflo        !   float parameters                                              ("key_float")
!-----------------------------------------------------------------------
   jpnfl         = 0           !  total number of floats during the run
   jpnnewflo     = 0           !  number of floats for the restart
   ln_rstflo     = .false.     !  float restart (T) or not (F)
   nn_writefl    =      75     !  frequency of writing in float output file
   nn_stockfl    =    5475     !  frequency of creation of the float restart file
   ln_argo       = .false.     !  Argo type floats (stay at the surface each 10 days)
   ln_flork4     = .false.     !  trajectories computed with a 4th order Runge-Kutta (T)
                               !  or computed with Blanke' scheme (F)
   ln_ariane     = .true.      !  Input with Ariane tool convention(T)
   ln_flo_ascii  = .true.      !  Output with Ariane tool netcdf convention(F) or ascii file (T)
/
!-----------------------------------------------------------------------
&namptr        !   Poleward Transport Diagnostic
!-----------------------------------------------------------------------
   ln_diaptr  = .false.     !  Poleward heat and salt transport (T) or not (F)
   ln_diaznl  = .true.      !  Add zonal means and meridional stream functions
   ln_subbas  = .false.     !  Atlantic/Pacific/Indian basins computation (T) or not
                            !  (orca configuration only, need input basins mask file named "subbasins.nc"
   ln_ptrcomp = .true.      !  Add decomposition : overturning
   nn_fptr    =  1          !  Frequency of ptr computation [time step]
   nn_fwri    =  15         !  Frequency of ptr outputs [time step]
/
!-----------------------------------------------------------------------
&namhsb        !  Heat and salt budgets
!-----------------------------------------------------------------------
   ln_diahsb  = .false.     !  check the heat and salt budgets (T) or not (F)
/
!-----------------------------------------------------------------------
&namdct         ! transports through sections
!-----------------------------------------------------------------------
    nn_dct       = 60        !  time step frequency for transports computing
    nn_dctwri    = 60        !  time step frequency for transports writing
    nn_secdebug = 0          !      0 : no section to debug
                             !     -1 : debug all section
                             !  0 < n : debug section number n
/

!!======================================================================
!!            ***  Observation & Assimilation namelists ***
!!======================================================================
!!    namobs        observation and model comparison                        ('key_diaobs')
!!    nam_asminc    assimilation increments                                 ('key_asminc')
!!======================================================================
!
!-----------------------------------------------------------------------
&namobs        !  observation usage switch                                  ('key_diaobs')
!-----------------------------------------------------------------------
   ln_t3d     = .false.     ! Logical switch for T profile observations
   ln_s3d     = .false.     ! Logical switch for S profile observations
   ln_ena     = .false.     ! Logical switch for ENACT insitu data set
   !                        !     ln_cor                Logical switch for Coriolis insitu data set
   ln_profb   = .false.     ! Logical switch for feedback insitu data set
   ln_sla     = .false.     ! Logical switch for SLA observations

   ln_sladt   = .false.     ! Logical switch for AVISO SLA data

   ln_slafb   = .false.     ! Logical switch for feedback SLA data
                            !     ln_ssh                Logical switch for SSH observations

   ln_sst     = .false.     ! Logical switch for SST observations
                            !     ln_reysst             Logical switch for Reynolds observations
                            !     ln_ghrsst             Logical switch for GHRSST observations

   ln_sstfb   = .false.     ! Logical switch for feedback SST data
                            !     ln_sss                Logical switch for SSS observations
                            !     ln_seaice             Logical switch for Sea Ice observations
                            !     ln_vel3d              Logical switch for velocity observations
                            !     ln_velavcur           Logical switch for velocity daily av. cur.
                            !     ln_velhrcur           Logical switch for velocity high freq. cur.
                            !     ln_velavadcp          Logical switch for velocity daily av. ADCP
                            !     ln_velhradcp          Logical switch for velocity high freq. ADCP
                            !     ln_velfb              Logical switch for feedback velocity data
                            !     ln_grid_global        Global distribtion of observations
                            !     ln_grid_search_lookup Logical switch for obs grid search w/lookup table
                            !     grid_search_file      Grid search lookup file header
                            !     enactfiles            ENACT input observation file names
                            !     coriofiles            Coriolis input observation file name
   !                        ! profbfiles: Profile feedback input observation file name
   profbfiles = 'profiles_01.nc'
                            !     ln_profb_enatim       Enact feedback input time setting switch
                            !     slafilesact           Active SLA input observation file name
                            !     slafilespas           Passive SLA input observation file name
   !                        ! slafbfiles: Feedback SLA input observation file name
   slafbfiles = 'sla_01.nc'
                            !     sstfiles              GHRSST input observation file name
   !                        ! sstfbfiles: Feedback SST input observation file name
   sstfbfiles = 'sst_01.nc' 'sst_02.nc' 'sst_03.nc' 'sst_04.nc' 'sst_05.nc'
                            !     seaicefiles           Sea Ice input observation file name
                            !     velavcurfiles         Vel. cur. daily av. input file name
                            !     velhvcurfiles         Vel. cur. high freq. input file name
                            !     velavadcpfiles        Vel. ADCP daily av. input file name
                            !     velhvadcpfiles        Vel. ADCP high freq. input file name
                            !     velfbfiles            Vel. feedback input observation file name
                            !     dobsini               Initial date in window YYYYMMDD.HHMMSS
                            !     dobsend               Final date in window YYYYMMDD.HHMMSS
                            !     n1dint                Type of vertical interpolation method
                            !     n2dint                Type of horizontal interpolation method
                            !     ln_nea                Rejection of observations near land switch
```

```
   nmsshc      = 0           ! MSSH correction scheme
                             !     mdtcorr                 MDT  correction
                             !     mdtcutoff               MDT cutoff for computed correction
   ln_altbias = .false.      ! Logical switch for alt bias
   ln_ignmis  = .true.       ! Logical switch for ignoring missing files
                             !     endailyavtypes   ENACT daily average types
   ln_grid_global = .true.
   ln_grid_search_lookup = .false.
/
!-----------------------------------------------------------------------
&nam_asminc   !   assimilation increments                                ('key_asminc')
!-----------------------------------------------------------------------
    ln_bkgwri = .false.     !  Logical switch for writing out background state
    ln_trainc = .false.     !  Logical switch for applying tracer increments
    ln_dyninc = .false.     !  Logical switch for applying velocity increments
    ln_sshinc = .false.     !  Logical switch for applying SSH increments
    ln_asmdin = .false.     !  Logical switch for Direct Initialization (DI)
    ln_asmiau = .false.     !  Logical switch for Incremental Analysis Updating (IAU)
    nitbkg    = 0           !  Timestep of background in [0,nitend-nit000-1]
    nitdin    = 0           !  Timestep of background for DI in [0,nitend-nit000-1]
    nitiaustr = 1           !  Timestep of start of IAU interval in [0,nitend-nit000-1]
    nitiaufin = 15          !  Timestep of end of IAU interval in [0,nitend-nit000-1]
    niaufn    = 0           !  Type of IAU weighting function
    ln_salfix = .false.     !  Logical switch for ensuring that the sa > salfixmin
    salfixmin = -9999       !  Minimum salinity after applying the increments
    nn_divdmp = 0           !  Number of iterations of divergence damping operator
/
!-----------------------------------------------------------------------
&namsbc_wave   ! External fields from wave model
!-----------------------------------------------------------------------
!              !  file name  ! frequency (hours) ! variable  ! time interp. !  clim  ! 'yearly'/ ! weights  ! rotation !
!              !             !  (if <0  months)  !   name    !   (logical)  !  (T/F) ! 'monthly' ! filename ! pairing
!
   sn_cdg      =  'cdg_wave' ,        1          , 'drag_coeff' , .true.    , .false. , 'daily'   ,''         , ''
!
   cn_dir_cdg  = './'  !  root directory for the location of drag coefficient files
/
!-----------------------------------------------------------------------
&namdyn_nept   !   Neptune effect (simplified: lateral and vertical diffusions removed)
!-----------------------------------------------------------------------
   ! Suggested lengthscale values are those of Eby & Holloway (1994) for a coarse model
   ln_neptsimp       = .false.  ! yes/no use simplified neptune

   ln_smooth_neptvel = .false.  ! yes/no smooth zunep, zvnep
   rn_tslse          =  1.2e4   ! value of lengthscale L at the equator
   rn_tslsp          =  3.0e3   ! value of lengthscale L at the pole
   ! Specify whether to ramp down the Neptune velocity in shallow
   ! water, and if so the depth range controlling such ramping down
   ln_neptramp       = .false.  ! ramp down Neptune velocity in shallow water
   rn_htrmin         =  100.0   ! min. depth of transition range
   rn_htrmax         =  200.0   ! max. depth of transition range
/
!-----------------------------------------------------------------------
&namtrj ! Handling non-linear trajectory for TAM (output for direct model, input for TAM)
!-----------------------------------------------------------------------
    cn_dirtrj   = 'tam_trajectory'   ! prefix for input/ouput files
    ln_trjhand  = .false.            ! Handling non linear trajectory
    nn_ittrjfrq = 20                 ! Output/input frequency
    ln_trj_spl = .false.             ! Handling trajectory at simple precision
/
```

References

Anderson, D. L. T., Bryan, K., Gill, a. E., & Pacanowski, R. C. (1979). The transient response of the North Atlantic: Some model studies. *Journal of Geophysical Research*, *84*(C8), 4795. doi: 10.1029/JC084iC08p04795

Anderson, D. L. T., & Killworth, P. D. (1977). Spin-up of a stratified ocean, with topography. *Deep-Sea Research*, *24*(8), 709–732. doi: 10.1016/0146-6291(77)90495-7

Bryan, K. (1969). A numerical method for the study of the circulation of the world ocean. *Journal of Computational Physics*, *4*(3), 347–376. doi: 10.1016/0021-9991(69)90004-7

Dee, D. P., Uppala, S. M., Simmons, A. J., Berrisford, P., Poli, P., Kobayashi, S., ... Vitart, F. (2011, apr). The ERA-Interim reanalysis: configuration and performance of the data assimilation system. *Quarterly Journal of the Royal Meteorological Society*, *137*(656), 553–597. doi: 10.1002/qj.828

Döös, K., & Webb, D. (1994). The Deacon cell and the other meridional cells of the Southern Ocean. *Journal of Physical Oceanography*, *24*(2), 429–442. doi: 10.1175/1520-0485(1994)0242.0.CO;2

Drews, A., Greatbatch, R. J., Ding, H., Latif, M., & Park, W. (2015). The use of a flow field correction technique for alleviating the North Atlantic cold bias with application to the Kiel Climate Model. *Ocean Dynamics*, *65*(8), 1079–1093. doi: 10.1007/s10236-015-0853-7

Eden, C., & Olbers, D. (2010). Why western boundary currents are diffusive: A link between bottom pressure torque and bolus velocity. *Ocean Modelling*, *32*(1-2), 14–24. doi: 10.1016/j.ocemod.2009.07.003

Favre, A. (1992). Formulation of the Statistical Equations of Turbulent Flows with Variable Density. In *Studies in turbulence* (pp. pp 324–341).

Gent, P. R., & McWilliams, J. C. (1990). Isopycnal Mixing in Ocean Circulation Models. *Journal of Physical Oceanography*, *20*(1), 150–155. doi: 10.1175/1520-0485(1990)020<0150:IMIOCM>2.0.CO;2

Gill, A. E. (1971). Ocean models. *Philos. Trans. R. Soc. London*, *270*(Ser. A), 391–413.

Greatbatch, R. J., Fanning, A. F., Goulding, A. D., & Levitus, S. (1991). A diagnosis of interpentadal circulation changes in the North Atlantic. *Journal of Geophysical Research*, *96*(C12), 22009. doi: 10.1029/91JC02423

Hasselmann, K. (1982). An ocean model for climate variability studies. *Progress in Oceanography*, *11*(2), 69–92.

Holland, W. R. (1973). Baroclinic and topographic influences on the transport in western boundary currents. *Geophysical Fluid Dynamics*, *4*(1), 187–210. doi: 10.1080/03091927208236095

Hughes, C. W. (2000). A theoretical reason to expect inviscid western boundary currents in realistic oceans. *Ocean Modelling*, *2*(1-2), 73–83. doi: 10.1016/S1463-5003(00)00011-1

Hughes, C. W., & de Cuevas, B. A. (2001). Why Western Boundary Currents in Realistic Oceans are Inviscid: A Link between Form Stress and Bottom Pressure Torques. *Journal of Physical Oceanography*, *31*(10), 2871–2885. doi: 10.1175/1520-0485(2001)031<2871:WWBCIR>2.0.CO;2

Jackson, L., Hughes, C. W., & Williams, R. G. (2006). Topographic control of basin and channel flows: the role of the bottom pressure torques and friction. *Journal of Physical Oceanography*, *36*(October), 1786–1805. doi: 10.1175/JPO2936.1

Knauss, J. (1969). A Note on the Transport of the Gulf Stream. *Deep-Sea Research*, *16*(Supplement), 117–123.

Köhl, A., Käse, R. H., Stammer, D., & Serra, N. (2007). Causes of Changes in the Denmark Strait Overflow. *Journal of Physical Oceanography*, *37*(6), 1678–1696. doi: 10.1175/JPO3080.1

Le Sommer, J., Penduff, T., Theetten, S., Madec, G., & Barnier, B. (2009). How momentum advection schemes influence current-topography interactions at eddy permitting resolution. *Ocean Modelling*, *29*(1), 1–14. doi: 10.1016/j.ocemod.2008.11.007

Locarnini, R. A., Mishonov, A. V., Antonov, J. I., Boyer, T. P., Garcia, H. E., Baranova, O. K., ... Seidov, D. (2013). World Ocean Atlas 2013. Vol. 1: Temperature. *S. Levitus, Ed.; A. Mishonov, Technical Ed.; NOAA Atlas NESDIS*, *73*(September), 40. doi: 10.1182/blood-2011-06-357442

Madec, G. (2008). NEMO ocean engine. *Note du Pôle de modélisation, Institut Pierre-Simon Laplace (IPSL)*(27), 1288–1619.

Mellor, G. L., Mechoso, C. R., & Keto, E. (1982). A diagnostic calculation of the general circulation of the atlantic ocean. *Deep Sea Research Part A. Oceanographic Research Papers*, *29*(10), 1171–1192. doi: 10.1016/0198-0149(82)90088-7

Mertz, G., & Wright, D. G. (1992). Interpretations of the JEBAR Term. *Journal of Physical Oceanography*, *22*(3), 301–305. doi: 10.1175/1520-0485(1992)022<0301:IOTJT>2.0.CO;2

Munk, W. (1950). on the Wind-Driven Ocean Circulation. *Journal of Meteorology*, *7*(2), 80–93. doi: 10.1175/1520-0469(1950)007<0080:OTWDOC>2.0.CO;2

Munk, W., & Palmén, E. (1951). Note on the Dynamics of the Antarctic Circumpolar Current. *Tellus*, 4–6. doi: 10.3402/tellusa.v3i1.8609

Myers, P. G., Fanning, A. F., & Weaver, A. (1996). JEBAR, Bottom Pressure Torque, and Gulf Stream Seperation.

Olbers, D., Willebrand, J., & Eden, C. (2012). *Ocean Dynamics*. doi: 10.1007/978-

3-642-23450-7

Penduff, T., Le Sommer, J., Barnier, B., a. M. Treguier, Molines, J.-M., & Madec, G. (2007). Influence of numerical schemes on current-topography interactions in 1/4° global ocean simulations. *Ocean Science Discussions*, *4*(3), 491–528. doi: 10.5194/osd-4-491-2007

Reynolds, O. (1895). On the Dynamical Theory of Incompressible Viscous Fluids and the Determination of the Criterion. *Philosophical Transactions of the Royal Society of London. A.*, *186*(1895), 123–164.

Rintoul, S., Hughes, C., & Olbers, D. (2001). *The Antarctic Circumpolar Current System*. doi: 10.1002/ajp.20122

Roberts, M. J., & Marshall, D. P. (2000). On the validity of downgradient eddy closures in ocean models. *Journal of Geophysical Research*, *105*(C12), 28613–28627. doi: 10.1029/1999JC000041

Sarkisyan, A. (1969). Deficiencies of Barotropic Models of Oceanic Circulation. *Izv., Atmospheric and Oceanic Physics*, *5*(8), 818–835.

Sarkisyan, A., & Ivanov, V. (1971). Joint Effect of Baroclinicity and Bottom Relief as an Important Factor in the Dynamics of Sea Currents. *Izv., Atmospheric and Oceanic Physics*, *7*(2), 173–188.

Spence, P., Saenko, O. a., Sijp, W., & England, M. (2012). The Role of Bottom Pressure Torques on the Interior Pathways of North Atlantic Deep Water. *Journal of Physical Oceanography*, *42*(1), 110–125. doi: 10.1175/2011JPO4584.1

Stommel, H. (1948). The westward intensification of wind-driven ocean currents. *Trans. Amer. Geophys. Union*, *29*(2), 202–206. doi: 10.1029/TR029i002p00202

Sverdrup, H. U. (1947). Wind-Driven Currents in a Baroclinic Ocean; with Application to the Equatorial Currents of the Eastern Pacific. *Proceedings of the National Academy of Sciences of the United States of America*, *33*(11), 318–326. doi: 10.1073/pnas.33.11.318

Weaver, A. J., & Sarachik, E. S. (1990). On the Importance of Vertical Resolution in Certain Ocean General Circulation Models. *Journal of Physical Oceanography*, *20*(4), 600–609. doi: 10.1175/1520-0485(1990)020<0600:OTIOVR>2.0.CO;2

Willebrand, J., Barnier, B., Böning, C., Dieterich, C., Killworth, P. D., Le Provost, C., ... New, A. L. (2001). Circulation characteristics in three eddy-permitting models of the North Atlantic. *Progress in Oceanography*, *48*(2-3), 123–161. doi: 10.1016/S0079-6611(01)00003-9

Wunsch, C., & Roemmich, D. (1985). Is the North Atlantic in Sverdrup Balance? *Journal of Physical Oceanography*, *15*(12), 1876–1880. doi: 10.1175/1520-0485(1985)015<1876:ITNAIS>2.0.CO;2

Yeager, S. (2015). Topographic coupling of the Atlantic overturning and gyre circulations. *Journal of Physical Oceanography*, 150224120347006. doi:

10.1175/JPO-D-14-0100.1

Zweng, M. M., Reagan, J., Antonov, J., Mishonov, A., Boyer, T., Garcia, H., ... Bidlle, M. (2013). World Ocean Atlas 2013, Volume 2: Salinity. *NOAA Atlas NESDIS*, *119*(1), 227–237. doi: 10.1182/blood-2011-06-357442

ERKLÄRUNG

Hiermit erkläre ich, dass ich die vorliegende Arbeit selbständig und ohne fremde Hilfe angefertigt und keine anderen als die angegebenen Quellen und Hilfsmittel verwendet habe. Die eingereichte schriftliche Fassung der Arbeit entspricht der auf dem elektronischen Speichermedium.

(Name der Datei: Eisbrenner_818852.pdf)

Weiterhin versichere ich, dass diese Arbeit noch nicht als Abschlussarbeit an anderer Stelle vorgelegen hat.

_____

Datum, Unterschrift